THE MEASUREMENT OF THE REAL PART OF THE $P\bar{P}$ ELASTIC SCATTERING AMPLITUDE AT A C.M.S. ENERGY OF 546 GEV AND THE RISE OF THE TOTAL CROSS SECTION

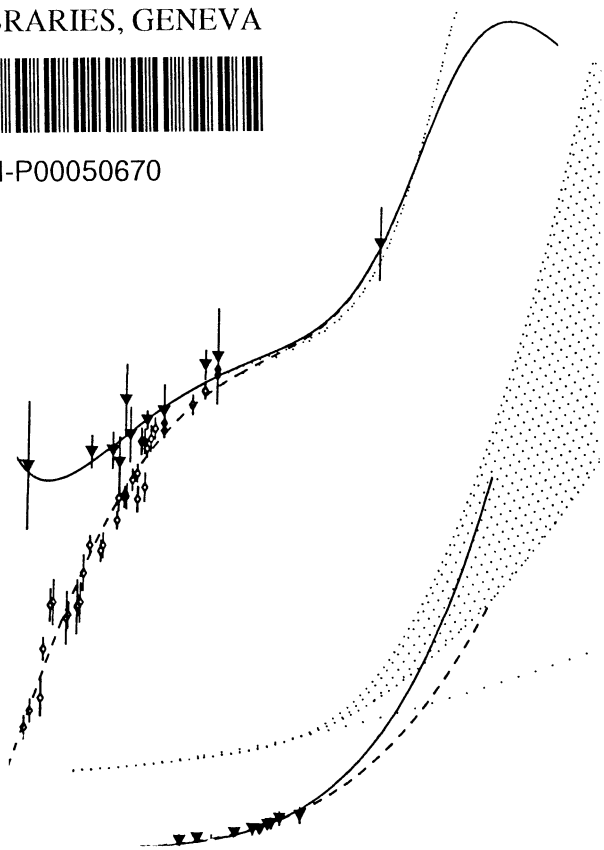

Peter Martin Kluit

THE MEASUREMENT OF THE REAL PART OF THE $P\bar{P}$ ELASTIC SCATTERING AMPLITUDE AT A C.M.S. ENERGY OF 546 GEV AND THE RISE OF THE TOTAL CROSS SECTION

ACADEMISCH PROEFSCHRIFT

TER VERKRIJGING VAN DE GRAAD VAN DOCTOR AAN DE UNIVERSITEIT VAN AMSTERDAM, OP GEZAG VAN DE RECTOR MAGNIFICUS PROF. DR. S. K. THODEN VAN VELZEN IN HET OPENBAAR TE VERDEDIGEN IN DE AULA DER UNIVERSITEIT (OUDE LUTHERSE KERK, SINGEL 411, HOEK SPUI) OP WOENSDAG 7 DECEMBER 1988 TE 15.00 UUR.

door

Peter Martin Kluit

geboren te Hilversum

Promotors : Prof. Dr. A. N. Diddens

Prof. Dr. G. Matthiae

Co-promotor : Dr. J. J. M. Timmermans

The work described in this thesis is part of the research programme of 'het Nationaal Instituut voor Kernfysica en Hoge-Energie Fysica (NIKHEF-H)' in Amsterdam. The author was financially supported by 'de Stichting voor Fundamenteel Onderzoek der Materie (FOM)'.

Integ. Werk, je nie formule?

1) Werk spiroa

2) $F^{NM}(S,t) \sim e^{B \cdot t}$ ↑ celkem int. t.

ale tr nie je celkom tak

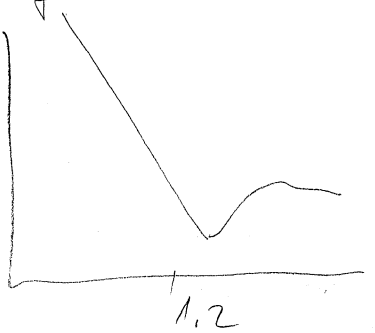

3) Predpoklad, že S je ~~tuntr~~ nezávisle
konštanta $S = S(0)$ ale v skutoč-
nosti je tr $S = S(t)$.

Berglund: zavedol $S = S(t)$ ale
pracoval ϕ (1.14 vzťah)

⇒ formula CAHN (1982)

$F^{1-N}(S,t) = \ldots \int_0^{\infty}$

ale tr diskriminuje, dostali Werk Yamic
formulu.

Do nej pr dá rozdiel amplitúda
F^N - hrad. rozptylu.

Aan mijn ouders

Elektrický formulator

---

v závislosti od periferality, ale predpokladajú
(kruhový + dokonalý), dostávajú

$S(0.19 - 0.23)$

Contents

Chapter 1

Introduction

1.1 Motivation

High Energy Physics studies the fundamental particles and forces of nature in the realm of the subatomic. It searches for the ultimate constituents of matter: the indivisible, elementary particles of which the physical world is built. It investigates the nature of the forces and fields which manifest itself in the interaction with matter. High energy physics tries to discover and formulate the laws which are the foundation of nature. It is expected that behind the variety of physical laws there must be one first unifying principle - one formula - on which everything is based. From this principle all laws of nature can be derived. The tendency to bring the laws back to one first principle is called unification. Although unification is not an established fact - one of the problems with unification is the incorporation of the gravitational force - there are indications that there is a way which could lead to a unified theory.

Recently a great step forward has been set by the discovery of the predicted $W^{\pm}$ and Z bosons in the UA1 and UA2 experiments. This means that the fundamental ideas of the Glashow-Weinberg-Salam model, which unifies the weak and the electromagnetic interaction, are correct. The way towards a final unification of all the four forces (the strong, the weak and electro-magnetic interaction and gravitation) might still be long. Theory indicates that at some energy-scale also the standard model, which unifies the strong , weak and electromagnetic interactions (but not gravitation), should break down and a lot of unknown things can happen. Both theoretically and experimentally a lot of research and tests have to be done to achieve unification, the ultimate goal of physics.

The subject of this thesis is the experimental study of the elastic scattering of protons and anti-protons at a centre of mass energy of 546 GeV at the SPS (Super Proton Synchrotron) at CERN (Conseil Européen pour les Recherches Nucléaires). At this very high energy (1 GeV = 10^9 electron Volts) it is interesting to study the strong interaction. In principle there exists a good theory for

the strong interaction: QCD (Quantum Chromo Dynamics). The problem with QCD is that at this moment only in perturbation theory reliable results can be obtained. Perturbation theory however breaks down at low momentum transfers or Q^2 values. This is the regime where particles scatter elastically: the field of the soft hadronic interactions. Therefore more or less phenomenological models, which are constrained by asymptotic theorems, are developed to understand the nature of the strong interaction.

The elastic scattering of particles due to the strong interaction is described by the nuclear scattering amplitude. This amplitude is a complex analytical function of the energy and the momentum tranfer squared. It contains two basic physical quantities: (i) the total cross section that is related to the imaginary part at zero momentum transfer squared and (ii) ρ, the ratio of the real to the imaginary part of the nuclear scattering amplitude at zero momentum transfer squared. Zero momentum transfer squared corresponds to a scattering angle which equals zero.

The total cross section is equivalent to the interacting surface of the two particles (e.g proton-proton or proton-antiproton). In the seventies the physics community was surprised by the measurement at the ISR (Intersecting Storage Rings) at CERN of a total cross section for proton-proton scattering that rises appreciably as a function of the energy. Before this discovery it was generally accepted that the total cross section for proton-proton and proton-antiproton would decrease and tend towards the same constant. At the ISR the cross section was observed to rise[1] like $\ln^2(s/s_0)$ (s is the centre of mass energy squared, s_0 is a constant) as was anticipated by some theoreticians. Later, other measurements - also for proton-antiproton - confirmed this logarithmic-squared rise with the energy.

The second fundamental quantity ρ is related to the high energy behaviour of the total cross section by the dispersion relations. This means that if ρ is known, predictions for the behaviour of the total cross section at higher energies can be given. This was done at the ISR. By assuming a logarithmic squared rise of the total cross section and the measured ρ values at the ISR a prediction could be given for the total cross section at the SPS Collider: it yielded approximately 60 mb (1 mb is 10^{-31} m^2). This prediction was confirmed in 1983 and 1984 by the measurement of the total cross section for proton-antiproton scattering at the SPS Collider by the UA1 and UA4 collaboration. The most precise and direct confirmation was obtained by the UA4 experiment. The next step was to measure ρ at the SPS and see whether the cross section still rises like $\ln^2(s)$ in the TeV energy domain. This experiment was proposed and carried out by the UA4 Collaboration.[2]

[1] In fact at Serpukov, the total cross section for K^+p was observed to rise somewhat, before the measurements at the ISR. But not much value was attached to this measurement at that time.

[2] The UA4 Collaboration consists of: D. Bernard [2,7], M. Bozzo [3], P.L. Braccini [6], F. Carbonara [4], R. Castaldi [6], F. Cervelli [6], G. Chiefari [4], E. Drago [4], M. Haguenauer [5], V. Innocente [5,11], P.M. Kluit [1], S. Lanzano [4], G. Matthiae [4,8], L. Merola [4], M. Napolitano [4], V. Palladino [4], G. Sanguinetti [6], P. Scampoli [6], S. Scapellato [6,9], G. Sciacca [4], G. Sette [3], J. Timmermans [1], C. Vannini [6], J. Velasco [2,10], P.G. Verdini [6] and F. Visco [4].
[1]) 'NIKHEF-H, Amsterdam, The Netherlands', [2]) 'CERN, European Organization for Nuclear

In this thesis the following subjects will be presented:
(1) The measurement of ρ, i.e. the ratio of the real to the imaginary part of the nuclear part of elastic scattering amplitude for proton-antiproton at zero momentum transfer squared ($-t = 0$ GeV^2), at a centre of mass energy of $\sqrt{s} = 546$ GeV is described.[3]
(2) The implications of the result of this measurement for the behaviour of the total cross section in the TeV domain are derived.[4]
(3) The hypothesis is investigated whether there is a relation between the rise of the total cross section and the rise of the total jet cross section, as calculated in perturbative QCD and observed by the UA1 experiment.[5]

1.2 Elastic scattering

Elastic scattering of protons and antiprotons is described by the reaction:

$$\mathrm{p} + \overline{\mathrm{p}} \rightarrow \mathrm{p} + \overline{\mathrm{p}}$$

For every physical process energy and momentum should be conserved. Energy and momentum are usually combined in the energy-momentum four-vector $\vec{P}$. With $\vec{P} = (\vec{\mathbf{p}}, E_{\mathrm{cms}})$, where $\vec{\mathbf{p}}$ is the momentum and E is the energy. For energy and momentum the relativistic equation of Einstein holds:

$$\vec{P}^2_{\mathrm{cms}} \equiv \vec{\mathbf{p}}^2 - E^2 = -m^2 \tag{1.1}$$

where the velocity of light c is put to 1 and m is the Lorentz-invariant rest-mass of the particle, i.e. the mass of the proton or anti-proton. The four-momentum squared is a Lorentz-invariant quantity. Energy and momentum conservation implies that the sum of in- and outgoing four-momenta $\vec{P}$ are equal:

$$\sum \vec{P}_i^{\mathrm{in}} = \sum \vec{P}_i^{\mathrm{out}} \tag{1.2}$$

Research, Geneva Switzerland', [3]) 'Department of Physics and Sezione INFN, Genoa, Italy', [4]) 'Department of Physics and Sezione INFN, Naples, Italy', [5]) 'École Polytechnique, Palaiseau, France', [6]) 'Department of Physics and Sezione INFN, Pisa, Italy', [7]) now at 'École Polytechnique, Palaiseau, France', [8]) now at 'University of Rome II, Rome, Italy', [9]) now at 'Scuola Normale Superiore, Pisa, Italy', [10]) now at 'IFIC, University of Valencia, Spain' and [11]) now at 'Department of Physics and Sezione INFN, Naples, Italy'.

[3]The result was published in Physics Letters B [1] and presented at CERN in June 1987 by D. Bernard, at the International Europhysics Conference on High Energy Physics in Uppsala in June 1987 by P. M. Kluit and at the International Conference on Elastic and Diffractive Scattering in New York in October 1987 by G. Matthiae.

[4]The result was published in Physics Letters B [2] and presented at the International Conference on Elastic and Diffractive Scattering in New York in October 1987 by P. M. Kluit.

[5]A publication is in preparation.

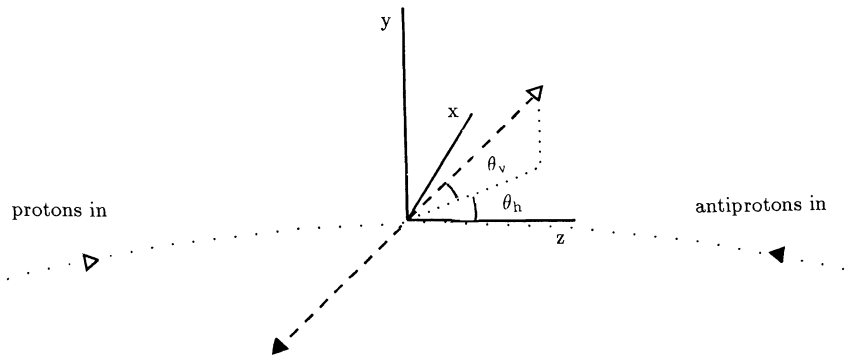

Figure 1.1: Scheme for elastic scattering.

If the proton and the antiproton have the same momenta and collide head-on as in the SPS collider, this formula implies that the outgoing proton and antiproton should be collinear:

$$\theta^{\mathrm{P}}_{\mathrm{h,v}} - \theta^{\overline{\mathrm{P}}}_{\mathrm{h,v}} = 0 \tag{1.3}$$

where $\theta_{\mathrm{h,v}}$ is the angle in the horizontal or vertical direction with respect to the unscattered outgoing proton or antiproton in the centre of mass system (see figure 1.1).

To describe the scattering process the following Lorentz-invariant (Mandelstamm) variables are defined:

$$\begin{aligned} s &= (\vec{P}^{\mathrm{in}}_{\mathrm{p}} + \vec{P}^{\mathrm{in}}_{\overline{\mathrm{p}}})^2 &&= 4E^2_{\mathrm{cms}} \\ t &= (\vec{P}^{\mathrm{in}}_{\mathrm{p}} - \vec{P}^{\mathrm{out}}_{\mathrm{p}})^2 &&= -2p^2_{\mathrm{cms}}(1 - \cos\theta_{\mathrm{h}} \cos\theta_{\mathrm{v}}) \simeq -p^2_{\mathrm{cms}}(\theta^2_{\mathrm{h}} + \theta^2_{\mathrm{v}}) \\ u &= (\vec{P}^{\mathrm{in}}_{\mathrm{p}} - \vec{P}^{\mathrm{out}}_{\overline{\mathrm{p}}})^2 &&= 4m^2 - t - s \end{aligned} \tag{1.4}$$

where cms refers to the centre of mass system and $p^2_{\mathrm{cms}} \equiv \vec{\mathbf{p}}^2_{\mathrm{cms}}$. This means that $\sqrt{s}$ is two times the energy in the centre of mass system, and t the four-momentum transfer squared. At the Collider the proton and antiproton beam have each a momentum of $p_{\mathrm{cms}} = 273$ GeV/c. This corresponds to a value of $\sqrt{s} = 546$ GeV (also 630 GeV, and - in pulsed mode - 900 GeV was reached). Usually the energy E_{lab} in the laboratory system - i.e. the coordinate-system in which one of the two particles is at rest - and the corresponding momentum $\vec{\mathbf{p}}_{\mathrm{lab}}$ are used. They are defined as:

$$\begin{aligned} E_{\mathrm{lab}} &= \frac{s}{2m} - m \\ \vec{\mathbf{p}}^2_{\mathrm{lab}} &= E^2_{\mathrm{lab}} - m^2 \end{aligned} \tag{1.5}$$

Further in the text E and $\vec{p}$ will be used for E_{lab} and $\vec{\mathbf{p}}_{\mathrm{lab}}$.

Elastic scattering is completely determined by the elastic scattering amplitude $F(s,t)$, which is a function of the Lorentz-invariant variables s and t. The elastic scattering amplitude $F(s,t)$ is defined in the laboratory system and is an analytic function of s and t. The differential cross section is related to this amplitude by:

$$\frac{d\sigma}{d\Omega} = |F(s,t)|^2 \tag{1.6}$$

which is equivalent to (putting $\hbar$ and c not equal to 1):

$$\frac{d\sigma}{dt} = \frac{\pi|F(s,t)|^2}{(\hbar c)^2 p^2} \tag{1.7}$$

The scattering amplitude for proton-proton or proton-antiproton consists of two parts: the electromagnetic or Coulomb amplitude (F_c) and the nuclear or hadronic amplitude (F_n).

The imaginary part of the nuclear amplitude at $-t = 0$ is related to the total cross section by the optical theorem:

$$\sigma_{\text{tot}} = 4\pi \frac{\text{Im}(F_n(s,t))}{p}\bigg|_{-t=0} \tag{1.8}$$

The ratio ρ, which is related to the real part of the nuclear amplitude at $-t = 0$, is defined as:

$$\rho = \frac{\text{Re}(F_n(s,t))}{\text{Im}(F_n(s,t))}\bigg|_{-t=0} \tag{1.9}$$

At low four-momentum transfer squared the hadronic amplitude is usually parametrised as a simple exponential with a constant forward elastic slope b (which is a function of s):

$$F_n = \frac{p\,\sigma_{\text{tot}}(\rho + i)\, e^{\frac{-b|t|}{2}}}{4\pi} \tag{1.10}$$

It is assumed that: (1) spin effects can be neglected, (2) the real part has the same t-dependence as the imaginary part in the very forward direction and (3) the low t-region can be described by a constant slope parameter b. These assumptions are valid at the ISR [3], [4]. It will be investigated whether they are still valid at SPS energy. The elastic cross section can be calculated by integrating the differential cross section over $|t|$. This yields:

$$\sigma_{\text{el}} = \frac{(1+\rho^2)\,\sigma_{\text{tot}}^2}{16\pi(\hbar c)^2\, b} \tag{1.11}$$

The Coulomb amplitude F_c for pp (upper case) and $\text{p}\overline{\text{p}}$ (lower case) - which can be derived from the Rutherford scattering formula for the differential cross section - is equal to:

$$F_c = \mp \frac{2\alpha\, p\, G^2(t) e^{\pm i\alpha\phi(t)}}{4\pi|t|} \tag{1.12}$$

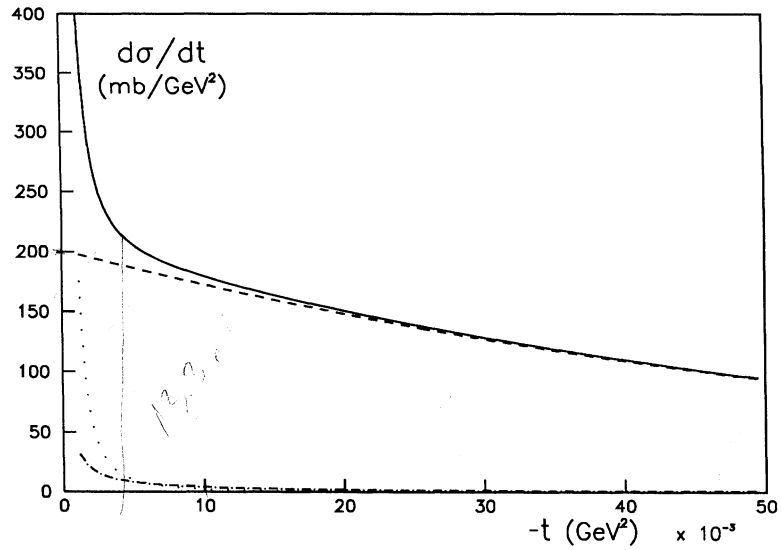

Figure 1.2: The differential cross section for proton-antiproton elastic scattering as a function of $-t$ for $\sqrt{s} = 546$ GeV. We took $\sigma_{p\bar{p}} = 61$ mb, $\rho_{p\bar{p}} = 0.12$, and $b = 15.3$ GeV^{-2} and plotted the different terms of formula (1.15). The solid line represents the sum of the different terms, the dotted line the pure Coulomb term, the dotted-dashed the interference term and the dashed line the pure nuclear term.

where α is the fine-structure constant. $G(t)$ is the proton electromagnetic form factor, which can be written as:

$$G(t) = \frac{\lambda^2}{(\lambda + |t|)^2} \tag{1.13}$$

with $\lambda = 0.71$ GeV^2. The phase $\phi(t)$ - which was calculated first by Bethe [5], and later by West and Yennie [6] and more recently by Cahn [7] - is equal to:

$$\phi(t) = \ln(0.08/|t|) - 0.577 \tag{1.14}$$

If these formulae are substituted in equation (1.7) the differential cross section for proton-antiproton scattering can be calculated:

$$\frac{d\sigma}{dt} = \frac{4\pi(\hbar c)^2\alpha^2 G^4(t)}{|t|^2} + \frac{\sigma_{tot}\alpha(\rho - \alpha\phi(t))G^2(t)e^{\frac{-b|t|}{2}}}{|t|} + \frac{(1+\rho^2)\sigma_{tot}^2 e^{-b|t|}}{16\pi(\hbar c)^2} \tag{1.15}$$

where the first term corresponds to the pure Coulomb, the second term to the interference, and the third to the pure nuclear part of the differential cross section.

At this stage it is possible to sketch the method to determine ρ. If the differential cross section is measured in a certain $|t|$-interval, the different contributions

can be disentangled (see figure 1.2). For very low $|t|$-values ($|t| < 0.001$ GeV^2) the pure Coulomb term is dominant. This term fixes the normalisation. The pure nuclear term is dominant at high $|t|$-values ($|t| > 0.01$ GeV^2). In that region the slope can be determined and - as the overall normalisation is known - the constant $\sigma_{tot}^2(1+\rho^2)$.[6] The interference term is active in the intermediate region. The point of maximum interference (where the ratio of the interference term to the total differential cross section is maximal) lies around $|t| = 0.002$ GeV^2. Because the other terms are fixed, ρ can be determined from this region.

The objective of the measurement can be stated in the following way. The differential cross section should be measured in a $|t|$ region from e.g. 0.001 GeV^2 up to a value of e.g. 0.1 GeV^2. From a fit of formula (1.15) to the data ρ can be determined.

1.3 Asymptotic theorems

The elastic scattering amplitude $F(s,t)$ has an important symmetry, called crossing symmetry. If the elastic scattering amplitude for proton-proton is denoted by $F(s,t)$, the amplitude for proton-antiproton can be obtained by interchanging s and t, i.e. it is given by $F(t,s)$. The physical domain for pp scattering is $s \geq 4m^2$ and $4m^2 - s \leq t \leq 0$. The corresponding domain for the $\mathrm{p\bar{p}}$ case becomes $t \geq 4m^2$ and $4m^2 - t \leq s \leq 0$. In general the elastic scattering amplitude can be split up in two contributions: a part which is even under crossing $F_+(s,t)$ and a part which is odd under crossing $F_-(s,t)$ i.e.:

$$\begin{aligned} F_+(s,t) &= F_+(t,s) \\ F_-(s,t) &= -F_-(t,s) \end{aligned} \tag{1.16}$$

The elastic scattering amplitude for proton-proton $F_{\mathrm{pp}}(s,t)$ and for proton-antiproton $F_{\mathrm{p\bar{p}}}(s,t)$ is given by:

$$\begin{aligned} F_{\mathrm{pp}}(s,t) &= F_+(s,t) + F_-(s,t) \\ F_{\mathrm{p\bar{p}}}(s,t) &= F_+(s,t) - F_-(s,t) \end{aligned} \tag{1.17}$$

Before the discovery of the rising total cross section at the ISR the high energy behaviour of the total cross section could be described by Regge theory (see e.g. [10]). Regge theory assumes that particles are exchanged during the interaction. The scattering amplitude takes the following form:

$$\begin{aligned} F_+(E, -t = 0) &= \sum_k C_k\, p\, (\mathrm{cotan}(\frac{\pi}{2}\alpha_k) - i) E^{\alpha_k - 1} \\ F_-(E, -t = 0) &= \sum_k C_k\, p\, (\tan(\frac{\pi}{2}\alpha_k) + i) E^{\alpha_k - 1} \end{aligned} \tag{1.18}$$

[6] The slope b will be compared with the value which was previously measured by UA4 [8], [9]. In the actual fitting procedure the term $\sigma_{\mathrm{tot}}(1+\rho^2)$ is fixed at the value which was measured by UA4 [8], [9].

where α_k is a constant which corresponds to the pole k. The sum loops over the different poles or Regge trajectories. To describe the non-rising term of the total cross section above $\sqrt{s} \sim 5$ GeV it is sufficient to take two poles in F_+ and one in F_-. This gives the standard Regge parametrisation of the total cross section as a function of the laboratory energy E:

$$\sigma_{\substack{\mathrm{pp} \\ \mathrm{p\overline{p}}}}^{\mathrm{Regge}} = C_1 + C_2 E^{-\alpha_1} \pm C_3 E^{-\alpha_2} \tag{1.19}$$

Before the rise of the total cross section is discussed and parametrised, some important asymptotic theorems are summarised. The Pomeranchuk-theorem [11] states that, if the total cross section goes to a constant, the cross section for pp and $\mathrm{p\overline{p}}$ tend to the same value for infinite energies.

$$\lim_{E \to \infty} (\sigma_{\mathrm{pp}}(E) - \sigma_{\mathrm{p\overline{p}}}(E)) = 0 \tag{1.20}$$

Another restrictive bound was derived from axiomatic field theory by Froissart [12] and Martin [13]. It is based on the unitarity of the scattering amplitude and states an upper limit for the total cross section.

$$\lim_{E \to \infty} \sigma_{\mathrm{tot}}(E) < \frac{\pi(\hbar c)^2}{m_\pi^2 c^4} \ln^2(s/s_0) \tag{1.21}$$

where m_π is the mass of the pion and s_0 is a constant. This upper limit excludes cross sections which rises asymptotically with some power of the energy, as e.g. a Regge pole with a value of α which is greater than one.

A second bound concerning the behaviour of the total cross sections for pp and $\mathrm{p\overline{p}}$ - which also holds in the case the total cross section rises infinitely like $\ln^2(s)$ - is derived by several authors e.g. [14]:

$$\lim_{E \to \infty} \frac{\sigma_{\mathrm{pp}}(E)}{\sigma_{\mathrm{p\overline{p}}}(E)} = 1 \tag{1.22}$$

A similar limit for the ratio of the forward elastic slope b for pp and $\mathrm{p\overline{p}}$ was derived by Cornille and Martin [15]:

$$\lim_{E \to \infty} \frac{b_{\mathrm{pp}}(E)}{b_{\mathrm{p\overline{p}}}(E)} = 1 \tag{1.23}$$

Several scenarios, which stay within these asymptotic bounds, are in principle allowed. (i) If it is assumed that asymptotically the total cross section goes to a constant, it follows from the Pomeranchuk theorem that the difference between the total cross section for pp and for $\mathrm{p\overline{p}}$ should go to zero. (ii) If it is assumed that asymptotically the total cross section rises like $\ln^2(s)$, two possibilities are left open. In the first case - the so-called even interpretation [16] - it is assumed that the elastic scattering amplitude is asymptotically even. This implies that the difference between the total cross section for pp and for $\mathrm{p\overline{p}}$ should go to zero:

$$\lim_{E \to \infty} (\sigma_{\mathrm{pp}}(E) - \sigma_{\mathrm{p\overline{p}}}(E)) = 0 \tag{1.24}$$

The alternative interpretation assumes that the forward elastic scattering amplitude is asymptotically odd. This means that the difference of the total cross section for pp and $p\overline{p}$ can go to a constant value or even rise like $\ln(s)$. This interpretation is called the odderon interpretation [22]. This interpretation is allowed, because the ratio of the total cross sections for pp and $p\overline{p}$ still goes to one for infinite energy, as is required by theorem (1.22).

The measurements at the ISR indicated that the total cross section started to rise approximately like $\ln^2(s/s_0)$. This corresponds asymptotically to the following parametrisation of the elastic scattering amplitude [23]:

$$F_+(s, -t = 0) = i\, p\, (\overline{C}_0(\ln(s/s_0 - i\frac{\pi}{2})^\gamma + C_0) \tag{1.25}$$

where $\overline{C}_0$, C_0 are constants, with $\gamma \leq 2$. An odderon - i.e. in the alternative interpretation - corresponds to the following extra term in the amplitude:

$$F_-(s, -t = 0) = p\, (\overline{B}_0(\ln(s/s_{\text{odd}} - i\frac{\pi}{2})^\beta + B_0) \tag{1.26}$$

where $\overline{B}_0$, B_0 are constants, with $\beta \leq 2$. If β is equal to 2, the maximal odderon is obtained. This corresponds to a term $\ln(s/s_{\text{odd}})$ in the difference of the pp and $p\overline{p}$ total cross section.

A fit to the existing data for the total cross section for pp and $p\overline{p}$ shows that the introduction of an odderon is possible but not necessary. The difference between the pp and the $p\overline{p}$ cross sections tends to zero and can be described by one Regge term without adding an odderon. Therefore the following - the so-called Amaldi - parametrisation [24] for the total cross section was introduced to describe the data in the ISR region:

$$\sigma_{\substack{pp \\ p\overline{p}}} = \sigma^{\text{Regge}}_{\substack{pp \\ p\overline{p}}} + C_4\, \ln^\gamma(s/s_0) \tag{1.27}$$

where $\sigma^{\text{Regge}}_{\substack{pp \\ p\overline{p}}}$ is defined in (1.19). A recent fit to the data (see figure 1.3) shows that this parametrisation describes very well the data for the total cross section up to $\sqrt{s} = 546$ GeV. The constant γ turns out to be 2.00 $\pm$0.01, with C_4 equal to 0.19 $\pm$ 0.01 mb and s_0 fixed at 1 GeV^2. This means that the Froissart bound is qualitatively saturated. The constant in front of the $\ln^2(s/s_0)$ (1.21) is much smaller than the 60 mb, which corresponds to the absolute maximum that is allowed.

1.4 Dispersion relations

Dispersion relations - which relate the real and imaginary part of the elastic scattering amplitude - are essentially based on one axiom: the analyticity of the elastic scattering amplitude. Usually these relations are derived in the laboratory

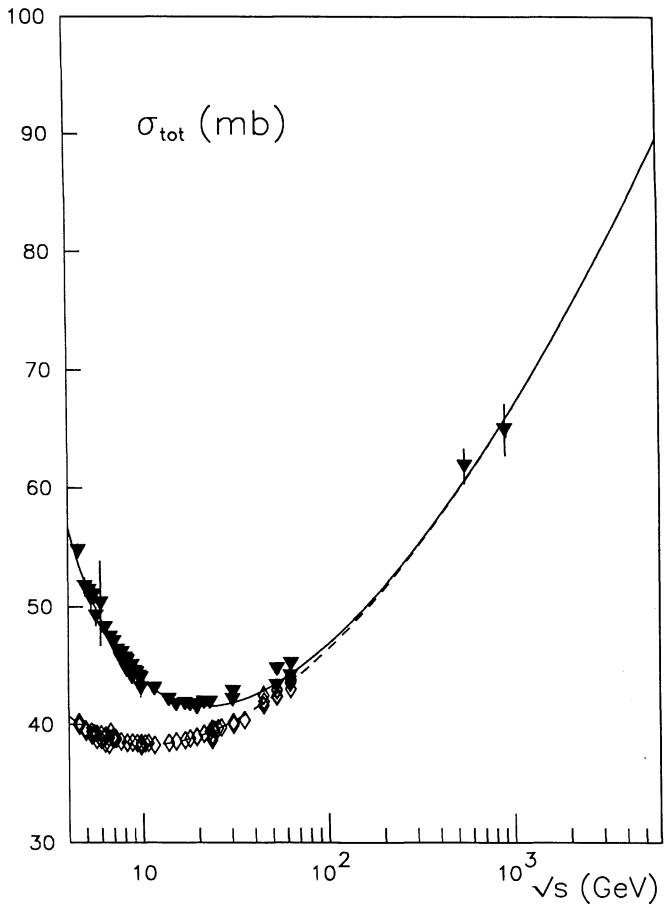

Figure 1.3: The total cross section for pp and $p\overline{p}$. The data are from reference [104]. The black triangles represent the $p\overline{p}$ data points, the open diamonds the pp data points. The dashed line corresponds to the pp total cross section, the solid line corresponds to the $p\overline{p}$ total cross section. They were obtained by a dispersion relation fit through the data points using formula (1.27) and (1.33).

system where a simple crossing relation between the pp and the $p\overline{p}$ amplitudes at $-t = 0$ holds:

$$F_{pp}(-E,t)|_{-t=0} = F_{p\overline{p}}(E,t)|_{-t=0} \tag{1.28}$$

The global idea of a dispersion relation is the following. For an analytic function the real and imaginary part of this function are closely related. Mathematically this is expressed by the Cauchy-Riemann relations, or the Cauchy integral formula

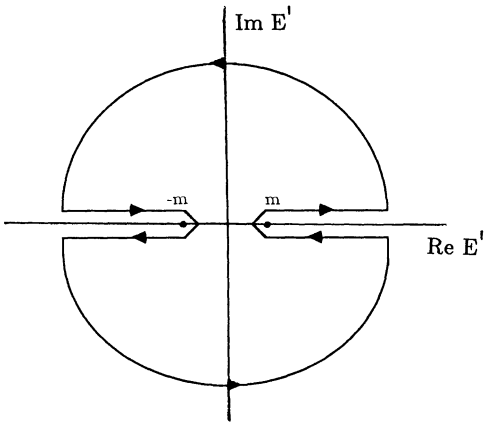

Figure 1.4: Contour in the complex analytic plane.

for a complex analytic function G:

$$G(E,t) = \frac{1}{2\pi i} \oint_C \frac{G(E',t)}{E'-E} dE' \tag{1.29}$$

where C is a closed contour in the complex E' plane around the pole at E that lies on the real axis. If the real part of the left side is taken, a relation is obtained which contains the imaginary part under the integral at the right side. This relation is called a dispersion relation.

To derive mathematically correct a dispersion relation one has to chose a contour in the complex plane, which includes the physical domain on the real axis where the pole at E is located. This contour is shown in figure 1.4. The allowed physical domain is $E > m$ and $E < -m$. If the condition is imposed that the integral over the (infinite) circle vanishes, there remains only an integral (from which the principal value should be taken) over the real axis. Thus it is required that:

$$\lim_{E\to\infty} |G(E,t)| = 0 \tag{1.30}$$

It is known that F doesn't have to satisfy this condition (1.30). The elastic scattering amplitude can rise at most as $\sqrt{E^2 - m^2c^4}\ \ln^2(s)$, thus saturating the Froissart-Martin bound (1.21). In that case the following condition is needed:

$$\lim_{E\to\infty} \frac{|F(E,t)|}{E^2}\bigg|_{-t=0} = 0 \tag{1.31}$$

Applying the Cauchy theorem to $\frac{F(E,t)}{E^2}\big|_{-t=0}$, and defining an analytic continuation of $F(E,t)$ in the complex E-plane, one obtains [25] the twice subtracted dispersion

relation:

$$\rho_{\substack{pp\\p\bar{p}}}(E)\sigma_{\substack{pp\\p\bar{p}}}(E) = \frac{A_0}{\sqrt{E^2-m^2c^4}} \pm \frac{A_1 E}{\sqrt{E^2-m^2c^4}} + \\ + \frac{E^2}{\pi\sqrt{E^2-m^2c^4}} \int_m^\infty dE' \sqrt{E'^2-m^2c^4} \left[\frac{\sigma_{\substack{pp\\p\bar{p}}}(E')}{E'^2(E'-E)} + \frac{\sigma_{\substack{p\bar{p}\\pp}}(E')}{E'^2(E'+E)} \right] \quad (1.32)$$

where A_0 and A_1 are integration constants. The low-energy contributions of the poles, which lie on the real axis (i.e. the low-energy resonances) and the possible spin dependence of the scattering amplitude are neglected.

If the extra assumption is made that the odd terms vanish at infinite energy - i.e. the elastic scattering amplitude is asymptotically an even function of the energy - formula (1.32) can be simplified. This condition implies that the cross section for pp and $p\bar{p}$ will be asymptotically the same (formula (1.24)). In this way one obtains [26] the standard (once subtracted) dispersion relation:

$$\rho_{\substack{pp\\p\bar{p}}}(E)\sigma_{\substack{pp\\p\bar{p}}}(E) = \frac{A_0}{\sqrt{E^2-m^2c^4}} + \\ + \frac{E}{\pi\sqrt{E^2-m^2c^4}} \int_m^\infty dE' \sqrt{E'^2-m^2c^4} \left[\frac{\sigma_{\substack{pp\\p\bar{p}}}(E')}{E'(E'-E)} - \frac{\sigma_{\substack{p\bar{p}\\pp}}(E')}{E'(E'+E)} \right] \quad (1.33)$$

Dispersion relations provide a powerful tool to predict from the real part (or ρ) the high energy behaviour of the total cross section [27]. This type of analysis can be done model-independent, if we allow for all kinds of parametrisations of the total cross section. In chapter 4 this method will be used to derive the consequences of the measured $\rho_{p\bar{p}}$ value. This method was also used at the ISR a decade ago. From measurements of σ_{tot} and ρ up to ISR energies - predictions for σ_{tot} up to Collider energies were obtained [28], [29]. It was a remarkable success: using eq. (1.33) and the Amaldi-parametrisation of the total cross section (1.27) a value of $\sigma_{p\bar{p}}$ between 56 and 66 mb was predicted at $\sqrt{s} = 546$ GeV, while a value of 60 ± 2 mb was measured [1], [8], [9]. A similar analysis was performed more recently on the (pp and $p\bar{p}$) ISR data [3], [4].

Using the standard parametrisation (1.27) a dispersion relation fit predicts for $\rho_{p\bar{p}}$ at the Collider at $\sqrt{s} = 546$ GeV a value of 0.12-0.14 (see figure 1.5). Similar values are predicted by most of the models [30]. This prediction for $\rho_{p\bar{p}}$ can be tested and verified by the experiment of the UA4 collaboration, which is described and discussed in this thesis.

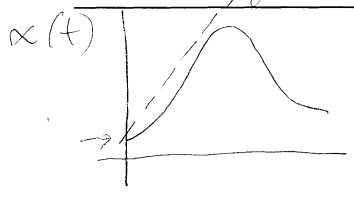

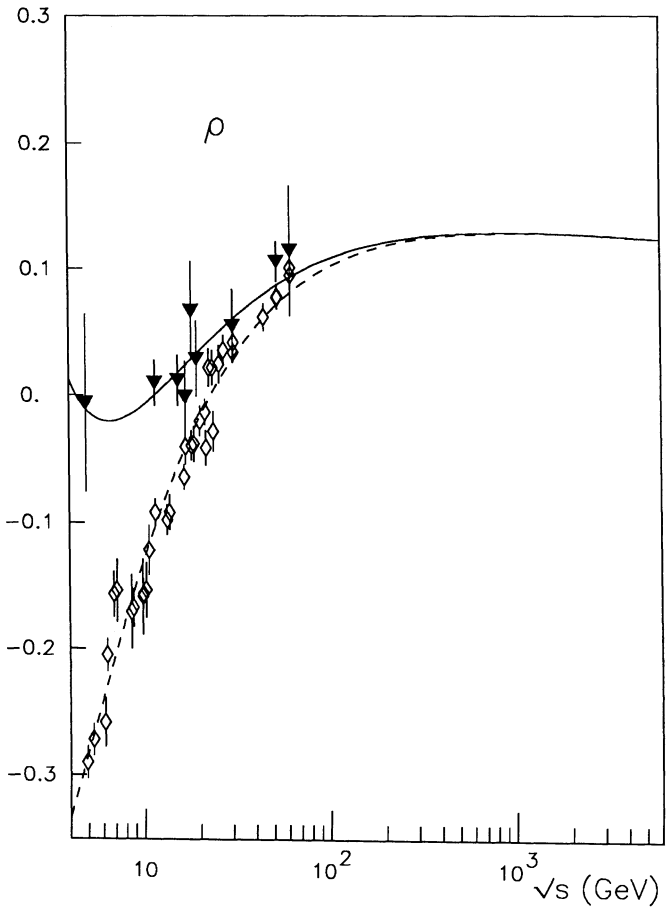

Figure 1.5: The ratio ρ for pp and $p\overline{p}$. The data are from reference [104]. The black triangles represent the $p\overline{p}$ data points, the open diamonds the pp data points. The dashed line corresponds to the ratio ρ for pp, the solid line corresponds to ρ for $p\overline{p}$. They were obtained by a dispersion relation fit through the data points using formula (1.27) and (1.33).

Chapter 2

Experimental set up

2.1 The Spp̄S Collider

The UA4 experiment is located at one of the long straight sections of the SPS (Super Proton Synchrotron) at CERN. The idea of using the SPS as a proton-antiproton collider, i.e. an accelerator in which bunches of protons and antiprotons circulate in opposite directions and collide head on, was proposed by Rubbia et al. in 1976 [32]. This plan could be realised because dense antiproton beams could be obtained with the stochastic cooling technique, which was invented by van der Meer [33].

In figure 2.1 an overview of the CERN p$\bar{\text{p}}$ complex is given [37], [38], [39]. A dense proton beam of 26 GeV is dumped on a copper target. The antiprotons, which are produced with a yield of approximately 2.10^{-6} per proton and an average momentum of 3.5 GeV/c per bunch, are collected and accumulated in the antiproton accumulator (AA). In the accumulator the antiprotons are 'cooled' and a stack of 10^{11} particles is gathered in 24 hours. Part of the high density core of the stack is injected in three bunches - each containing approximately 10^{10} particles - in the Proton Synchrotron (PS), where the bunches are accelerated up to 26 GeV/c. Finally the bunches are transferred to the SPS where they are accelerated up to a momentum of 273 $\pm$0.7 GeV/c.

They collide in six long straight sections of the SPS with three proton bunches, which circulate in the opposite direction and contain approximately 10^{11} particles. In this way a centre of mass energy of 546 GeV is reached. Under good conditions the beam has an average life-time of approximately 18 hours. At two intersection points large experimental underground areas were located. LSS5 contains the UA1 experiment [40], LSS4 the UA2 [41], UA4 [42] and UA5 [43] experiments.

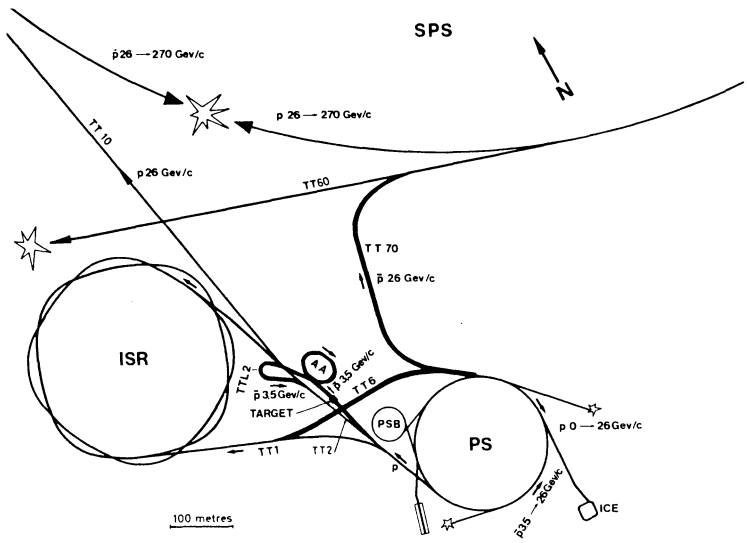

Figure 2.1: Overview of the proton-antiproton complex at CERN.

2.2 Beam optics

The particles in the SPS follow an equilibrium orbit, around which they oscillate. This orbit and the amplitude of the oscillations is determined by the particular focussing properties of the magnets. The trajectory of the particles can be described by Hill's equation [44]:

$$\frac{d^2z}{ds^2} + K(s)z = 0 \tag{2.1}$$

where z is the displacement perpendicular to the orbit (either in the vertical or in the horizontal direction), s is the distance along the accelerator, and $K(s)$ is the magnetic strength as a function of s. The solution of this equation can be written as:

$$z(s) = A\sqrt{\beta(s)}\cos(\mu(s) + \lambda) \tag{2.2}$$

with:

$$\mu(s) = \int_{s_0}^{s} \frac{1}{\beta(s')} ds' \tag{2.3}$$

where $\mu(s)$ is the relative phase around the orbit, $\beta(s)$ the betatron oscillation function and A is a constant. The angle of the particle with respect to the machine axis can be obtained by differentiating equation (2.2):

$$z'(s) = \frac{-A}{\sqrt{\beta(s)}}[\alpha(s)\cos(\mu(s) + \lambda) + \sin(\mu(s) + \lambda)] \tag{2.4}$$

with:

$$\alpha(s) = \frac{-1}{2}\frac{d\beta(s)}{ds} \tag{2.5}$$

The betatron oscillation function $\beta(s)$, the relative phase $\mu(s)$, and $\alpha(s)$ can be calculated from the values of the magnetic fields. For this purpose a matrix formulation is introduced [45], [46]. The matrix M relates the initial values for z and z′ at the position s_0 to the values at the position s:

$$\begin{pmatrix} z(s) \\ z'(s) \end{pmatrix} = M(s|s_0) \begin{pmatrix} z(s_0) \\ z'(s_0) \end{pmatrix} = \begin{pmatrix} M_{11} & M_{12} \\ M_{21} & M_{22} \end{pmatrix} \begin{pmatrix} z(s_0) \\ z'(s_0) \end{pmatrix} \tag{2.6}$$

It is useful to split the matrix M in sub-intervals in which the value of $K(s)$ is constant. Three cases should be considered: $K > 0$, $K = 0$ and $K < 0$, where the strength K can be expressed in the value of the magnetic field. The relevant elements in the SPS are focussing and defocussing quadrupoles and vacuum sections. A focussing quadrupole ($K > 0$)- in e.g. the horizontal plane - can be described by:

$$K > 0 \qquad M = \begin{pmatrix} \cos\phi & 1/\sqrt{K}\sin\phi \\ -\sqrt{K}\sin\phi & \cos\phi \end{pmatrix} \tag{2.7}$$

where $\phi = \sqrt{|K|}\, l$ and l is the length of the quadrupole. The same quadrupole is defocussing ($K < 0$) in the perpendicular i.e. vertical plane:

$$K < 0 \qquad M = \begin{pmatrix} \cosh\phi & 1/\sqrt{-K}\sinh\phi \\ \sqrt{-K}\sinh\phi & \cosh\phi \end{pmatrix} \tag{2.8}$$

For a vacuum section over a length l ($K = 0$) we obtain:

$$K = 0 \qquad M = \begin{pmatrix} 1 & l \\ 0 & 1 \end{pmatrix} \tag{2.9}$$

By simple matrix multiplication one obtains the matrix, which relates the values for z and z′ at position s to the values at s_0. Note that all matrices have a determinant which equals one. This means that there are not four but only three independent matrix-elements.

The matrix M can also be expressed in the three values for β, μ and α.

$$M(s|s_0) = \begin{pmatrix} \frac{\sqrt{\beta(s)}}{\sqrt{\beta(s_0)}}(\cos\Delta\mu + \alpha(s_0)\sin\Delta\mu) & \sqrt{\beta(s_0)\beta(s)}\sin\Delta\mu \\ -\left(\frac{(1+\alpha(s)\alpha(s_0))\sin\Delta\mu + (\alpha(s)-\alpha(s_0))\cos\Delta\mu}{\sqrt{\beta(s)\beta(s_0)}}\right) & \frac{\sqrt{\beta(s_0)}}{\sqrt{\beta(s)}}(\cos\Delta\mu - \alpha(s)\sin\Delta\mu) \end{pmatrix} \tag{2.10}$$

where $\Delta\mu$ is the phase difference $\mu(s) - \mu(s_0)$. In a circular machine - as the SPS - the matrix for one turn can be calculated. In that case $\beta(s) = \beta(s_0)$ and $\alpha(s) = \alpha(s_0)$ and the Twiss-matrix is obtained:

$$M_{\odot}(s|s) = \begin{pmatrix} \cos\mu(s) + \alpha(s)\sin\mu(s) & \beta(s)\sin\mu(s) \\ -\gamma(s)\sin\mu(s) & \cos\mu(s) - \alpha(s)\sin\mu(s) \end{pmatrix} \tag{2.11}$$

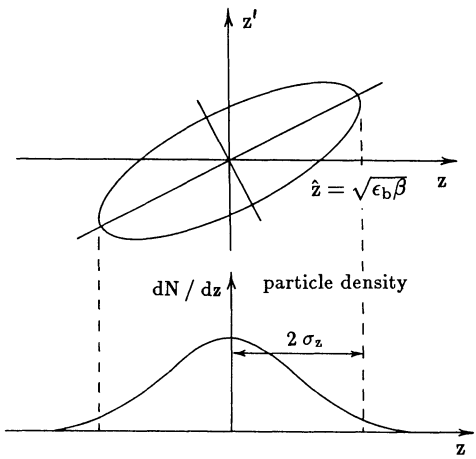

Figure 2.2: Ellipse in phase space of the machine

with:

$$\gamma(s) = \frac{1 + \alpha^2(s)}{\beta(s)} \tag{2.12}$$

From the machine properties and formula (2.11) the betatron amplitude $\beta(s)$, the phase $\mu(s)$, and the gradient $\alpha(s)$ can be calculated at any place around the accelerator.

A constant of motion can be derived from the solution of Hill's equation. If z is plotted against z' an ellipse in phase space is obtained (see figure 2.2):

$$A^2 = \frac{z^2}{\beta(s)} + \left(z' \sqrt{\beta(s)} + \frac{\alpha(s) z}{\sqrt{\beta(s)}} \right)^2 \tag{2.13}$$

This ellipse rotates through the machine and the area remains constant. It describes the motion of each particle in phase space. The particle emittance (E_p) is a constant of motion. It is proportional to the area of the ellipse and defined as:

$$E_p = A^2 \pi \equiv \pi \epsilon_p \tag{2.14}$$

It is useful to introduce the concept of beam emittance (E_b) [46]. In that case the phase space of the ellipse is filled with e.g. 10^{11} particles. The beam profile, i.e. the z projection of the ellipse, has a near gaussian shape. The beam emittance is arbitrarily defined in terms of the size of the beam (σ_z, one standard deviation of the distribution):

$$E_b = \frac{4 \sigma_z^2 \pi}{\beta(s)} \equiv \pi \epsilon_b \tag{2.15}$$

and size of the beam is:

$$\sigma_z = \frac{\sqrt{\epsilon_b \beta(s)}}{2} \tag{2.16}$$

The angular spread of the beam can be calculated by taking the z' projection of the distribution:

$$\sigma_{z'} = \frac{\sqrt{\epsilon_b \gamma(s)}}{2} \tag{2.17}$$

If the interaction point lies in the maximum or minimum of the betatron function ($\alpha(s) = 0$), the angular spread of the beam becomes:

$$\sigma_{z'} = \frac{1}{2}\sqrt{\frac{\epsilon_b}{\beta(s)}} \tag{2.18}$$

The luminosity (L), which is defined as the number of interactions per unit of cross section per unit of time, is an important parameter of the Collider. It can be expressed in the revolution frequency (f_0), the number of bunches (N_b), the number of colliding protons (N_p) and anti-protons ($N_{\bar{p}}$) and the horizontal (σ_h) and vertical (σ_v) size of the beam [47]:

$$L = \frac{f_0 N_b N_p N_{\bar{p}}}{4\pi\sigma_h \sigma_v} \tag{2.19}$$

For the SpS̄ $f_0 = 43.375$ kHz, $N_b = 3$,$N_p \approx 9.10^{10}$ and $N_{\bar{p}} \approx 5.10^9$. A high luminosity and event rate corresponds - according to formula (2.19) - to a small beam size. A small beam size corresponds to a low β in the interaction point and a small emittance ϵ_b of the beam. For the SpS̄ the emittance E_b after insertion of the bunches is 0.04-0.08 π.mm.mrad. The emittance steadily grows - mainly due to beam-beam scattering - with 0.003 π.mm.mrad per hour. This means that the beam blows up and the luminosity slowly decreases with time.

2.3 Super high beta optics

To detect scattered particles down to a momentum transfer squared $|t|$ of 0.001 GeV^2, extremely small angles up to 0.1 mrad should be reached. This means that the detector should be positioned at just a few millimeters from the centre of the beam and at approximately hundred meters from the interaction point. For this purpose a special setting of the magnets in the SpS̄ was studied and designed [48]. The following points should be considered. The minimum angle, which can be reached with a detector position z_{min} as close as possible to the beam, is:

$$\theta_{min} = \frac{z_{min}}{L_{eff}} \tag{2.20}$$

L_{eff} is the effective length which is equal to:

$$L_{eff} = |M_{12}| = |\sqrt{\beta\beta^*}\sin\Delta\mu| \tag{2.21}$$

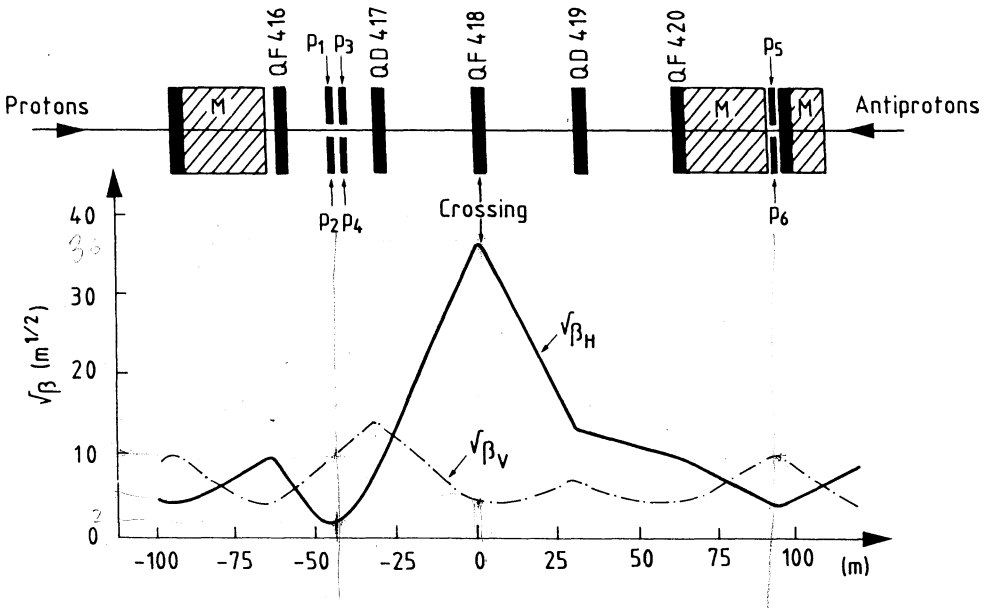

Figure 2.3: The values of the horizontal and vertical betatron function as a function of the position along the beam line and a lay out of the position of the different magnets (QD,QF and M) and the pots (P).

where β is the betatron function at the position of the detector, and β^* in the interaction point, $\Delta\mu$ is the phase difference. The minimum detector position, which can be reached is proportional to the beam size:

$$z_{\min} = C\sigma_z = C\frac{\sqrt{\epsilon_b \beta}}{2} \tag{2.22}$$

The constant C depends strongly on the background in the machine. It is known from previous measurements of UA4 and is approximately equal to 20 [9]. Substitution yields:

$$\theta_{\min} = \frac{C\sqrt{\epsilon_b}}{2\sqrt{\beta^*}\sin\Delta\mu} \tag{2.23}$$

This means that the smallest angles can be reached if β^* is very large, the phase difference $\Delta\mu$ equals $\frac{\pi}{2}$ and the emittance of the beam is small. This is the reason that a super high beta scheme was studied, and realised for this experiment.

A beta in the interaction point of 1086 m in the horizontal plane and 22.28 m in the vertical plane was chosen. In figure 2.3 $\sqrt{\beta}$ in the horizontal and vertical plane is plotted as a function of s. In the interaction point the highest $\sqrt{\beta_h}$ is reached. With an average emittance ϵ_b of 0.064 mm.mrad which was obtained during data taking, we get the following values for the size and angular spread of the beam at the interaction point (see table 2.1).

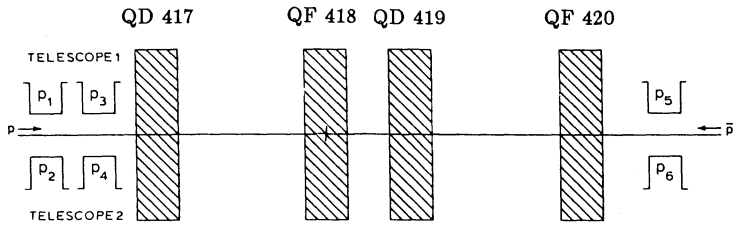

Figure 2.4: The set up with the numbering and position of the detectors in the Roman pots.

The super high beta optics has two peculiar features. First, the interaction point lies in the middle of a quadrupole magnet. Secondly, the highest beta value is exclusively obtained in the horizontal coordinate. In the standard high beta mode (100 m x 100 m) the beta was maximal in both coordinates. For the special super high beta optics new horizontal Roman pots (see section 2.4), which contain the detectors, were installed. At the left side two pairs of pots were placed at 43 m from the interaction point and 60 cm from each other. At the right side there was only place for one pair of pots at 94 m from the interaction point. In figure 2.4 the position and numbering of the pots along the beam line is sketched.

From the strength of the magnets K the matrix elements M, which relate the values of the position and angle at the interaction point at s_{int} = 0 cm to the corresponding values at the pot position, were calculated (see table 2.2). An examination of table 2.2 shows that there is a large asymmetry between left and right. The effective length L_h is approximately 60 m at the left side and 120 m at the right. For the vertical plane it is just the other way around: L_v is 27 m at the left side and 15 m at the right side. Note also that the effective length L_v is larger for pots 3 and 4 than for pots 1 and 2. This is caused by the special magnet settings and the sign of the matrix element M_{22}.

If the interaction point is shifted from s_{int} = 0 cm to s_{int} = -20 cm, new matrix elements (see table 2.3) can be obtained. If the matrix elements in table 2.2 and

Table 2.1 Beam parameters		
	σ_z	$\sigma_{z'}$
	mm	μrad
horizontal	4.2	3.8
vertical	0.59	27.

Table 2.2 Matrix elements for horizontal and vertical plane with s_{int} = 0 cm		
detectors	M_h	M_v
pot 1 and 2 $s = -4329.15$ cm	$\begin{pmatrix} 0.1926 & -5934.28 \\ 0.00009 & 2.4749 \end{pmatrix}$	$\begin{pmatrix} 1.0975 & -2740.12 \\ 0.0005 & -0.4564 \end{pmatrix}$
pot 3 and 4 $s = -4268.15$ cm	$\begin{pmatrix} 0.1980 & -5783.30 \\ 0.00009 & 2.4749 \end{pmatrix}$	$\begin{pmatrix} 1.1309 & -2767.95 \\ 0.0005 & -0.4564 \end{pmatrix}$
pot 5 and 6 $s = +9334.25$ cm	$\begin{pmatrix} -0.2660 & 12688.92 \\ -0.0009 & 0.5914 \end{pmatrix}$	$\begin{pmatrix} -1.5510 & 1575.48 \\ -0.0005 & -0.1056 \end{pmatrix}$

Table 2.3 Matrix elements for horizontal and vertical plane with s_{int} = -20 cm		
detectors	M_h	M_v
pot 1 and 2 $s = -4329.15$ cm	$\begin{pmatrix} 0.3681 & -5928.67 \\ 0.00002 & 2.4760 \end{pmatrix}$	$\begin{pmatrix} 1.0167 & -2718.97 \\ 0.0005 & -0.4455 \end{pmatrix}$
pot 3 and 4 $s = -4268.15$ cm	$\begin{pmatrix} 0.3690 & -5777.63 \\ 0.00002 & 2.4760 \end{pmatrix}$	$\begin{pmatrix} 1.0493 & -2746.15 \\ 0.0005 & -0.4455 \end{pmatrix}$
pot 5 and 6 $s = +9334.25$ cm	$\begin{pmatrix} -0.6413 & 12680.85 \\ -0.00011 & 0.5844 \end{pmatrix}$	$\begin{pmatrix} -1.5048 & 1544.92 \\ -0.0005 & -0.1152 \end{pmatrix}$

2.3 are compared, it can be seen that most of the matrix elements are stable within a few percent except the matrix elements M_{11} for the horizontal coordinate. This means that a change in the longitudinal position of the interaction point changes the value of the matrix element M_{11}. This effect is especially important if the beam has an off-set in the horizontal plane.

2.4 The detectors

The detector should be positioned as close to the beam as possible (i.e. inside the 20 cm wide cylindrical beam pipe) without disturbing the beam. For this purpose a special mechanical device, a Roman pot (see figure 2.5), has been designed [49], [50]. This type of device was used for the first time at the ISR [51]. The pot is cylindrical in shape with a diameter of 30 cm. It has a window (6 cm wide 12 cm high) of 0.1 mm thick steel to allow for the passage of particles. It contains the detector for elastically scattered particles.

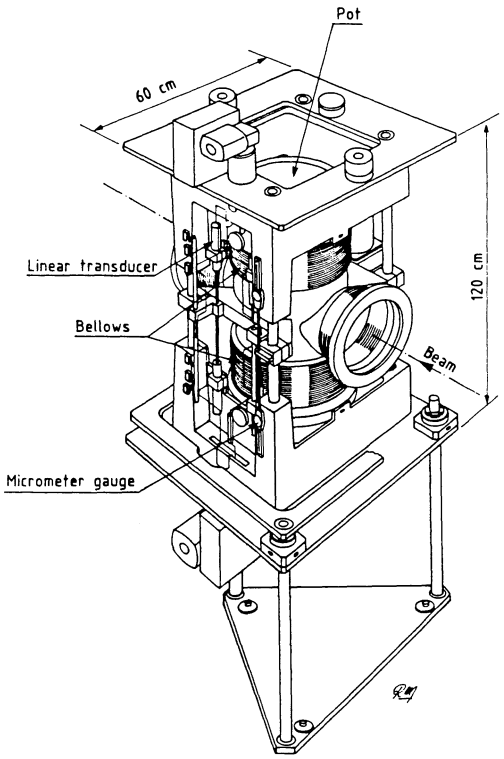

Figure 2.5: The construction of a pair of Roman pots, which contains two detectors.

During the injection and acceleration of the bunches in the Sp$\bar{p}$S the Roman pots are retracted at approximately 10 cm from the machine axis. If the beams have reached stable conditions, they are moved inwards by a low power electric motor. The pot position is determined by a potentiometric reading, which was calibrated with a micrometer gauge. An accuracy of 50 μm is obtained with a systematic uncertainty of 100 μm in the overall position of the pot with respect to the machine axis.

During data taking the pots were moved in as close to the beam as possible. The following pot positions (x_{min}) and minimum angles (θ_{min}) were reached for stack 6 (see table 2.4).

This corresponds to an absolute value for the minimum angle that is reached by the upper arm P1*P3*P6 and the lower arm P2*P4*P5 of $\pm$ 0.14 mrad. A minimum $|t|$-value of 0.0015 GeV^2 is thus reached.

Table 2.4 Pot positions and minimum angles		
pot number	x_{min}	θ_{min}
	(mm)	(mrad)
1	-6.985	-0.12
3	-7.97	-0.14
6	+13.955	-0.11
2	+8.135	+0.14
4	+8.01	+0.14
5	-11.355	+0.09

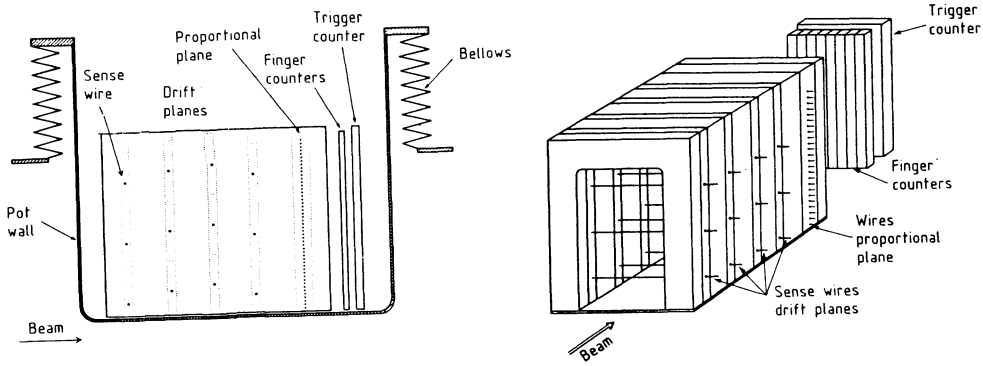

Figure 2.6: Schematic layout of the detector

To get an impression how close the detector was from the beam, the size of the beam and the ratio (C) of the average pot position and the beam size were calculated. The results for stack 6 are shown in table 2.5. At the left side only a C value of 29 could be reached. This was due to the background in the machine. At the right side it was possible to put the detector at 23 sigma's from the beam.

The detector, which is placed in the Roman pot, contains [49], [50]:
- a high-precision wire chamber with one proportional plane, and four drift planes,
- a hodoscope with eight finger counters,
- a trigger counter.

The drift part of the wire chamber consists of four planes with three drift cells. In our set-up the drift part measures the horizontal coordinate.[1] The proportional plane contains 24 resistive anode wires. The vertical coordinate is obtained by the

[1]In the other optics (high beta, normal beta, squeezed beta) the *vertical* coordinate was measured by the drift planes.

Table 2.5 The average pot positions and the size of the beam					
pot combination	position	$\sin\Delta\mu$	$\sqrt{(\beta_h)}$	σ_{beam}	C
	(mm)		$(\sqrt{m})$	(mm)	
1-2	7.56	-0.866	2.079	0.26	29
3-4	7.99	-0.792	2.216	0.28	29
5-6	12.66	0.831	4.464	0.56	23

charge division technique. The eight finger counters of the hodoscope are each 5.5 mm wide, 4 mm thick and 110 mm high. The finger counters are used to calibrate the proportional plane. The trigger counter is 45 mm wide, 5 mm thick and 110 mm high. A schematic layout of the detector is shown in figure 2.6. The information obtained with the detector is converted to an electronic signal, then amplified and finally carried with approximately 130 m long cables to the control room.

2.4.1 Calibration of the drift planes

Each drift plane is placed at 30 mm from the other plane and consists out of three drift cells. The drift cells are defined by the field shaping wires (with a relative distance of 2 mm) at ± 3 mm from the middle of the cell and two separation wires at 21 mm from the 'central' sense wire (see figure 2.7). The position of the first wire with respect to the bottom wall is different for each plane: it is respectively 9 mm, 17 mm, 21 mm and 13 mm for the first, second, third and fourth plane.

The lay out of the cell and the voltages applied to the field, separation and sense wires are carefully chosen to obtain a homogeneous drift field and constant

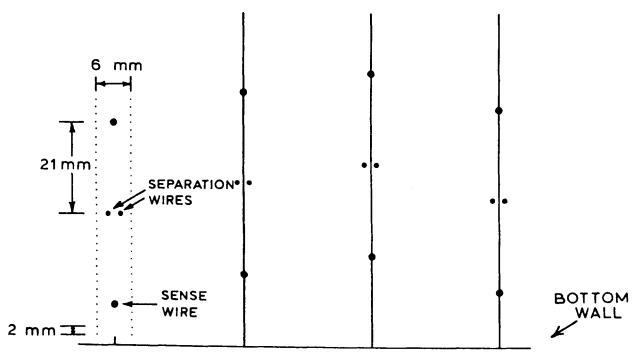

Figure 2.7: Geometry of the drift planes.

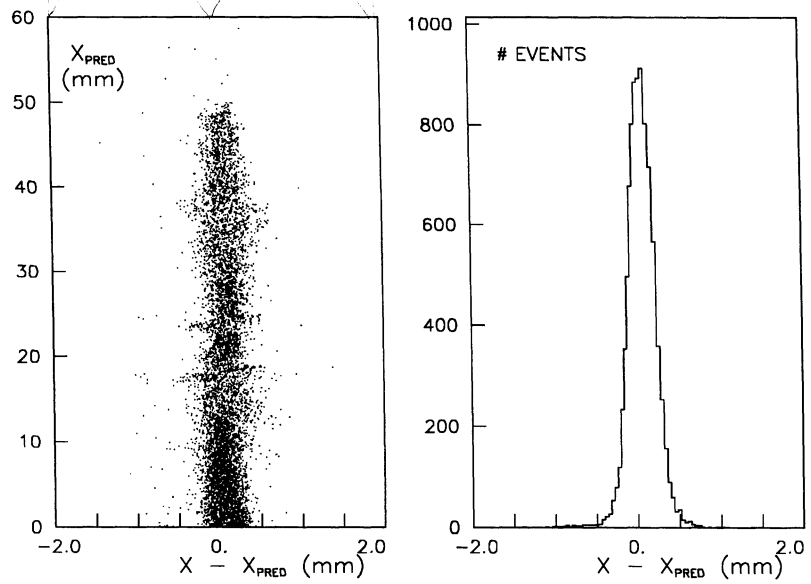

Figure 2.8: Calibration plot of x-x_{pred} vs. x_{pred} and projection.

drift velocity. Under standard operating conditions (anode voltage of 1.7 kV and drift potential -2.7 kV and a 50/50 argon-ethane mixture) a drift velocity of 52 μm/nsec is obtained. The drift times are measured by a time to digital converter (TDC) with multi-hit capacity. The time information is registered in bins of 1.5 nsec.

The calibration of the drift planes is performed using high quality straight-line tracks. The position is given by:

$$|x - x_{wire}| = v_d\,(t - t_0) \tag{2.24}$$

where x is the position, x_{wire} the wire position, t is the measured time, t_0 is the off-set time which is different for each wire and v_d is the drift velocity.

The absolute value in formula (2.24) introduces an ambiguity. This ambiguity can be resolved (because of the special geometry, which was chosen) by demanding more than two planes hit. The calibration of the drift planes consists of the determination of the t_0 values for each wire and the drift velocity for each cell. Usually the drift velocity is constant for the whole chamber.

The method of calibration is the following. The predicted value of the coordinate in a certain plane is calculated without using the information of that plane. Then the difference between the measured coordinate in that plane minus the predicted value (x-x_{pred}) is plotted as a function of the predicted coordinate (x_{pred}). If everything is calibrated well, figure 2.8 is obtained. If the t_0 is wrong by 1 nsec, a step near the wire position (see figure 2.9a; the wires are positioned at 21 mm

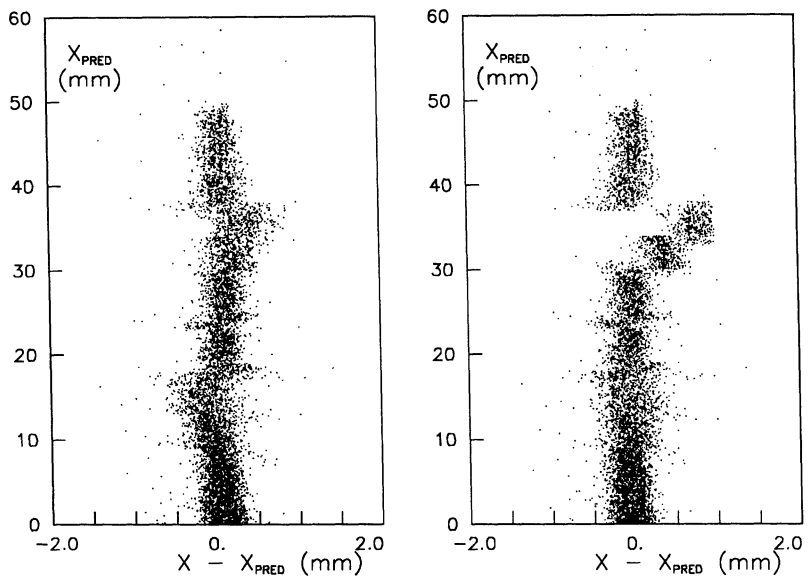

Figure 2.9: Calibration plot of x-x_{pred} vs. x_{pred} with a) a t_0 error of 1 nsec, and with b) a drift velocity error of 1 μm/nsec.

and 63 mm) can be seen. If the drift velocity is wrong by 1 μm/nsec, three regions with a constant deviation can be seen in the region between the separation wires of the different planes (see figure 2.9b, the separation wires for different planes are positioned respectively at 30, 38, 42 and 34 mm). These features enable us to calibrate the different planes.

The drift planes were calibrated for each stack. The error on the t_0 is less than 1 nsec. The error on the drift velocity is less than 0.4 μm/nsec for pots 1-4 and less than 0.2 μm/nsec for pot 5-6. The figures for the errors on the drift velocity are different, because only particles up to 20 mm from the bottom wall were detected at the left side. At the right side particles up to 50 mm from the bottom wall were detected, thus allowing for a more precise calibration. A single wire resolution of 150-180 μm was obtained during the run. This figure is larger than the single wire resolution of 80 μm, that was found in the test set up [49]. It is however slightly worse than the value of 130 μm, that was obtained during the high beta run [9].

2.4.2 Calibration of the proportional planes

The proportional plane consists of 24 resistive 64 mm long anode wires, spaced 4 mm from each other and with the first wire 4 mm from the bottom wall. The cathode wire planes are positioned at 6 mm from the anode wires. The anode wires

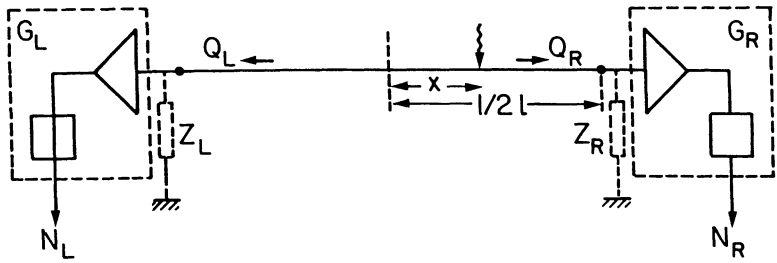

Figure 2.10: Scheme of the method of charge division

operate at ground potential, the cathode wires at -2.7 kV. The charge deposited on the wire (see figure 2.10) is preamplified by two current to voltage amplifiers, then integrated by a pulse shaping amplifier. Finally the signal is digitised by a peak sensing analogue to digital converter (ADC).

The position of the track can be obtained from the following formula:

$$y = 0.5\, l\, (1 + 2\beta)\frac{\alpha Q_L - Q_R}{\alpha Q_L + Q_R} \tag{2.25}$$

where Q is the charge deposited on the wire (L refers to the left side, R to the right side), l is the wire length, β is the ratio of the impedance of the amplifier (Z) and the wire resistance (R_w), and α is the ratio of the gains of the amplifiers. The constant $0.5\,l(1+2\beta)$ equals 35.6 mm, as was obtained with a test set up [49].

The value of the charge Q deposited on the wire can be obtained by taking the measured charge (Q^M) minus the pedestal (P):

$$Q_L = Q_L^M - P_L \tag{2.26}$$

$$Q_R = Q_R^M - P_R \tag{2.27}$$

The α values were determined before and after the run by pulsing the amplifiers. They are stable within 2 per mille. The pedestals correspond to the average noise level measured at the input of the ADC.

The pedestals (two per wire) are calibrated by matching the finger counter position with the proportional plane [49]. If the calibration is good a figure like 2.11 is obtained. If a calibration error in the difference of the pedestals (of 50 counts on an average pedestal of 80 counts) is made, the straight line - that fits the deviation from the finger position - is shifted with a constant value as can

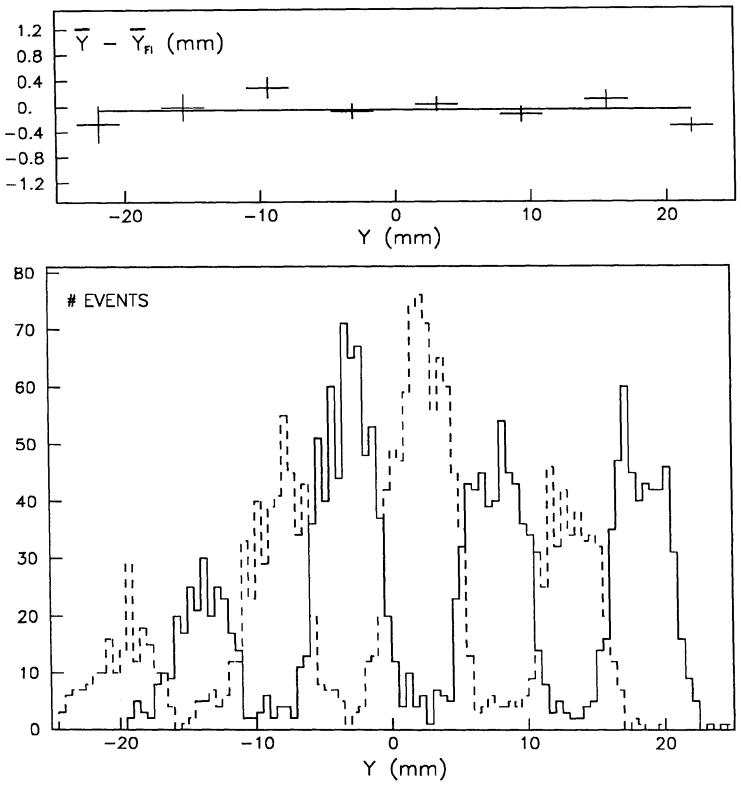

Figure 2.11: The vertical position measured by the finger counters (y_{fi}) and the proportional plane (y) as a function of y. The dashed line corresponds to a hit in the finger counters 1,3,5 or 7. The solid line to a hit in finger counters 2,4,6 or 8.

be seen in figure 2.12. If an error in the sum of the pedestals (of 50 counts) is made, the straight line has an angle as can be seen in figure 2.13. These features allow us to calibrate the pedestals. The calibration was performed for each stack individually.

The pedestals can also be measured directly by reading out the ADC's before and during the run. For the 1983 high beta run the pedestals, obtained by the match with the finger counters, were compatible with the pedestals measured before and during the run. Only small corrections of $\pm$ 20 counts had to be introduced [9].

For the super high beta run larger corrections were necessary. First, an average shift of the proportional plane with respect to the geometrical mean had to be introduced [53] (see table 2.6). Secondly, the pedestals obtained before and during the run were far from compatible with the pedestals obtained by the match

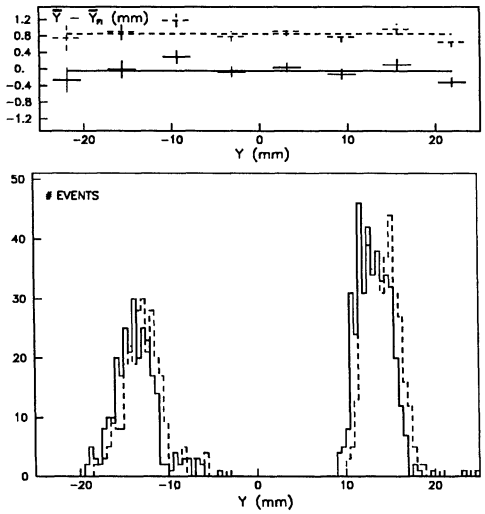

Figure 2.12: The vertical position measured by the finger counters (y_{fi}) and the proportional plane (y)- well calibrated (solid line) and with an error of 50 counts in the difference of the pedestals (dashed line)- as a function of y.

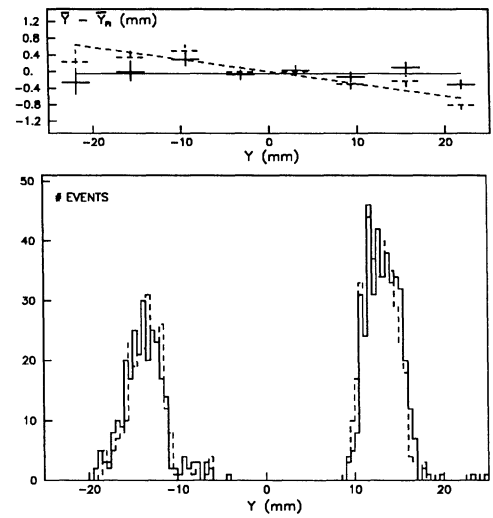

Figure 2.13: The vertical position measured by the finger counters (y_{fi}) and the proportional plane (y)- well calibrated (solid line) and with an error of 50 counts in the sum of the pedestals (dashed line)- as a function of y.

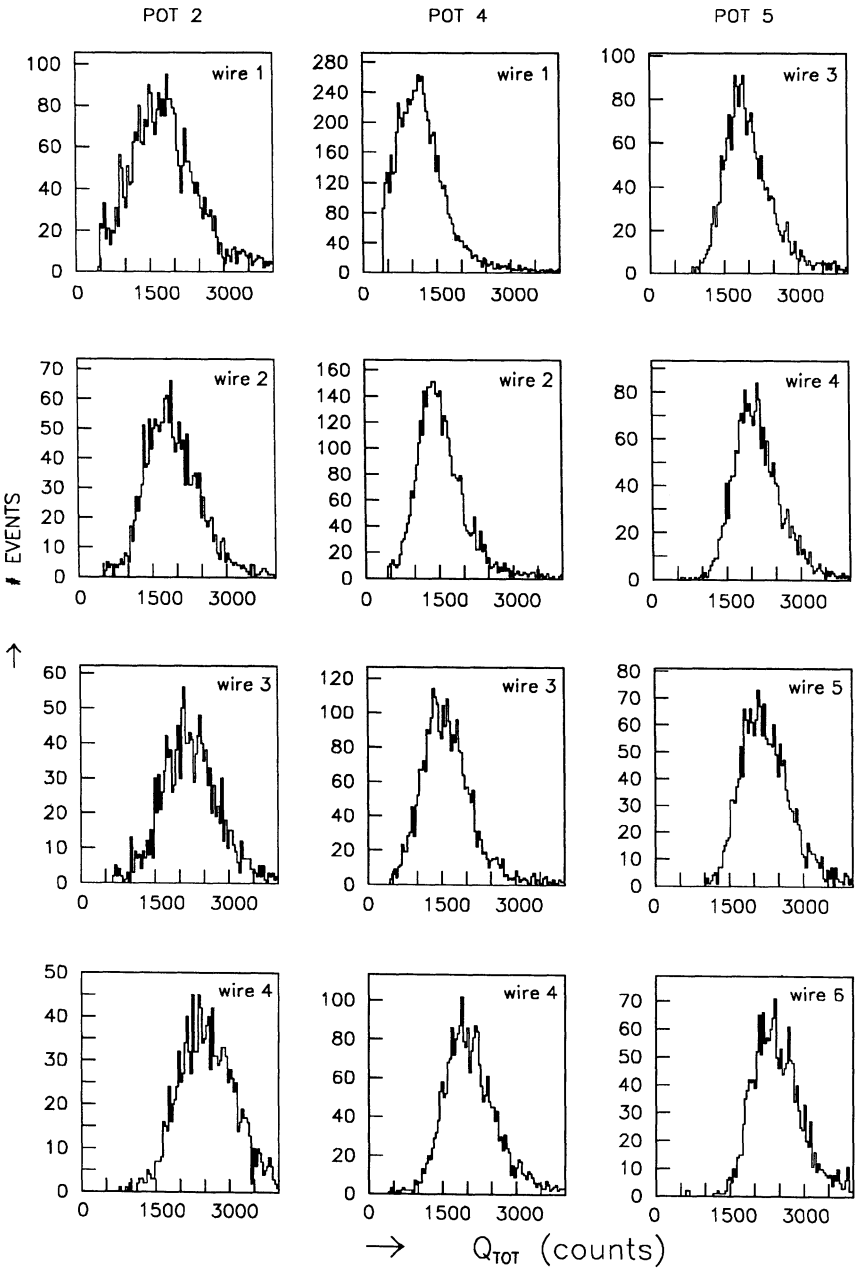

Figure 2.14: Total charge Q_{tot} for different wires in pot 2, 4 and 5

with the finger counters. Especially the pedestals for pots 1-4 were quite different from the pedestals measured before and during the run. Even negative pedestals had to be used. The explanation is the following. During the run the pots at the left side suffered from a large background. This background affected the pedestals.

Table 2.6 Off sets for the horizontal coordinate						
pot number	1	2	3	4	5	6
off set (mm)	0.0	-0.8	-0.7	0.3	-1.3	-0.2

The background had a second effect: it influenced the value of the total charge deposited on the proportional wire. Close to the beam the average total charge - defined as the average of the sum of the charge left (Q_L) and right (Q_R) - decreases. This is illustrated in figure 2.14 where the total charge Q_{tot} is plotted for different wires in pot 2, pot 4 and pot 5. We shall compare the three different pots. It is clear that the average total charge for pot 5 is highest and varies only a little bit as a function of the wire number. For pot 2 the average total charge decreases substantially, if the bottom wall is approached. In pot 4 this decrease is more severe. The same kind of behaviour was found for the other pot combination. Pots 3 and 4 suffered most from the background.

The decrease of the average total charge affects the resolution of the pots at the left side. This is shown in figure 2.15a where the difference of the coordinate

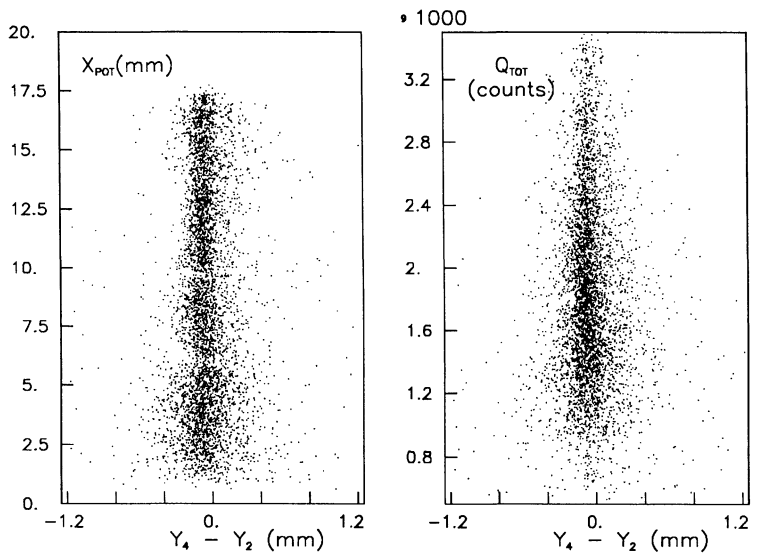

Figure 2.15: Difference of the vertical position measured by pot 4 and pot 2 (y_4 - y_2) versus a) the horizontal coordinate (x_{pot}) and b) the total charge (Q_{tot}) in pot 4.

measured in pot 4 and pot 2 - with a required total charge in pot 2 which is larger than 1500 - is plotted versus the horizontal position measured in pot 4. In figure 2.15b the same difference is plotted as a function of the total charge in pot 4. A higher total charge corresponds to a better resolution.

For pots 5 and 6 the resolution is approximately constant and equals 0.4 mm. For pots 1 and 2 the resolution varies from 0.5 mm far from the bottom plate till 1 mm at the bottom of the pot. For pots 3 and 4 the resolution is worse and varies from 0.7 mm till 2 mm at the bottom of the pot. The resolution obtained with pot 5 and 6 is the same as that obtained with the test set up [49]. The overall systematic uncertainty in the calibration of the proportional plane can be derived from the finger plots (figures 2.11-2.13). It is better than 200 μm in the middle of the wire and better than 500 μm at the extremes of the wire.

Chapter 3

The measurement of the real part

3.1 Data taking and processing

Data taking took place in a period of six days in June 1985, in which the Sp$\bar{p}$S operated in the described super high beta mode. In this period seven stacks of protons and antiprotons were successfully injected in the Sp$\bar{p}$S. Of these stacks six were analysed. Stack 2 was not analysed because of bad background conditions.

The triggering conditions were the following. An elastic-like event was demanded with either a threefold coincidence of the trigger counters in the 'upper' arm P1*P3*P6 or in the 'lower' arm P2*P4*P5. This signal was required to be in coincidence with the radio-frequency (RF) signal of the machine, which indicates a crossing of the circulating bunches. A veto was introduced in the case the PDP11 computer was busy or we had a fourfold coincidence P1*P3*P2*P4 - a so-called "splash" - in both telescopes at the left side. The trigger T was thus:

$$T = (P1 * P3 * P5 + P2 * P4 * P6) * RF * \overline{P1 * P3 * P2 * P4} * \overline{BUSY} \qquad (3.1)$$

In this way 850 000 triggers were collected for which all the information was read by the computer and written on tape. During data taking the trigger rate was 5-10 Hz with an average luminosity of 2. 10^{26} cm^{-2}s^{-1}.

A total of 64 datatapes (of 1600 BPI) was written. Data reduction took place in the following way.

(1) The relevant information for the calibration of the drift part of the chambers was written on five so-called NEVIS tapes. The complete calibration of the drift chambers resulting in the drift constants (t_0 and v_d) was carried out on these tapes.

(2) Datafiles were produced (selecting raw elastic-like events), that contained all the information of the fingers and proportional planes. With an iterative programme adjusting the pedestals step by step - using the measured α values - the pedestals of the proportional plane were determined.

(3) After the determination of the calibration constants data summary tapes (DST's) were written. These tapes contain all the physical information i.e. time

and distance of an event in the common reference frame. The calibration constants of the drift planes and the proportional planes, the pot positions, the geometry of the detectors - including small position corrections, which were measured by the SPS Survey group - and the values of the strength of the magnets were used as an input for the production of the DST's.

The events that were written on the DST's, had to satisfy the following criteria.
(i) At least two drift planes at the right side and four drift planes at the left side were required to be hit.
(ii) The angle of the reconstructed track in the telescope at the right side had to be less than $\pm$ 50 mrad and at the left side less than $\pm$ 10 mrad.
(iii) The number of hits in one pot recorded by the TDC's had to be less than 100.
The cuts (ii) and (iii) were required to remove 'junky events'. At this stage no cuts were made on the proportional plane. The charges of the three proportional wires, which were closest to the reconstructed track in the telescope, were written on the DST. The effects of these cuts on the efficiency will be discussed in the next section.

From the DST's a set of MINIDST's were produced. The MINIDST's contain the horizontal and vertical coordinate in the different drift planes, the total charge deposited on the proportional wires and some quantities - as e.g. the reconstructed interaction point - which can be calculated from both coordinates. Two additional cuts were introduced:
(1) The number of lines found in a telescope should be less than 10.
(2) The time of flight must lie in a window that corresponds to an elastic interaction. The time of flight (TOF) was measured by the trigger counters. In the TOF spectra both the incoming (anti)protons and the outgoing (anti)protons were present. By a cut the outgoing i.e. interacting (anti)protons could be selected.

The elastic candidates were selected by an algorithm that determines the best track combination of the right and left side. Therefore the quality of a track combination has to be defined. The best track combination:
(i) is collinear in the horizontal plane. Collinearity is defined (see formula (1.3)) in terms of the angle that can be calculated by dividing the measured coordinate by the effective length.
(ii) points to the interaction point if the track is extrapolated from the measured horizontal coordinates in the telescope at the *left* side.
(iii) is collinear in the vertical plane.
(iv) has the highest total charge deposited on the proportional wire.
The criterion that the track should point to the interaction region if the track is extrapolated from the *right* side was not included. This extrapolation is too sensitive to small systematic errors in the measurement of the horizontal coordinate, because of the small lever arm at the right side. The four criteria are listed in order of priority.

Extra attention was given to the proportional plane. An algorithm was developed to obtain the highest resolution in the vertical plane. If the track passed

between two neighbouring proportional wires the measured position (and the total charge) of two wires was combined. Secondly, the vertical coordinate at the *left* side was determined by taking the weighted average (in terms of the total charge, which is a reasonable measure for the resolution) of the measurements in the two pots. In practice it means that in most cases the measurement in pot 1 and 2 counts most.

The events that passed the cuts (1) and (2) and had the best track combination in terms of the criteria (i) till (iv) were written on the MINIDST.

3.2 Efficiencies

On MINIDST level a careful study of the efficiency of the horizontal and vertical planes was carried out. The efficiency of the drift planes was calculated by examining one plane, and putting severe constraints on the track (without using the information of the plane under examination). By looking if there is or is not a hit in the selected plane, the efficiency is determined. The result for pot 5 is shown in figure 3.1a, b and c. Small local inefficiencies can be seen. The total efficiency for the whole pot in the case we require 2 out of 4 planes hit (in fact only 3 planes were active) can be calculated easily. The result is shown in figure 3.1d.

The drift planes were carefully studied and a dead zone at the bottom of pot 3 of 430 μm was found. This is probably caused by the trigger counter, which was too short and started at approximately 400 μm from the bottom of the pot. Also periodical wiggles in the TDC spectra of pot 1 and the distribution of events were discovered. These oscillations were caused by the non-uniformity of the drift field. This was presumably due to space charge effects. The problem was solved by correcting the measured coordinate x (expressed in cm) according to the sine form of the wiggles:

$$\Delta x = 0.01 \sin \frac{2\pi(x - x_{wire})}{0.4} \tag{3.2}$$

The effect of this correction is further suppressed by calculating the horizontal coordinate at the left side - using the measured coordinate in pot 1 and 3 - by giving less weight to the measurement in pot 1. The result is a proper distribution of events with a total efficiency over the whole effective area that is better than 99 percent.

The efficiency of the proportional plane depends strongly on the minimum total charge Q_{min} which is required. If e.g. Q_{min} is only 200 counts - just above the pedestal - the efficiency goes to 100 percent. In that case however a lot of background and noise is marked as a good hit. Therefore the minimum charge should be raised to a level where it is highly probable that we have a real hit, that corresponds to an elastic event. The values for the minimum required charge per pot are listed in table 3.1.

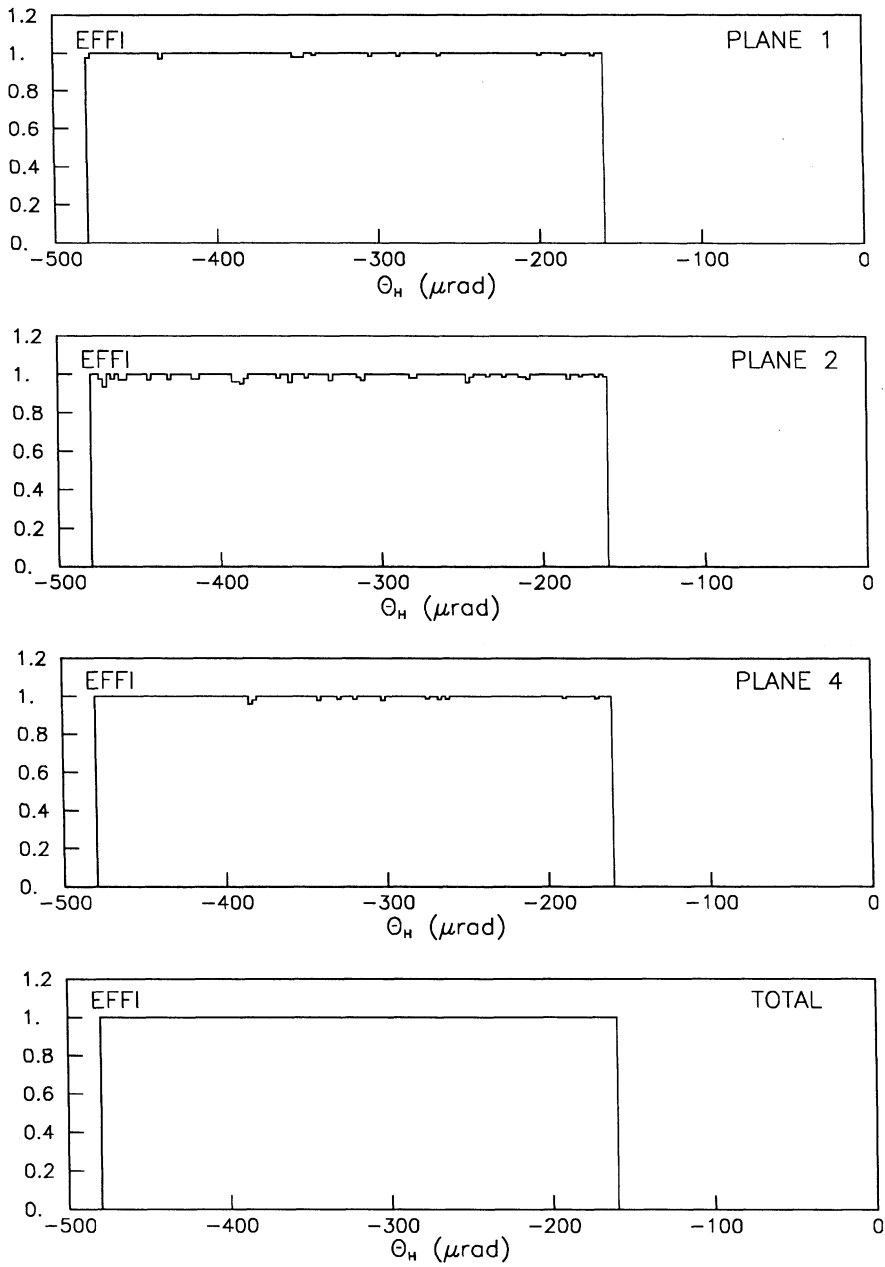

Figure 3.1: Efficiency for drift planes 1, 2 and 4 and total efficiency for pot 5 as a function of the horizontal angle.

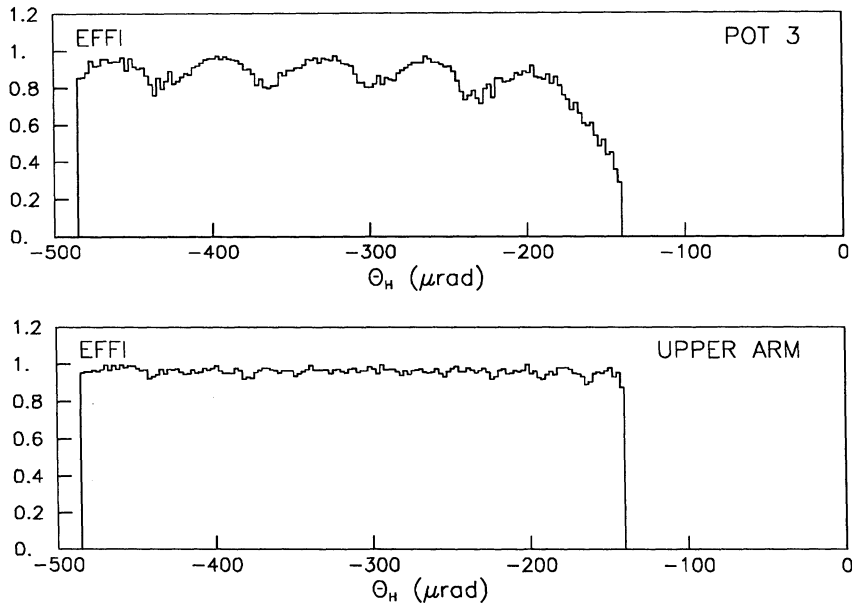

Figure 3.2: Efficiency for the proportional plane of pot 3 and total efficiency for planes of the upper arm vs. the horizontal angle.

Table 3.1 Minimum total charge per pot						
pot #	1	2	3	4	5	6
Q_{min}	700	700	850	850	900	900

The efficiency of the proportional planes was determined in a similar way as in the case of the drift planes. Severe constraints were put on the event asking an elastic-like event (leaving out the selected proportional plane). Then it is investigated whether or not there is a hit with a charge higher than Q_{min} in the selected proportional plane. The efficiency for pot 3 as a function of the horizontal angle is shown in figure 3.2a. The efficiency drops quickly if the bottom of the pot is approached. Large dips in the efficiency can be seen just in between two proportional wires. At these points the total charge drops. The total efficiency for the upper arm (see figure 3.2b) is better than the efficiency of pot 3, because only one out of two planes is required at the left side. The total efficiency of the proportional plane for both arms over the whole active area is better than 95 percent.

For the first proportional plane of pot 3 it was necessary to introduce a pedestal that changes linearly as a function of the horizontal coordinate (i.e. the drift distance to the proportional wire). This correction was at most 60 counts at the bottom of the pot (on an average pedestal of 100 counts for this wire).

The effect of this correction on the final vertical coordinate (and the distribution of events) is small, because not much weight is given to the measurement of

the vertical coordinate in pot 3.

3.3 Elastic events

Candidates for elastic events, that passed the selections (i) till (iii) and (1) and (2) (see section 3.1), have at least 4 drift planes and one proportional plane hit at the left side, and 2 drift planes and 1 proportional plane hit at the right side. The charge deposited on the proportional wire had to be larger than Q_{min}. To define the final set of elastic events three 3.5 sigma cuts were introduced.
(I) A cut on the horizontal extrapolation to the interaction point - $x_0(\overline{p})$ - from the left side was made. This quantity was calculated as follows:

$$x_0(\overline{p}) = M_{22}(\overline{p})x^t(\overline{p}) - M_{12}(\overline{p})\theta^t(\overline{p}) \tag{3.3}$$

where M_{22} and M_{12} are the horizontal matrix elements, $x^t(\overline{p})$ the position and $\theta^t(\overline{p})$ the angle measured in the telescope of the $\bar{p}$, i.e. left side.
(II) A collinearity cut in the horizontal plane was added. This quantity is defined as follows:

$$\Delta\theta_h = \frac{x(\overline{p})}{L_h(\overline{p})} + \frac{x(p)}{L_h(p)} \tag{3.4}$$

where L_h refers to the effective length and x to the measured horizontal coordinate in the telescope.
(III) A collinearity cut in the vertical plane was made. This quantity is defined as follows:

$$\Delta\theta_v = \frac{y(\overline{p})}{L_v(\overline{p})} + \frac{y(p)}{L_v(p)} \tag{3.5}$$

The distribution of events before the application of these successive cuts are shown in figure 3.3. The width (r.m.s.) of the extrapolation $x_0(\bar{p})$ after all cuts is 1.7 cm, the width of the horizontal collinearity $\Delta\theta_h$ is 8 μrad and the width of the vertical collinearity $\Delta\theta_v$ is equal to 55 μrad. The result of these cuts is a set of elastic events, that is uncorrected for the background.

A two dimensional distribution in θ_h and θ_v of elastic events is made to study the effect of additional cuts on the maximal and minimal vertical and horizontal angle. A confidence area in θ_h and θ_v is selected that is not affected by edge effects. In this area the slope b and the ratio ρ are stable. The distribution of events and the confidence area is shown in figures 3.4 and 3.5. The form of the confidence area is not rectangular, because a quadrupole shielded off the corners of the area. A total of 70 000 elastic events is left over after these cuts.

It is important to understand the precise width and off set of the six distributions of figure 3.3. The width of the collinearity distribution has four independent sources: the angular divergence of the beam (θ_b), the spread in the transverse

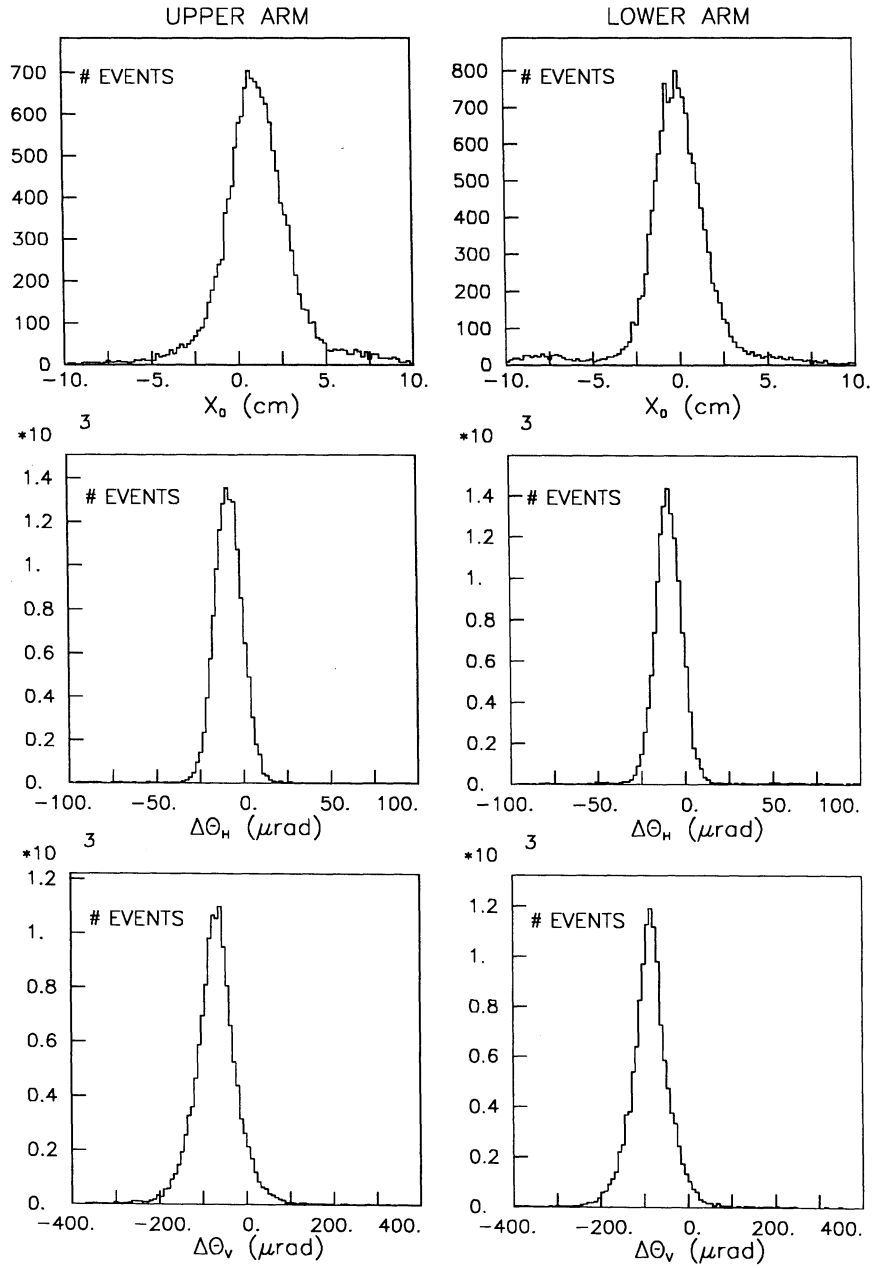

Figure 3.3: Successive cuts on the horizontal extrapolation, horizontal collinearity and vertical collinearity.

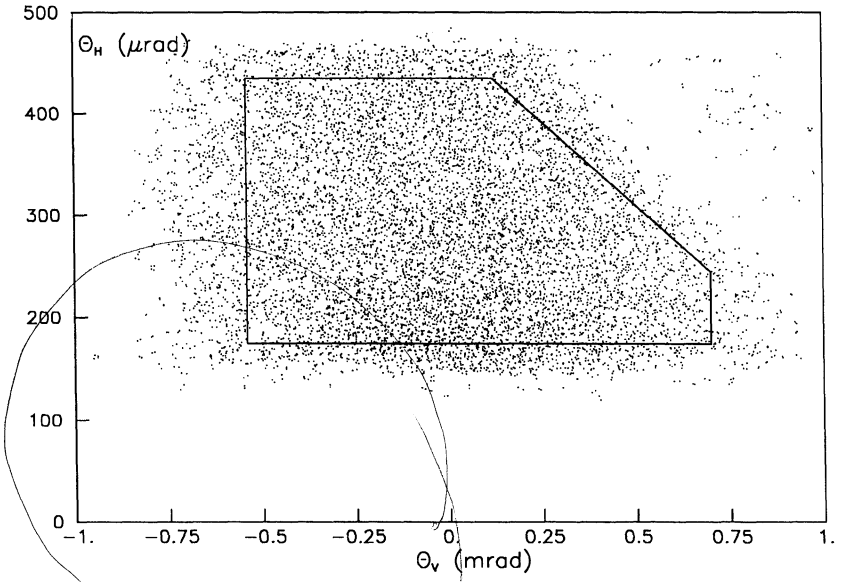

Figure 3.4: Distribution of events in the lower arm as a function of the horizontal and vertical angle.

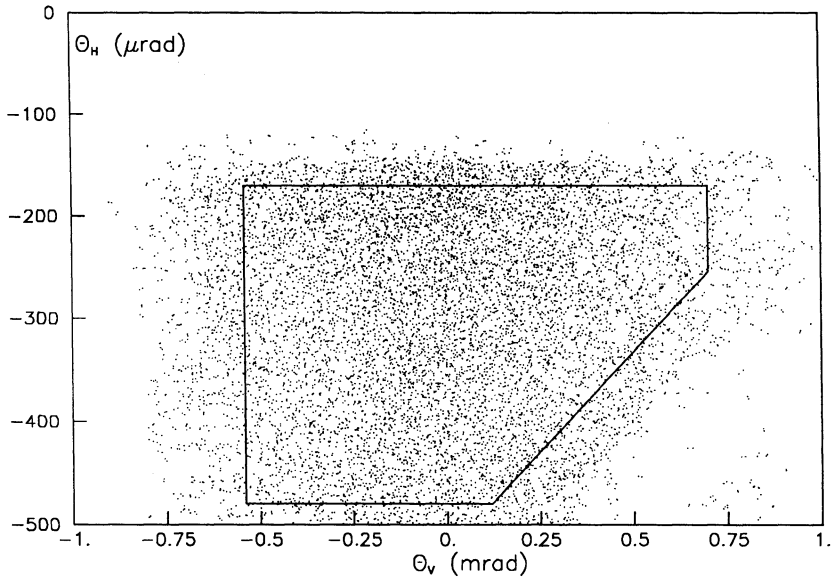

Figure 3.5: Distribution of events in the upper arm as a function of the horizontal and vertical angle.

position of the beam (σ_b), the longitudinal z (or s) spread of the beam (σ_z) and the resolution of the detector (σ_d) (see table 3.2).

The value of the longitudinal z spread of the beam is known from the bunch-length measurements at the SpS̄pS. During the super high beta run σ_z was 18 cm; a little bit larger than the 10 cm which was obtained in the lower beta modes. Note that the longitudinal spread of the beam gives a rather large contribution to the spread in the *horizontal* collinearity distribution. This is caused by the combination of an off-set of the beam and a large variation of the matrix elements as a function of the z position of the interaction point (see section 2.3).

Table 3.2 Width of the collinearity distributions

source	spread in $\Delta\theta_h$	spread in $\Delta\theta_v$
	μrad	μrad
θ_b	5.4	38.
σ_b	3.5	24.
σ_z	2.9	3.
σ_d	1.4	29.
total	7.6	57.
measured	$\approx$ 8.	$\approx$ 55.

The beam position can be calculated from the off-set of the collinearity distribution. The beam position varies from stack to stack and is on the average 6 mm in the horizontal plane and 1.5 mm in the vertical plane. These figures are compatible with the beam position and angle measurements (BPCS [52]) carried out by the SPS engineers.

An estimate for the residual systematic error on the measurement of both coordinates can be obtained. From the difference in the vertical collinearity (which is at maximum 20 μrad) a systematic error in the measurement of the vertical coordinate of 150 μm can be inferred. This is well below the estimate of 200 μm (see section 2.4.2).

From the variation of the values of extrapolation $x_0(\overline{p})$ a $\pm$ 50 μm error on the relative pot positions in one telescope can be derived. A maximal systematic error of $\pm$ 100 μm in the measurement of the horizontal coordinate can be obtained from the comparison of the extrapolation of the upper and lower arms. This is in perfect agreement with the estimate of 100 μm.

The second point, that has to be understood, is the difference - between both arms - of at most 5 μrad in the average value of the horizontal collinearity. Part of this difference is caused by the systematic uncertainty in the longitudinal (z) position of the interaction point. From the time of flight measurement the interaction point was calculated for each stack (see table 3.3).

Table 3.3 z of the interaction point

stack #	1	3	4	5	6	7
z (cm)	-19	4	2	0	-2	-7

This was done by measuring the difference in time between the incoming and outgoing protons and antiprotons at the left and right side. The systematic error on the determination of the z position of the interaction point is ± 5 cm [53]. This corresponds to a systematic error of ± 1 μrad in the difference of the horizontal collinearity. The rest can be explained in terms of a systematic error in the relative pot positions of both arms (i.e. the error in the difference between the pots in the upper and lower arms) of approximately 200 μm. This corresponds to a systematic error in the horizontal coordinate of each pot of approximately 100 μm. This is in agreement with the estimate (see section 2.4.1).

From the positions measured at the proton and antiproton side the final scattering angle is calculated. In principle this can be done in several ways, e.g. by using only the position measurements at the left or right side. In general we can take any combination of left and right with a weight λ (λ can be chosen freely from 0 till infinity):

$$\theta_{\rm h}^{\rm final} = \frac{{\rm x}(\overline{\rm p}) - \lambda {\rm x}({\rm p})}{L_{\rm h}(\overline{\rm p}) + \lambda L_{\rm h}({\rm p})} + \theta_{\rm h}^{\rm cor} \tag{3.6}$$

where the $\theta_{\rm h}^{\rm cor}$ is a constant correction angle. This angle can be expressed in the unknown beam position and the beam angle in the interaction point:

$$\theta_{\rm h}^{\rm cor} = \frac{M_{11}({\rm p}) - M_{11}(\overline{\rm p})}{L_{\rm h}(\overline{\rm p}) + L_{\rm h}({\rm p})} {\rm x}^{\rm beam} - \theta_{\rm h}^{\rm beam} \tag{3.7}$$

where x^{beam} and $\theta_{\rm h}^{\rm beam}$ are respectively the beam position and angle in the interaction point. An analogue formula can be written down for the vertical coordinate.

If the effective lengths at the right and left side are equal and the set up is symmetric, it is clear that the best value of λ - in terms of the error on the final angle - will be 1. In our (asymmetric) case it is found that the optimum value for λ equals -1 for one of the arms. The width of final horizontal angle in the lower arm becomes 19 μrad. This is only slightly better than the 20 μrad that corresponds to λ equals 1. This value will be used for the calculation of the final scattering angle.

The error on the elastic scattering angle $\theta^{\rm final}$ is calculated by Monte Carlo and shown in table 3.4.

Table 3.4 Spread on the final angle

source	spread in $\theta_{\rm h}^{\rm final}$	spread in $\theta_{\rm v}^{\rm final}$
	μrad	μrad
$\theta_{\rm b}$	2.9	19.
$\sigma_{\rm b}$	7.2	25.
$\sigma_{\rm z}$	18.	3.
$\sigma_{\rm d}$	1.0	13.
total	20.	34.

The spread on the final scattering angle in the horizontal coordinate is mainly caused by the spread in the z position of the interaction point. The angular spread of the beam and the spread in position of the beam contribute most to the spread in the vertical angle.

3.4 Results and checks

The correction angle θ^{cor} (see formula (3.7)) varies from stack to stack and can be determined by fitting both the upper and lower arm of the distribution. For the vertical coordinate it is possible to fit separately the upper and lower arm - centering the distribution - and eliminate thus the systematic shifts in this coordinate. For the horizontal coordinate this is not possible, because the distribution is split into two parts for the upper and lower arm. This implies that the systematic error between the upper and lower arm ($\Delta\theta_h^{arms}$ of $\pm$ 2 μrad as can be estimated from the systematic error in the relative distance of the pot positions in both arms) cannot be eliminated. This systematic error will enter in our systematic error on ρ.

Two types of fits were performed to extract the unknown parameters ρ, b, θ_h^{cor} and θ_v^{cor} from the distribution of elastic events.

(I) A maximum likelihood fit on the two dimensional θ_h and θ_v distribution using the formula (1.15) for the differential cross section gives the correction angle for each stack. This angle corresponds to an average (over all stacks) vertical beam angle of 90 μrad and a horizontal beam angle of 10 μrad. Both values agree very well with the values obtained by the BPCS measurements. The value of the correction angle was verified by checking that the ratio of events in both arms is flat as a function of θ_h, θ_v and t.

The final distribution of events is obtained after subtraction of the background. This background was measured by widening the strongest cut, which is in this case the cut on the horizontal collinearity. The background is less than 0.5 percent on the average, rising to 1.5 percent at very low t (i.e. θ_v and θ_h) values. From this distribution - correcting for the spread in the scattering angle and the efficiency of the detector - ρ and the slope b can be determined.

(II) The second method is the following. With a Monte Carlo the whole experiment is simulated: generating events according to the t-distribution using reasonable starting values for ρ and b and putting in the beam position and angle, introducing the spread on the angles, including the detector efficiencies, and using the angular cuts that define the confidence area. By dividing the number of events that were accepted by the number that were generated, the acceptance (as a function of $|t|$) was calculated.

The acceptance is shown in figure 3.6. The form of this distribution can be understood qualitatively in the following way. The minimum $|t_0|$ value of approximately 0.002 GeV^2 corresponds to the lowest scattering angle of 160 μrad. For higher $|t|$ values the acceptance (Acc) rises as, because of geometry:

$$\mathrm{Acc}(t) = \frac{2}{\pi}\arccos\left(\sqrt{\frac{|t_0|}{|t|}}\right) \tag{3.8}$$

The acceptance starts to drop after the highest horizontal angle θ_h is reached at $|t|$ approximately 0.015 GeV^2. Around $|t| \sim 0.03$ GeV^2 the magnet shade enters

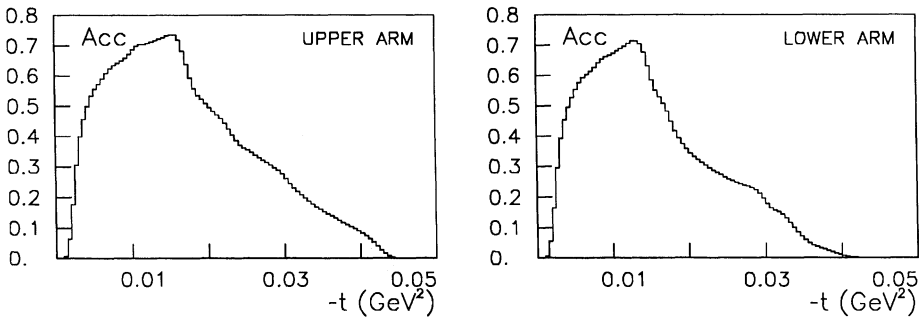

Figure 3.6: Acceptance (smoothed) as a function of $|t|$.

and a second breakpoint can be observed. The highest $|t|$ values 0.04-0.05 GeV^2 are fixed by the maximum scattering angles.

By dividing the observed distribution by the acceptance, a measured t-distribution can be formed. From this t-distribution ρ and the slope b can be determined with a simple χ^2 fit. The new values for ρ and b are used again as an input value for the t-distribution. The whole process is repeated until the acceptance and ρ stay the same. After two iterations a stable result was obtained.

The first fit was performed on the experimental t-distribution, as obtained with the second Monte Carlo method. The value of $(1+\rho^2)\,\sigma_{\rm tot}$ was fixed at the value which was measured before by the UA4 experiment: 63.3 $\pm$ 1.5 mb [8], [9]. The t-distribution was fitted in the $|t|$-interval of 0.002-0.035 GeV^2 with formula (1.15) leaving free the normalisation (or luminosity), the slope b and ρ. The result is $b =$ 15.5 $\pm$ 0.8 GeV^{-2} and $\rho = 0.23 \pm 0.04$ (statistical errors only). The value of the slope is perfectly compatible with the value of 15.3 $\pm$ 0.3 GeV^{-2} ([8], [9]) which was measured before by the UA4 experiment in the four-momentum transfer range of $0.03 < |t| < 0.10$ GeV^2.

In the final fit the slope b was fixed at 15.3 GeV^{-2}; the normalisation and ρ were left free. The result is $\rho = 0.238 \pm 0.024$, the quoted error is only statistical. In figure 3.7 the measured t-distribution and the result of the final fit are shown. The Coulomb and hadronic part of the differential cross section are shown too. The interference term is not shown. In figure 3.8 the ratio:

$$R(t) = (\frac{d\sigma}{dt})_{\rm meas}/(\frac{d\sigma}{dt})_{\rho=0} - 1 \qquad (3.9)$$

is plotted. It shows the effect of the interference term at low $|t|$ values. The data for the measured differential cross section are listed in table 3.5.

The systematic error on ρ has four main sources. First there is an error on the value of $(1+\rho^2)\,\sigma_{\rm tot}$, secondly an error on the slope b, thirdly a systematic error

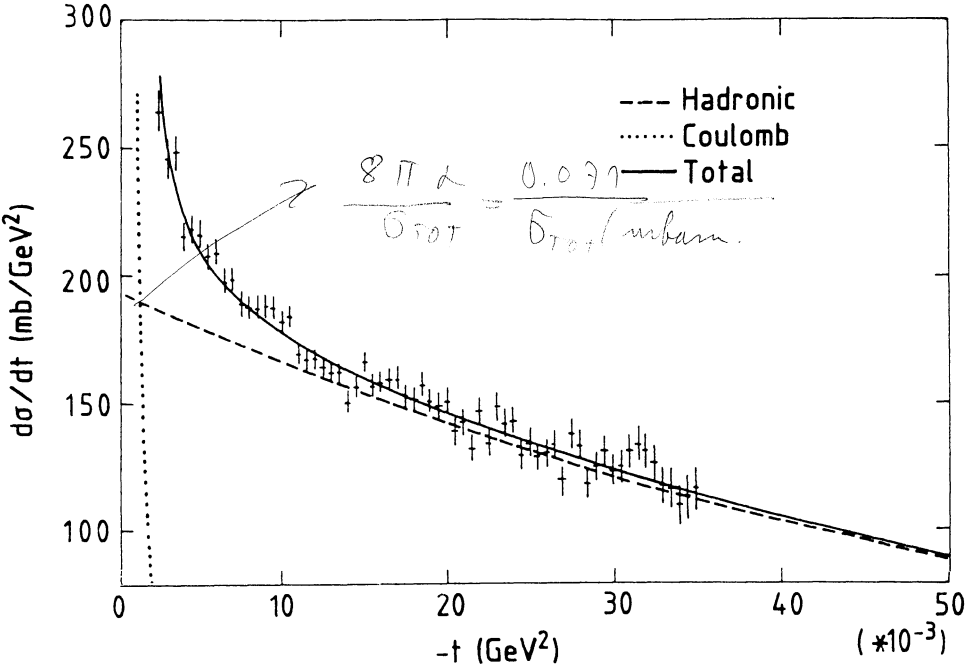

Figure 3.7: Measured differential cross section. Also shown is the final fit and the the Coulomb and hadronic contribution.

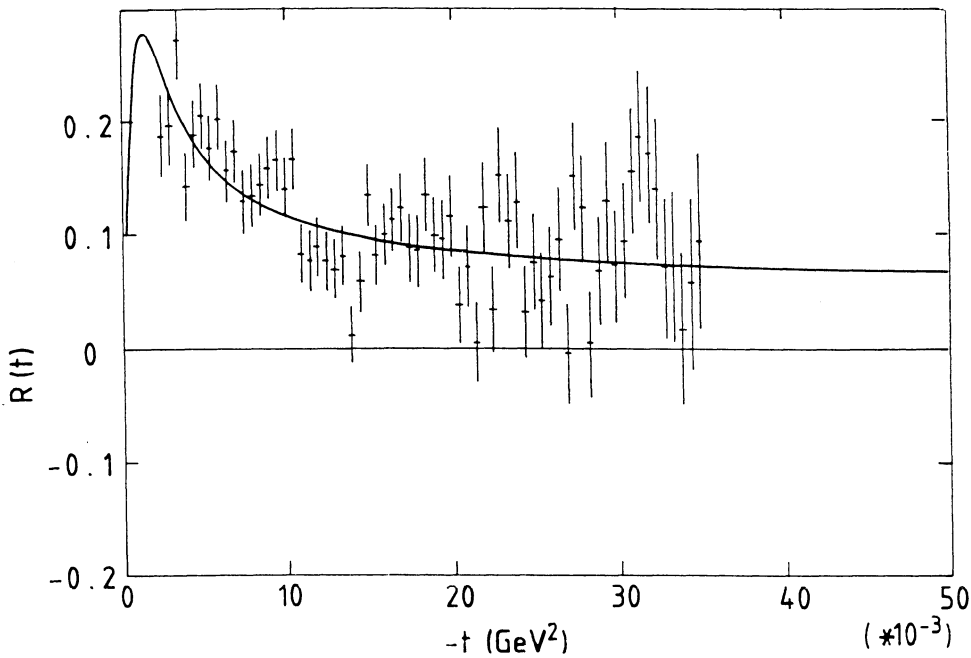

Figure 3.8: Measured ratio R(t). Also shown is the final fit.

Table 3.5. Measured differential cross section for $p\bar{p}$ at $\sqrt{s} = 546$ GeV

$\lvert t\rvert$	$d\sigma/dt$	error	$\lvert t\rvert$	$d\sigma/dt$	error
GeV^2 (10^{-3})	mb GeV^{-2}	mb GeV^{-2}	GeV^2 (10^{-3})	mb GeV^{-2}	mb GeV^{-2}
2.25	265.	8.	18.75	151.	5.
2.75	246.	7.	19.25	150.	5.
3.25	248.	6.	19.75	151.	5.
3.75	215.	6.	20.25	140.	5.
4.25	218.	5.	20.75	143.	5.
4.75	216.	5.	21.25	133.	5.
5.25	208.	5.	21.75	148.	5.
5.75	209.	5.	22.25	135.	5.
6.25	198.	5.	22.75	149.	5.
6.75	199.	5.	23.25	143.	5.
7.25	189.	4.	23.75	144.	5.
7.75	188.	4.	24.25	131.	5.
8.25	188.	4.	24.75	135.	5.
8.75	188.	4.	25.25	130.	5.
9.25	188.	4.	25.75	131.	5.
9.75	182.	4.	26.25	134.	6.
10.25	184.	4.	26.75	121.	5.
10.75	170.	4.	27.25	139.	6.
11.25	168.	4.	27.75	135.	6.
11.75	168.	4.	28.25	119.	5.
12.25	165.	4.	28.75	126.	6.
12.75	162.	4.	29.25	132.	6.
13.25	163.	4.	29.75	125.	6.
13.75	151.	4.	30.25	126.	6.
14.25	157.	4.	30.75	132.	6.
14.75	167.	4.	31.25	135.	7.
15.25	157.	4.	31.75	132.	7.
15.75	159.	4.	32.25	128.	7.
16.25	159.	4.	32.75	119.	7.
16.75	160.	4.	33.25	118.	7.
17.25	154.	4.	33.75	111.	7.
17.75	152.	4.	34.25	115.	8.
18.25	158.	5.	34.75	118.	8.

in the determination of the horizontal angle and finally a systematic error in the vertical angle.

As argued before, the systematic error on the vertical angle due to an overall shift in the proportional plane is eliminated. The only effect which is relevant is a linear error in the vertical coordinate that effects the value of the slope. The relative error in the vertical coordinate is estimated to be less than 5 per mille. The error on the slope is thus less than 0.2 GeV^{-2}. As the value of the slope is fixed in the final fit, it has a negligible effect on the final result for ρ.

The systematic error on $\Delta\theta_h^{arms}$ of $\pm$ 2 μrad will enter in our final result. The correlation is the following $\delta\rho/\Delta\theta_h^{arms} = 0.01\ \mu rad^{-1}$. The correlations in this t-range between ρ and the total cross section and ρ and the slope are resp. $\delta\rho/\delta\sigma_{tot} = 0.009\ mb^{-1}$ and $\delta\rho/\delta b = -0.044\ GeV^2$. There is however an anti-correlation which should be taken into account. If the slope is changed in the 1984 UA4 measurement, the total cross section changes too. The correlation can be calculated and equals $\delta\sigma_{tot}/\delta b = 4.4$ mb GeV^2. This implies that the effective correlation equals $\delta\rho/\delta b = -0.006\ GeV^2$. The final systematic error on ρ is 0.028 and is obtained by adding quadratically the independent errors. The main contribution to this error comes from $\Delta\theta_h^{arms}$.

The final result is $\rho_{p\bar{p}}(546\ GeV) = 0.24 \pm 0.04$ (statistical and systematical error summed quadratically).

The analysis with the first - maximum likelihood - method, which was carried out independently, yielded the same result. The behaviour of the slope parameter as a function of t was investigated by leaving out the low $|t|$ region. A fit in the interval 0.006-0.035 GeV^2 (fixing ρ at 0.24) yielded $b = 15.5 \pm 0.7\ GeV^{-2}$. The conclusion is that the slope is stable.

To be really sure about the ρ value a number of checks was carried out. The complete analysis was repeated, but now the final scattering angle was calculated exclusively with the coordinate from the left *or* the right side (taking λ equal to 0 or to infinite). If the coordinates at the left side were used, a value for ρ of 0.25 was obtained; in the other case a value for ρ of 0.23 was obtained. This small shift in the value for ρ is within the estimated systematic error.

The result was also checked against modifications of formula (1.15). It is e.g. possible that the elastic scattering amplitude has a spin-dependence. Therefore the spin-flip parameter η is introduced. In the simplest case the pure nuclear term has to be multiplied by $(1+\eta^2)$ [54]. Fixing the slope b at 15.3 GeV^{-2} and $(1+\rho^2)(1+\eta^2)\,\sigma_{tot}$ at 63.3 mb and leaving free the normalisation, a value for η of 0.008 $\pm$ 0.27 and ρ of 0.23 $\pm$ 0.025 (statistical errors only) is obtained. This means that the spin-flip term is compatible with zero. The final result for ρ remains unchanged.

A second point that was stressed by some authors [21], is the fact that the forward elastic slope b must have a t-dependence. Quite generally it is allowed (and theoretically plausible) that the slope of the real part is different from the

slope of the imaginary part. Two alternative hypotheses were examined. In the first case the slope is parametrised as:

$$b(t) = b_0 + \frac{b_1}{1 + t/t_0} \tag{3.10}$$

with t_0, b_0 and b_1 chosen such that $b(t)$ equals 17.2 GeV^{-2} at $|t|$=0 and drops to 15.7 GeV^{-2} at $|t|$=0.04 GeV^2 and to 15.3 GeV^{-2} at $|t|$=0.06 GeV^2. A fit to the data yields a ρ value which is 0.02 lower. In the second case a radical assumption was investigated. The slope of the real part was allowed to be two times the slope of the imaginary part, i.e. 30.6 GeV^{-2}. A steeper slope of the real part is excluded because of unitarity. A fit to the data gives a ρ value which is lowered by 0.03. All these effects stay within the quoted error.

As a final result is quoted $\rho_{p\overline{p}}$(546 GeV) = 0.24 $\pm$ 0.04. This means that the value of the total cross section, which was published before [8], [9] assuming a ρ value of 0.15, has to be changed into $\sigma_{p\overline{p}}$(546 GeV)= 60 $\pm$ 1.5 mb.

Chapter 4

Dispersion relations

4.1 Expectations and implications

The measured value for $\rho_{p\overline{p}}$ at 546 GeV of 0.24 ± 0.04 is almost twice the value of 0.12-0.14 that is predicted by most of the models [16] for elastic scattering. The main question is: what does the high ρ value imply? The most straight forward - but rather vague - answer is that the total cross section must behave in a new unexpected way in the high energy domain.

The basic hypothesis, which is made by most of these models, is the statement that asymptotically:

$$\sigma_{pp} = \sigma_{p\overline{p}} = C_3 \ln^{\gamma}(s/s_0) \tag{4.1}$$

with γ approximately equal to 2. This assumption should be reconsidered. Other assumptions could be questioned too, as e.g. the analyticity of the elastic scattering amplitude, the causality of the interaction or the Froissart-Martin bound (1.21). It is however unlikely that one of these assumptions is incorrect, because each of them is based on firm theoretical grounds.

The implications that can be drawn from qualitative arguments based on derivative or integral dispersion relations are twofold:
(1) either the total cross sections for pp and $p\overline{p}$ stay the same - the even scenario - and rise steeper than the assumed $\ln^2(s/s_0)$ of the Amaldi parametrisation (though asymptotically the Froissart-Martin bound is still respected);
(2) or the total cross section for pp and $p\overline{p}$ are asymptotically different - the odd scenario - and the pp and $p\overline{p}$ cross each other around $\sqrt{s} \sim 100$ GeV; and
(3) a combination of options (1) and (2).

In this chapter the even and odd scenario will be investigated. Precise, quantitative predictions for the behaviour of the total cross section will be derived using the dispersion relations. A dispersion relation analysis has the advantage that it is model independent as no specific assumptions (of the type Eq.(4.1)) on the behaviour of the total cross section have to be made. In the past this type of analysis proved to be a reliable method to obtain predictions for the total cross section in a new energy domain [3], [4], [27], [28].

4.2 Dispersion relation analysis

In the first scenario it is assumed that the elastic scattering amplitude is asymptotically an even function of the energy i.e. that the total cross section for pp and $p\overline{p}$ are asymptotically the same. In that case the once subtracted dispersion relation 1.33 may be used.

First a more general approach is followed to derive the consequences of the high ρ value. Secondly two more specific models are presented.

A parametrisation of the total cross section was constructed, which (a) is a smooth continuous function of the energy, (b) has the usual "low-energy" behaviour (1.27), (c) respects asymptotically the Froissart-Martin bound and (d) at energies above 546 GeV allows for a steep local rise:

$$\sigma^{}_{\substack{pp \\ p\overline{p}}} = \sigma^{\text{Regge}}_{\substack{pp \\ p\overline{p}}} + C_4 \ln^2(s/s_0) f^{\text{even}}_{\text{viol}}(E) \tag{4.2}$$

The violating function $f^{\text{even}}_{\text{viol}}$ was chosen such that for energies lower than E_1 it goes to 1; for higher energies up to E_2 the function can rise as steeply as we wish:

$$f^{\text{even}}_{\text{viol}}(E) = \frac{1+(E/E_1)^\lambda}{1+(E/E_2)^\lambda} \frac{D}{1+(E/E_3)^\mu} \tag{4.3}$$

μ equals 0 determines the upper limit of the rise; for μ greater than 0 the cross section falls off for energies greater than E_3. Of course $E_1 << E_2$, $E_1 << E_3$, $\lambda \geq 0$ and $\mu \geq 0$. D is a constant.

The free parameters are tuned to admit different kinds of high energy behaviour. Every parametrisation of the total cross section of the form (4.2) was accepted, which yielded a $\rho_{p\overline{p}}$ value of 0.24 ± 0.04 at $\sqrt{s} = 546$ GeV, with the constraint that the total cross section at $\sqrt{s} = 546$ GeV must be equal to 60 ± 2 mb. At ISR energies the deviation from the Amaldi parametrisation (1.27) is allowed to be at most 0.50 mb. The maximum allowed rise of the total cross section is 25 mb per TeV. A much steeper rise (due to e.g. a sharp resonance) is for physical reasons rather unlikely.

The results - a shaded area which represents all possible parametrisations - are shown in figure 4.1 and summarised in table 4.1.

One observes a steep rise of the total cross section; much steeper than $\ln^2(s)$, which is plotted in the same figure. The predictive power of this analysis is limited to energies below approximately 4 TeV. The measurement of the total cross section by UA5 at 900 GeV, which yields 65.3 ± 2.2 mb [55], is fully compatible with our prediction.

The set of parametrisations of the total cross section (4.2) is only useful to obtain lower and upper bounds for the behaviour of the total cross section. A more specific parametrisation - using a threshold at s_{cut} - which has the proper asymptotic behaviour and satisfies theoretical constraints is:

$$\sigma^{}_{\substack{pp \\ p\overline{p}}} = \sigma^{\text{Regge}}_{\substack{pp \\ p\overline{p}}} + C_4 \ln^\gamma(s/s_0) + C_5\, \theta(s - s_{\text{cut}}) \ln^2(s/s_{\text{cut}}) \tag{4.4}$$

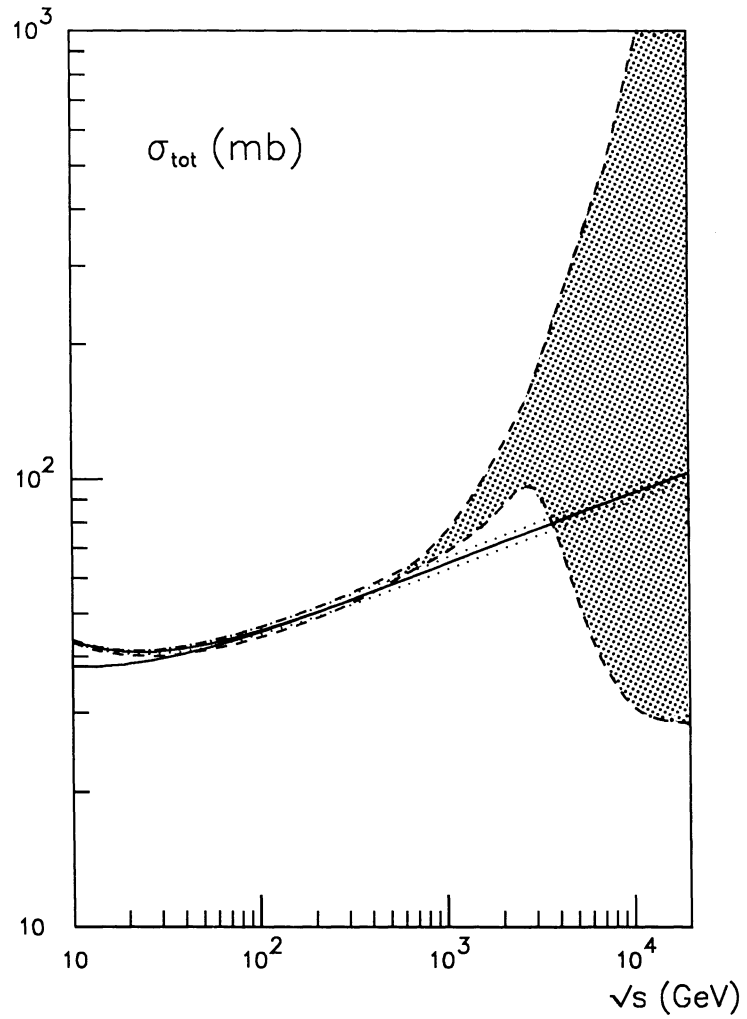

Figure 4.1: The total cross section for pp and $p\overline{p}$ as a function of the energy. The shaded area is obtained by the dispersion relation analysis in the even scenario. The continuous curve represents the $\ln^2(s)$ expectation, the dotted curves the one-standard-deviations in the constant in front of the $\ln^2(s)$.

$\sqrt{s}$	$\sigma_{\rm tot}^{\rm pred}$	$\sigma_{\rm tot}^{\rm stand}$
TeV	mb	mb
0.9	69. $\pm$3.	65.0
1.6	90. $\pm$11.	71.2
2.0	104 $\pm$16.	73.7
4.0	150. $\pm$80.	82.2
6.0	200. $\pm$160.	86.5

Table 4.1: Predictions for the total cross section using the dispersion relation analysis ($\sigma_{\rm tot}^{\rm pred}$) to be compared with the $\ln^2(s)$ (1.27) extrapolation ($\sigma_{\rm tot}^{\rm stand}$). The errors given should be considered as the upper and lower bounds.

where $\theta(s)$ is a step-function. The constants $s_{\rm cut}$ and s_0 are not prescribed by theory (see e.g. formula (1.21)) and can be chosen arbitrarily. The amplitude, which corresponds to this cross section, can easily be incorporated in most of the models. The physical interpretation of this formula is clear: there is a process which sets on at $s = s_{\rm cut}$ with a $\ln^2(s/s_{\rm cut})$ dependence.

The dispersion relation (1.33) with the input formula (4.4) was fitted to the existing data for ρ and $\sigma_{\rm tot}$ up to 546 GeV [104], fixing s_0 at 1.0 GeV^2 and leaving free all 10 constants. The result is plotted in figure 4.2. The fit agrees very well with the UA4 ρ measurement.

The fit gives $C_5 = 4^{+58}_{-2}$ mb, $\sqrt{s_{\rm cut}} = 500^{+1300}_{-100}$ GeV and a $\chi^2/NDF = 161.7/143$. The constant C_5 and $\sqrt{s_{\rm cut}}$ are strongly correlated. The lower limit is fixed by the data, the upper limit by the Froissart-Martin bound. The UA5 point [55] was not used in this fit, because their result was obtained using certain assumptions on the high energy behaviour of the ratio of the elastic to the total cross section. If the UA5 point - summing statistical and systematical errors - is included, $C_5 = 15^{+47}_{-5}$ mb, $\sqrt{s_{\rm cut}} = 900^{+800}_{-200}$ GeV and a $\chi^2/NDF = 161.5/144$ is obtained.

We also searched for a continuous parametrisation - without a threshold - which is the analogue of formula (4.4). One of the simplest forms is:

$$\sigma_{\substack{\rm pp\\ \rm p\overline{p}}} = \sigma_{\substack{\rm Regge\\ \rm pp\\ \rm p\overline{p}}} + C_4 \ln^\gamma(s/s_0) + C_5 \ln^2(1 + s/s_1) \qquad (4.5)$$

A fit to the data (again first leaving out the UA5 point) yields: $C_5 = 6^{+56}_{-3}$ mb and $\sqrt{s_1} = 700^{+1700}_{-200}$ GeV with a $\chi^2/NDF = 162.5/143$. If the UA5 point is included, $C_5 = 14^{+48}_{-7}$ mb and $\sqrt{s_1} = 1200^{+1200}_{-300}$ GeV with a $\chi^2/NDF = 164.1/144$ is obtained. There are no noticeable differences between the cross sections for pp and p$\overline{\rm p}$ above $\sqrt{s} \sim 300$ GeV. The results of these fits for $\sigma_{\rm tot}$ and ρ are shown in figure 4.3 and summarised in table 4.2.

To get an impression of the sensitivity of the results to the value of $\rho_{\rm p\overline{p}}$ at $\sqrt{s} = 546$ GeV Eq.(4.5) was also fitted with $\rho_{\rm p\overline{p}} = 0.20 \pm 0.04$ at the same

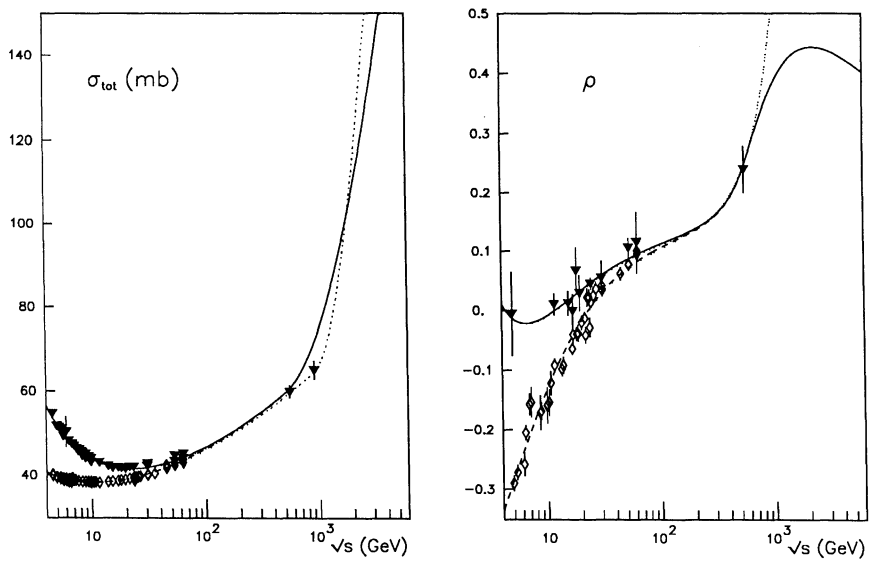

Figure 4.2: The total cross section and the ratio ρ for pp and $p\overline{p}$ as a function of the energy. The black triangles represent the $p\overline{p}$, the open diamonds the pp data points [104]. The solid (for $p\overline{p}$) and dashed (for pp) curves are obtained without the UA5 point [55] in the fit, using a parametrisation with a threshold (4.4), for the dotted curves the UA5 point was included.

	$\rho_{p\overline{p}} = 0.24$		$\rho_{p\overline{p}} = 0.20$	
$\sqrt{s}$	$\sigma^{pred}_{\substack{pp\\p\overline{p}}}$	$\rho^{pred}_{\substack{pp\\p\overline{p}}}$	$\sigma^{pred}_{\substack{pp\\p\overline{p}}}$	$\rho^{pred}_{\substack{pp\\p\overline{p}}}$
TeV	mb		mb	
0.9	71.	0.34	69.	0.24
1.6	92.	0.44	84.	0.29
2.0	103.	0.47	90.	0.30
4.0	157.	0.48	118.	0.31
10.0	265.	0.42	169.	0.30
40.0	510.	0.33	274.	0.25

Table 4.2: Predictions for the pp and $p\overline{p}$ cross sections and ρ using Eq.(4.5) with $\sqrt{s_1} = 700$ GeV, $\rho = 0.24$ and with $\sqrt{s_1} = 500$ GeV, $\rho = 0.20$.

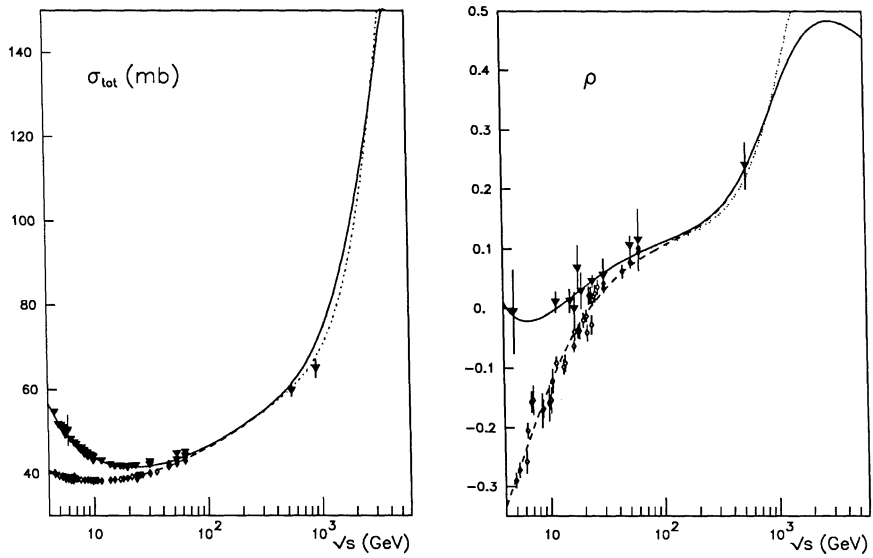

Figure 4.3: The total cross section and the ratio ρ for pp and $p\overline{p}$ as a function of the energy. The black triangles represent the $p\overline{p}$, the open diamonds the pp data points [104]. The solid (for $p\overline{p}$) and dashed (for pp curves are obtained without the UA5 point in the fit, using a continuous parametrisation (4.5), for the dotted curves the UA5 point was included.

energy. Leaving out the UA5 point $C_5 = 4^{+58}_{-3}$ mb and $\sqrt{s_1} = 500^{+1400}_{-150}$ GeV with a $\chi^2/NDF = 162.8/143$ is obtained. The results of this fit for $\sigma_{\rm tot}$ and ρ are also given in table 2. Note that the predictions are very sensitive to the $\rho_{p\overline{p}}$ value.

In the second scenario an odd term at infinite energies is allowed and the total cross sections for pp and $p\overline{p}$ are allowed to be asymptotically different [57], [58]. In that case the twice subtracted dispersion relation formula (1.32) should be used. As before first a more general approach is followed and then a more specific model is presented. To obtain the implications of this hypothesis additional assumptions should be made. First the constant A_1 in formula (1.32) should be fixed at the value obtained by a fit through all the data points [104] leaving out the UA4 measurement. The behaviour of the $p\overline{p}$ cross section up to 546 GeV is constrained by the measurement of the total cross section by UA4. This means that it is possible to use the standard Amaldi parametrisation for the $p\overline{p}$ cross section, with γ equals 2:

$$\sigma_{p\overline{p}} = \sigma^{\rm Regge}_{p\overline{p}} + C_4 \ln^2(s/s_0) \tag{4.6}$$

For the pp total cross section a parametrisation was constructed, which (a) is a smooth continuous function of the energy, (b) has the usual "low-energy"

$\sqrt{s}$	σ_{pp}^{pred}	$\sigma_{p\bar{p}}^{stand}$
TeV	mb	mb
0.546	67 ±2.	60.0
0.9	76 ±4.	65.0
1.6	92. ±10.	71.2
2.0	100.±14.	73.7
4.0	148. ±42.	82.2
10.0	350. ±200.	94.5

Table 4.3: Predictions for the pp cross section using the dispersion relation analysis (σ_{pp}^{pred}) and the $\ln^2(s)$ (1.27) extrapolation for the $p\bar{p}$ cross section ($\sigma_{p\bar{p}}^{stand}$). The errors given should be considered as the upper and lower bounds.

behaviour, (c) the difference of the pp and $p\bar{p}$ total cross sections asymptotically is a constant or rises maximally like $\ln(s/s_{odd})$ and (d) at energies above the ISR allows for a local rise:

$$\sigma_{pp} = \sigma_{pp}^{Regge} + C_4 \ln^2(s/s_0) + \sigma_0 f_{viol}^{odd}(E) \tag{4.7}$$

The violating function f_{viol}^{odd} is chosen such that for energies lower than E_1 it goes to 0; for higher energies up to E_2 or E_4 the function can rise as steeply as we wish.

$$f_{viol}^{odd}(E) = \frac{(E/E_1)^\lambda}{1+(E/E_2)^\lambda} \frac{1+(E/E_3)^\mu}{1+(E/E_4)^\mu} \tag{4.8}$$

μ equals 0 determines the upper limit of the rise; if μ is greater than 0 the cross section starts to fall off for energies greater than E_4 and a lower limit is obtained. E_3 determines the asymptotic limit. Of course $E_1 << E_2$, $E_4 << E_3$, $E_1 << E_4$, $\lambda \geq 0$ and $\mu \geq 0$.

From qualitative arguments it is clear that the constant σ_0 must be positive. A high $\rho_{p\bar{p}}$ value can be obtained if the total cross sections for pp and $p\bar{p}$ cross between ISR and SPS energies [59]. The parameters in the violating function are tuned such that the formula reduces to the Amaldi parametrisation for low energies, and deviates at most 0.5 mb at $\sqrt{s} = 62$ GeV. The same method as in the case of the even hypothesis was used: all kinds of behaviour of the pp cross section were allowed, which yielded $\rho_{p\bar{p}} = 0.24 \pm 0.04$ at $\sqrt{s} = 546$ GeV.
The results - again a shaded area - are shown in figure 4.4 and summarised in table 4.3. One observes a steep rise of the difference of the total cross sections for pp and $p\bar{p}$. The predictive power is limited to energies below 10 TeV.

Of course it is also possible that some mixing of the odd and even scenario occurs - as was already suggested in option (3) of section 4.1: if the $p\bar{p}$ cross section rises more steeply than $\ln^2(s)$, the difference between the pp and the $p\bar{p}$

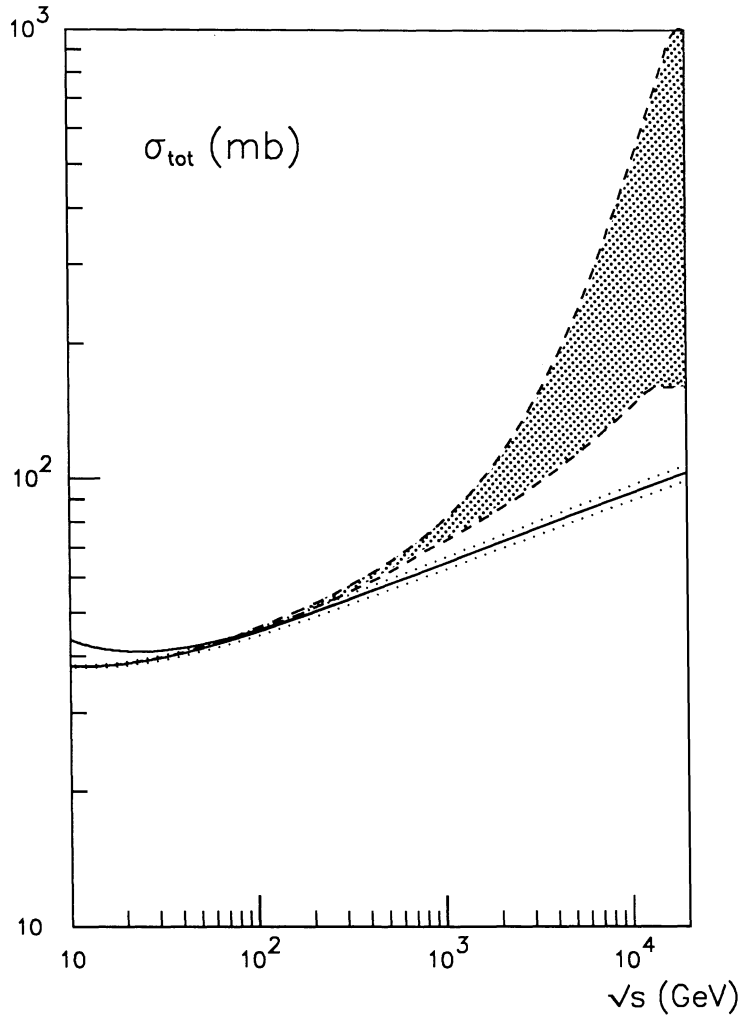

Figure 4.4: The total cross section for pp and $p\overline{p}$ as a function of the energy. The shaded area is obtained by the dispersion relation analysis in the odd scenario and represents the pp total cross section. The continuous curve represents the $\ln^2(s)$ expectation for the $p\overline{p}$ total cross section; the dotted curves show the one-standard-deviations in the constant in front of the $\ln^2(s)$.

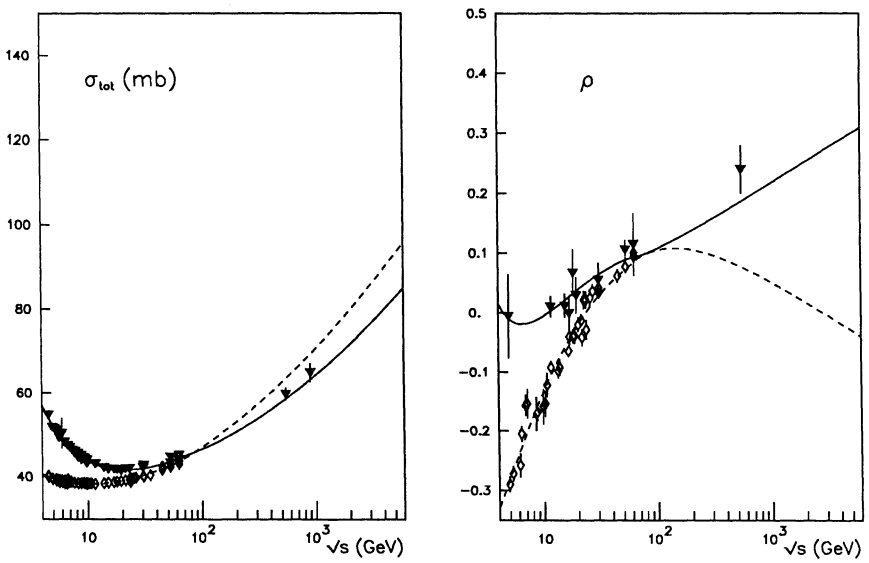

Figure 4.5: The total cross section and the ratio ρ for pp and $p\overline{p}$ as a function of the energy. The triangles represent the $p\overline{p}$ data points [104]. The continuous curves correspond to $p\overline{p}$ scattering, using a parametrisation with a threshold (4.9), the dashed curves correspond to pp scattering.

cross section will become smaller.

As in the case of the first scenario a more specific parametrisation of the so-called threshold type was constructed:

$$\sigma_{\substack{pp \\ p\overline{p}}} = \sigma^{\text{Regge}}_{\substack{pp \\ p\overline{p}}} + C_4 \ln^{\gamma}(s/s_0) \pm C_6\, \theta(s - s_{\text{cuto}}) \ln(s/s_{\text{cuto}}) \pm C_7 \qquad (4.9)$$

A dispersion relation fit (fixing s_0 and leaving free 12 constants) to the data with and without the UA5 point gives within the errors the same result: it yields $C_6 = 0.6 \pm 0.3$ mb and $\sqrt{s_{\text{cut0}}} = 63 \pm 4$ GeV with a $\chi^2/NDF = 162.8/141$. The fit is plotted in figure 4.5.
A continuous parametrisation is more difficult to develop: a simple $\ln(s/s_{\text{odd}})$ does not fit the data, nor does a form like $\ln(1 + s/s_{\text{odd}})$. Bernard et al. [60] however have added an extra Regge term to the low energy term and where thus able to explain the UA4 datum with a maximal odderon of the form $\ln(s/s_{\text{odd}})$.

4.3 Discussion

In conclusion, if the elastic scattering amplitude is an even function at infinite energy, the total cross section must rise locally faster than the assumed $\ln^2(s/s_0)$. The predictions obtained by the dispersion relation analysis (figure 4.1 and table 4.1) are in agreement with the results obtained by analytical methods (see e.g. [56], [60], [61]).

The possible parametrisations of the total cross section are twofold; either there exists a threshold or the total cross section rises continuously. In both cases there is a lot of freedom to construct a parametrisation that satisfies all constraints. Martin [56] has proposed a parametrisation with a threshold by adding a term of the form:

$$\sigma_{\substack{pp \\ p\bar{p}}} = C_{\text{thresh}}\,\theta(s - s_{\text{thresh}})\left(\frac{s - s_{\text{thresh}}}{s}\right)^2 \tag{4.10}$$

to the Amaldi parametrisation of the total cross section. In this way the UA4 ρ measurement could be explained. There is however one problem: the model predicts a total cross section of $\sim$ 76 mb at $\sqrt{s} = 900$ GeV while 65.3 ± 2.2 mb was measured by the UA5 experiment.

Hadjitheodoridis and Kang [61] have taken a more general form of this model:

$$\sigma_{\substack{pp \\ p\bar{p}}} = C_{\text{thresh}}\,\theta(s - s_{\text{thresh}})\left(\frac{s - s_{\text{thresh}}}{s}\right)^{\alpha} \tag{4.11}$$

By allowing all kinds of values for α they were able to fit the UA4 datum and obtain a lower bound for the cross section at 900 GeV of 66.6 mb.

It is shown that the high ρ value can be accounted for if we assume a *continuous* rise of the total cross section with an additional term, which has the form $\ln^2(1 + s/s_1)$ where s_1 lays around 700 GeV. Predictions are given in figure 4.3 and table 4.2.

Recently Troshin and Tyurin [62] have shown that the high ρ value agrees with their 1986 predictions [63]. Their U-matrix model saturates the Froissart-Martin bound in the following way:

$$\sigma_{\substack{pp \\ p\bar{p}}} = \frac{\pi(\hbar c)^2}{m_q c^4}\ln^2(s) \tag{4.12}$$

where m_q is the light quark mass. This model has however the peculiar feature that the ratio of the elastic cross section to the total cross section tends to 1 if infinite energies are approached. The inelastic cross section only rises as ln(s) in the asymptotic regime. This behaviour seems rather unnatural and contrary to the expectations based on QCD (see chapter 5).

Kopeliovich et al. [64] have shown that the high ρ value agrees very well with Lipatov's QCD pomeron that is responsible for a steep rise of the total cross

section. This steep rise is also in agreement with cosmic ray data that were reexamined recently by them.

The second interpretation, which allows for an odd part at infinite energy, assumes that the difference of the pp and $p\bar{p}$ cross sections is not equal to zero. Predictions for this scenario were given in figure 4.4 and table 4.3. It is shown that the pp total cross section crosses the $p\bar{p}$ total cross section around $\sqrt{s}$ ~100 GeV.

A parametrisation with a threshold was presented of the form $\ln(s/s_{\text{cuto}})$, with $\sqrt{s_{\text{cuto}}}$ is approximately 63 GeV.

An odderon, which has this threshold behaviour, is however not very likely. It is more natural that the odderon has a continuous nature as proposed by Bernard et al. [60]. A fit to the data shows that a maximal odderon - i.e. the difference of the total cross sections grows like $\ln(s/s_{\text{odd}})$ - is preferred.

A precise measurement of the total cross section and ρ at the Tevatron ($\Delta\sigma_{p\bar{p}} \leq$ 1 mb) will be able to confirm the results of the ρ measurement by UA4, to distinguish between both scenarios and - perhaps - single out a suitable parametrisation.

It seems a matter of taste to prefer one scenario above the other. There might be good reasons for a cross section that rises like $\ln^2(1 + s/s_1)$. The hypothesis that the steep rise of the total cross section is somehow related to a steeply rising minijet cross section, that was measured by the UA1 experiment [65], is investigated in the next chapter.

Chapter 5

Minijets and the rise of the total cross section

5.1 Hypothesis

Already in the seventies it was suggested that at high energies the rise of the inelastic cross section might be caused by the rise of the total jet cross section [66], [67]. If this is true, it gives a clue to understand the rise of the total cross section.

Recently a lot of work has been done to calculate in the framework of Perturbative Quantum Chromodynamics (PQCD) the differential and total jet cross sections going down to low Q^2 [68]. The predictions of PQCD were confirmed by the measurement of a large steeply rising jet cross section by the UA1 collaboration [65]. These jets at low transverse momentum p_t - experimentally defined as clusters with low transverse energy E_t - were called minijets.

A simple extrapolation from the UA1 data points and a calculation of the jet cross section in PQCD shows that the minijet cross section rises so quickly [69] that it would surpass the inelastic cross section around 1-2 TeV and the total cross section around 2-3 TeV, *if the total and inelastic cross sections are calculated on the basis of the standard parametrisation (1.27), where the total cross section goes asymptotically like* $C_4 ln^2(s/s_0)$. The steep rise of the total jet cross section might indicate that the total and inelastic cross section should rise faster than assumed.

Therefore we will investigate the hypothesis whether the steep rise of the total jet cross section is related to - and perhaps compatible with - a steeply rising inelastic cross section that corresponds to a total cross section of the form (see section 4.2):

$$\sigma_{\substack{pp \\ p\bar{p}}} = \sigma^{\text{Regge}}_{\substack{pp \\ p\bar{p}}} + C_4 \ln^2(s/s_0) + C_5 \ln^2(1 + s/s_1) \tag{5.1}$$

The reasons for this parametrisation are the following. It is clear that the hypothesis of a relation between the steeply rising jet cross section and the inelastic cross section does not require an odderon. This means that we can restrict ourselves to the even scenario. A threshold parametrisation of the total cross

section as e.g. in equations (4.4) and (4.11) seems improbable, as the jet cross section (above $\sqrt{s} \sim 100$ GeV) is a continuous function. Therefore the continuous parametrisation (4.5) (fixing γ at 2) that was proposed in chapter 4 is used. Other parametrisations of this type, that fit the measured ρ value and satisfy asymptotically the Froissart-Martin bound, are - of course - possible too.

The plan of this chapter is the following. First the inelastic cross section - excluding the single diffractive cross section - $\sigma_{\text{inel}}^{\text{nsd}}$, that corresponds to the parametrisation (5.1), is calculated on the basis of a simple hypothesis. Secondly the differential and total jet cross sections are calculated with PQCD and compared to the UA1 results. Further it is investigated when PQCD is expected to break down. Finally the total jet cross section and the inelastic n.s.d. cross section $\sigma_{\text{inel}}^{\text{nsd}}$ are compared.

5.2 The rise of the inelastic cross section

The inelastic cross section that corresponds to formula (5.1) has to be calculated. For this purpose a simple hypothesis is elaborated. The ratio R of the elastic to the total cross section (if a constant forward elastic slope b is assumed) is equal to (see Eq.(1.11)):

$$\mathrm{R} = \frac{\sigma_{\text{el}}}{\sigma_{\text{tot}}} = \frac{\sigma_{\text{tot}}(1+\rho^2)}{16\pi(\hbar c)^2\, b} \tag{5.2}$$

If it is assumed that at infinite energies the black disc limit R = 0.5 is reached, the asymptotic behaviour of the slope can be derived from the asymptotic behaviour of the total cross section. The slope for pp and $\mathrm{p\overline{p}}$ are asymptotically the same (as we restrict ourselves to the even scenario). The slope b can thus be parametrised as (above $\sqrt{s} \sim 50$ GeV):

$$b = \tilde{B}_3 + B_4 \ln^2(s/s_0) + B_5 \ln^2(1 + s/s_1) \tag{5.3}$$

where the total cross section is approximated by (above $\sqrt{s} \sim 50$ GeV):

$$\sigma_{\text{tot}} = \tilde{C}_3 + C_4 \ln^2(s/s_0) + C_5 \ln^2(1 + s/s_1) \tag{5.4}$$

$\tilde{B}_3$ and $\tilde{C}_3$ are approximately constant. It is implicitly assumed that the asymptotic regime sets in immediately. Note that the data for the slope up to $\sqrt{s} = 546$ GeV are also compatible with a $\ln(s)$ behaviour [8], [77]. However, if the total cross section rises as steeply as assumed, and the slope only goes like $\ln(s)$, unitarity ($\mathrm{R} \leq 1.0$) will be violated around $\sqrt{s} \sim 4$ TeV.

Because the ρ value goes to zero, when infinite energies are approached, the constants C_4 and B_4 and, C_5 and B_5 are related by:

$$\begin{aligned} C_4 &= 8\pi(\hbar c)^2\, B_4 \\ C_5 &= 8\pi(\hbar c)^2\, B_5 \end{aligned} \tag{5.5}$$

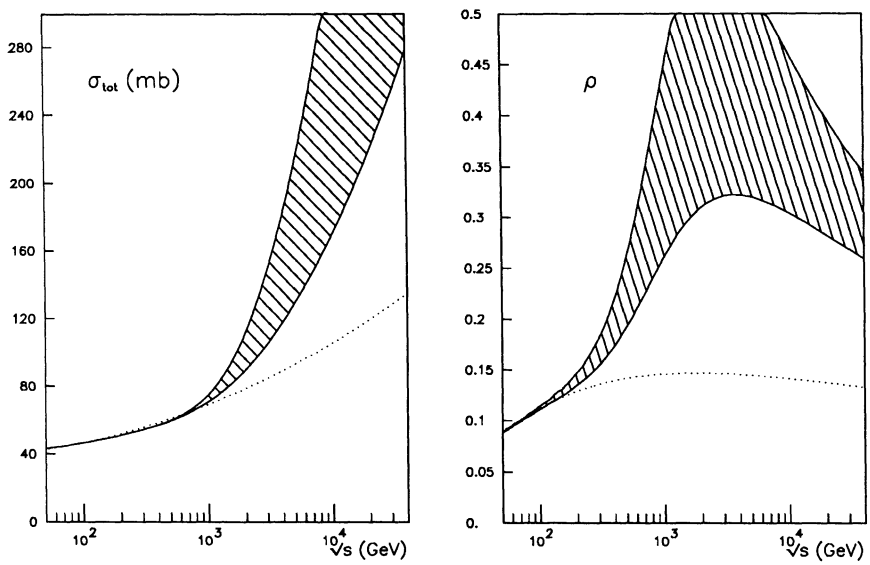

Figure 5.1: Total cross section and rho as a function of the energy. The shaded area gives the predictions according to equation (5.4) and (5.6). The dotted curve is obtained by an Amaldi-like model ($C_5 = 0$).

It is possible to calculate with the dispersion relations the real part that corresponds to formula (5.4). The result is:

$$\rho\sigma_{\text{tot}} = \pi C_4 \ln(s/s_0) + \pi C_5 \left(\ln(1 + s/s_1) + \mathcal{F}(s/s_1)\right) \tag{5.6}$$

The function $\mathcal{F}$ can be calculated analytically (see Appendix A). For high energies $\mathcal{F}$ goes to zero.

An upper limit for the constant C_5 can be derived. It was required that the ratio R of the elastic and total cross section is at maximum 0.5. The upper limit for C_5 is obtained by substituting the formulas (5.6) for ρ, (5.4) for σ_{tot} and (5.3) for b in equation (5.2), fixing R at 0.5. This gives approximately (neglecting $\mathcal{F}$):

$$C_5 \preceq \frac{8\pi(\hbar c)^2 \tilde{B}_3 - \tilde{C}_3}{\pi^2} \tag{5.7}$$

The free constants $\tilde{C}_3$, C_4, s_0 and $\tilde{B}_3$ are determined by a fit through the available data up to 546 GeV. After substitution an upper limit for C_5 of ~8.5 mb is obtained.

In figure 5.1 the results for the total cross section and the ratio ρ are shown. Two extreme cases are plotted. The upper bound corresponds to the upper limit for $C_5 = 8.5$ mb and a value for ρ of 0.28 (one standard deviation above the measured $\rho_{\text{p}\overline{\text{p}}}$ (546 GeV) value). The lower bound corresponds to the lowest value

$\sqrt{s}$	σ_{tot}	ρ	b	σ_{el}	σ_{inel}	R
TeV	mb		GeV^{-2}	mb	mb	
0.2	51.0	0.13	14.2	9.9	41.4	0.19
0.546	60.7	0.24 $\pm$0.04	15.2	13.1	47.6	0.21
0.9	70. $\pm$1.5	0.33 $\pm$0.08	16.1 $\pm$0.2	17.3$\pm$1.4	52.7 $\pm$0.1	0.25$\pm$0.02
1.6	90. $\pm$7.	0.42 $\pm$0.12	18.2 $\pm$0.7	27.3 $\pm$5.5	62.5 $\pm$1.6	0.30$\pm$0.04
2.0	101. $\pm$11.	0.44 $\pm$0.13	19.3 $\pm$1.1	33.2 $\pm$8.3	67.9 $\pm$2.9	0.32$\pm$0.05
4.0	150. $\pm$32.	0.44 $\pm$0.12	24.9 $\pm$3.3	58.9 $\pm$21.	91.6 $\pm$11.	0.38$\pm$0.06
10.0	249. $\pm$79.	0.38 $\pm$0.08	34.5 $\pm$8.1	109. $\pm$48.	140. $\pm$31.	0.42$\pm$0.06
40.0	472. $\pm$193.	0.30 $\pm$0.04	57.2 $\pm$20.	221. $\pm$108.	251. $\pm$86.	0.45$\pm$0.04

Table 5.1: Predictions for the total cross section, ρ, the slope, the elastic cross section, the inelastic cross section and the ratio R for our hypothesis. With $\tilde{B}_3 = 13.1$ GeV^{-2}, $\tilde{C}_3 = 39.6$ mb and $C_4 = 0.280$ mb, $s_0 = 68.5$ GeV^2 and for the lower bound $C_5 = 2.0$ mb and $\sqrt{s_1} = 500$ GeV (- sign), for the upper bound $C_5 = 8.5$ mb and $\sqrt{s_1} = 730$ GeV (+ sign). To obtain the total error on the predictions, the errors on the constants should be taken into account.

$\sqrt{s}$	σ_{tot}	ρ	b	σ_{el}	σ_{inel}	R
TeV	mb		GeV^{-2}	mb	mb	
0.2	51.9	0.129	14.2	9.9	42.0	0.19
0.546	61.9	0.143	15.2	13.1	48.7	0.21
0.9	67.8	0.146	15.8	15.2	52.6	0.22
1.6	75.5	0.147	16.6	17.9	57.6	0.23
2.0	78.7	0.147	16.9	19.1	59.6	0.24
4.0	89.5	0.145	18.0	23.2	66.3	0.26
10.0	105.8	0.141	19.7	29.6	76.2	0.28
40.0	134.8	0.132	22.7	41.7	93.1	0.31

Table 5.2: Predictions are given for a standard Amaldi-like model ($C_5 = 0$) with $\tilde{B}_3 = 12.8$ GeV^{-2}, $\tilde{C}_3 = 38.4$ mb, $C_4 = 0.330$ mb and $s_0 = 68.5$ GeV^2, where $\rho_{\text{p}\overline{\text{p}}}$ (546 GeV) equals 0.14.

of $C_5 = 2.0$ and a value for $\rho_{\text{p}\overline{\text{p}}}$ (546 GeV) of 0.20. Thus a shaded area is obtained. In figure 5.2 the corresponding slope, the ratio R, the elastic cross section, and the inelastic cross section are plotted as a function of the energy. The results are summarised in table 5.1. They should be compared with the predictions of an Amaldi-like model (see table 5.2 and the dotted curves in figures 5.1 and 5.2).

The slope parameter b was measured recently at the Tevatron and a value of 17.2 ± 1.3 GeV^{-2} [78] at $\sqrt{s} = 1800$ GeV was found. This result is compatible with our hypothesis that predicts a slope of 18.7 ± 0.9 GeV^{-2}. It is also compatible with the predictions of an Amaldi-like model. More precise measurements of the

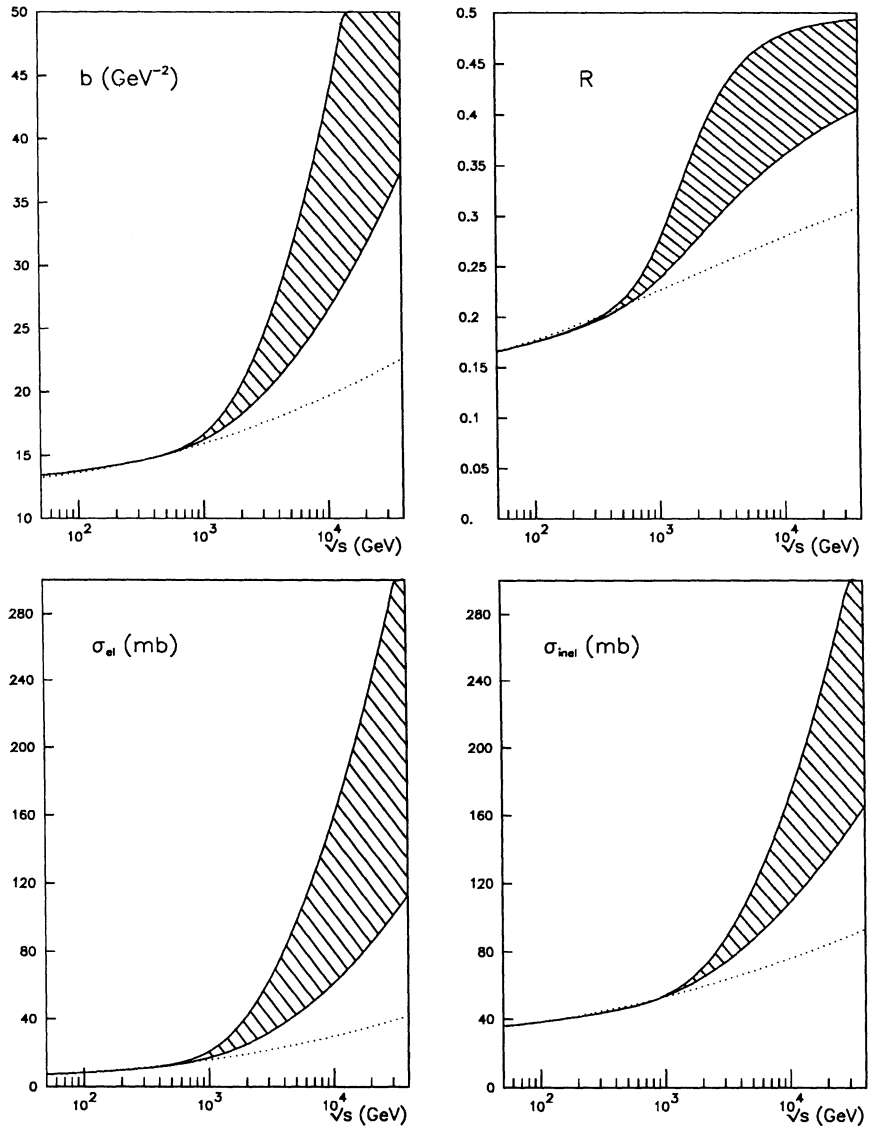

Figure 5.2: The slope, the ratio R, the elastic cross section and the inelastic cross section as a function of the energy. The shaded area gives the expectation for our hypothesis. The dotted curve is obtained by an Amaldi-like model.

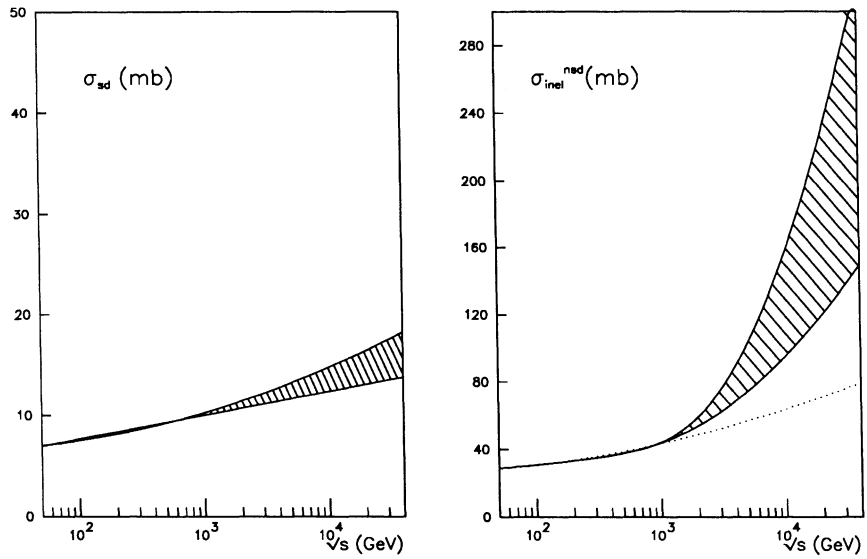

Figure 5.3: The single diffractive and the inelastic n.s.d. cross sections as a function of the energy. The dotted curve is obtained by an Amaldi-like model.

slope b, the total cross section and the ratio ρ at the Tevatron are needed to distinguish both hypotheses.

In order to calculate the inelastic n.s.d. cross section (that can be compared with the total jet cross section) the single diffractive cross section σ_{sd} has to be known. Different parametrisations for the single diffractive cross section can be considered, assuming e.g. a slowly like $\ln(s)$ rising cross section or one which rises like $\ln^2(s)$. Both parametrisations were considered and define the contours of the shaded area plotted in figure 5.3a. The inelastic n.s.d. cross section is calculated by subtracting the single diffractive cross section from the inelastic cross section. The result is shown in figure 5.3b.

5.3 Calculation of the jet cross section

The differential jet cross section will be calculated in the framework of the QCD parton model using perturbation theory. This calculation has been performed by many authors. Here the first order expression of EHLQ [79] for the two jet final state will be used:

$$\frac{d\sigma_{\rm jet}}{d\eta_1 d\eta_2 dp_t} = \frac{2\pi\tau p_t}{\hat{s}} \sum_{ij} \frac{\mathcal{G}_i^a(x_a, M^2)\, \mathcal{G}_j^b(x_b, M^2)\, \hat{\sigma}_{ij}(\hat{s}, \hat{t}, \hat{u})}{1+\delta_{ij}} + \frac{\mathcal{G}_j^a(x_a, M^2)\, \mathcal{G}_i^b(x_b, M^2)\, \hat{\sigma}_{ij}(\hat{s}, \hat{u}, \hat{t})}{1+\delta_{ij}} \tag{5.8}$$

where η_1 , η_2 are the respective rapidities of the jets, p_t is the common transverse momentum, M the characteristic mass of the jet, $\mathcal{G}$ is the parton distribution function, with:

$$\hat{s} = s\,\tau \tag{5.9}$$

$$\tau = \frac{4p_t^2}{s} \cosh^2\left(\frac{\eta_1 - \eta_2}{2}\right) \tag{5.10}$$

$$x_a = \sqrt{\tau} e^{\frac{\eta_1+\eta_2}{2}} \tag{5.11}$$

$$x_b = \sqrt{\tau} e^{-\frac{\eta_1+\eta_2}{2}} \tag{5.12}$$

$$\cos\theta = \sqrt{1 - \frac{4p_t^2}{\hat{s}}} \tag{5.13}$$

$$\hat{t} = -\frac{\hat{s}}{2}(1 - \cos\theta) \tag{5.14}$$

$$\hat{u} = -\frac{\hat{s}}{2}(1 + \cos\theta) \tag{5.15}$$

The summation runs over seven first order processes and the corresponding elementary cross sections $\hat{\sigma}_{ij}$ for quarks and gluons (see e.g. [79]).

Here we restrict ourselves to jets at 'low' p_t values - lower than approximately 40 GeV/c. Low p_t jets give the main contribution to the total jet cross section. In that case the differential cross section is dominated by the process $gg \to gg$ (gluon-gluon goes to gluon-gluon) [72], [74], citeEic84. The elementary cross section for this process is [79]:

$$\hat{\sigma}(gg \to gg) = \frac{9\alpha_s^2(Q^2)}{2\hat{s}} \left[3 - \frac{\hat{t}\hat{u}}{\hat{s}^2} - \frac{\hat{s}\hat{u}}{\hat{t}^2} - \frac{\hat{s}\hat{t}}{\hat{u}^2}\right] \tag{5.16}$$

where Q^2 - the momentum transfer squared - is in this case not exactly defined because of higher order corrections. For $\mathcal{G}$ the gluon structure function should be taken. Additional assumptions should be made to extract the differential jet cross section and a total jet cross section from formula (5.8).

First the scale for Q^2 and M^2 should be fixed. In first order calculations this choice is rather arbitrary: one can chose e.g. $Q^2 = M^2 = 4p_t^2$, $2\,p_t^2$, p_t^2, $p_t^2/2$, or $p_t^2/4$. Higher order effects should be taken into account by using an overall normalisation or K factor, which lies between 1. and 2.

Secondly the gluon structure function is not known with absolute precision in the low x domain. Therefore different gluon structure functions were considered:

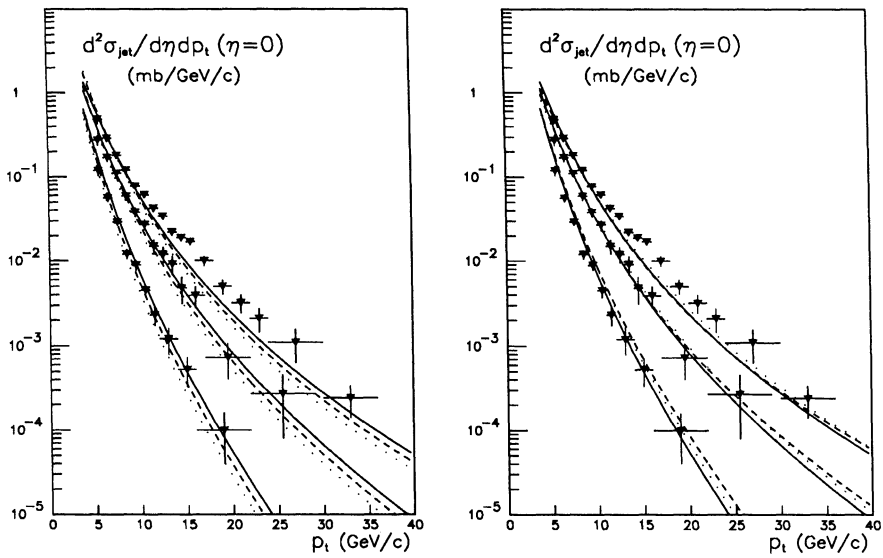

Figure 5.4: Differential jet cross section at $\eta = 0$ as a function of p_t for the three energies $\sqrt{s}$ = 200, 500 and 900 GeV (respectively the lower, middle and upper set of data points)
a. with EHLQ set 1 and $K = 1.25$. The solid line corresponds to $Q^2 = p_t^2/2$, the dashed line to $Q^2 = p_t^2$ and the dotted line to $Q^2 = 2\,p_t^2$.
b. with $Q^2 = p_t^2/2$. The solid line corresponds to EHLQ set 1 with $K = 1.25$, the dashed line to D&O set 1 with $K = 1.75$ and the dotted line to GHR set 1 with $K = 1.25$. The data from UA1 are plotted too [65].

set 1 and 2 of EHLQ [79], set 1 and 2 of Duke and Owens (D&O) [80], and set 1 of Glück, Hoffmann and Reya (GHR) [81].

The differential jet cross section around η equals zero is calculated in the measured rapidity range $|\eta| < 1.5$ and compared to the measured jet spectra of UA1. Therefore equation (5.8) is integrated over the rapidity range. First the choice of Q^2 is examined. This was done for the distributions of EHLQ set 1 for three choices of Q^2 ($Q^2 = 2p_t^2$, p_t^2, $p_t^2/2$), fixing one overall K-factor at 1.25, for the different energies $\sqrt{s}$ =200 GeV, 500 GeV and 900 GeV. The result is plotted in figure 5.4a and should be compared with the data points of UA1 [65]. The choice of Q^2 changes a little bit the slope of the p_t distribution: it becomes steeper if we go to $Q^2 = 2\,p_t^2$. The best choice is $Q^2 = p_t^2/2$.

Secondly the effect of different structure functions is studied. Therefore Q^2 is fixed at $p_t^2/2$ and the differential cross section at $\eta = 0$ is calculated for the three sets (EHLQ set 1, D&O set 1 and and GHR set 1) The result is also plotted in figure 5.4b.

All sets of structure functions describe very well the form of the data. The K-

factor has to be readjusted a little bit: for the sets of EHLQ and GHR K is equal to 1.25, for the set of D&O K is equal to 1.75. The introduction of a K factor is not really a problem. Higher order corrections cause an overall (theoretical) uncertainty of a factor of 1-2. The experimental uncertainty in the determination of p_t has the effect of an overall normalisation error of at least 20 percent [65].

These results show that PQCD can explain the differential jet cross sections that were measured by UA1. Similar conclusions were reached by other authors [65],[74]. This gives confidence that from PQCD reliable predictions for the jet cross section around 1 TeV can be obtained.

The reliability of first order PQCD in the low p_t region should be examined before the total jet cross section is evaluated. In principle the total jet cross section could be calculated by integrating formula (5.8) over p_t and η. It is not possible to start the integration at p_t equals zero, because the differential cross section is singular at this point. This is a well known phenomenon in PQCD. Perturbation theory breaks down at low p_t (or Q^2) of the order of 1 GeV/c. The problem in the low p_t regime is that no one has succeeded yet to obtain reliable results based on (non perturbative) QCD.

This means that if low p_t values are reached the perturbative, calculable domain is left and the non perturbative regime is entered. We restrict ourselves to first order PQCD. Between the first order perturbative and the non perturbative regime exists a transition region, where higher order effects become important, and the partons start to screen and overcrowd each other. Part of this region can be calculated by higher order PQCD.

The breakdown of PQCD at low p_t can be associated with a physical process: the emergence of more than two jets in the final state because of multiple parton scattering [73]. The main contribution to the total jet cross section comes however from two jets in the final state as given by equation (5.8). The four jet total cross section for double parton scattering is e.g at most 12.5 percent of the two jet cross section [72]. We will neglect these effects.

It is important to investigate down to which value of p_t first order PQCD can be trusted. In the paper of Gribov et al. [82] an intuitive criterion for the breakdown of PQCD is proposed. If the parton packing fraction (W) is much less than one, perturbative QCD can be trusted. This fraction is defined by:

$$W(x,Q^2) = W_1\, x\mathcal{G}(x,Q^2)\, m_\pi^2/Q^2 \tag{5.17}$$

where W_1 is a constant which is approximately 1, and m_π is the mass of the pion. Another criterion is suggested in a paper of Collins [83]. If it is assumed that the number of jets per unit of rapidity squared may not surpass a certain value - in order not to violate the Froissart bound (which goes like the rapidity squared) - the following criterion is obtained:

$$\overline{W}(x,Q^2) = W_2\, [x\mathcal{G}(x,Q^2)]^2\, m_\pi^2/Q^2 \tag{5.18}$$

where W_2 is a constant which is approximately 1.

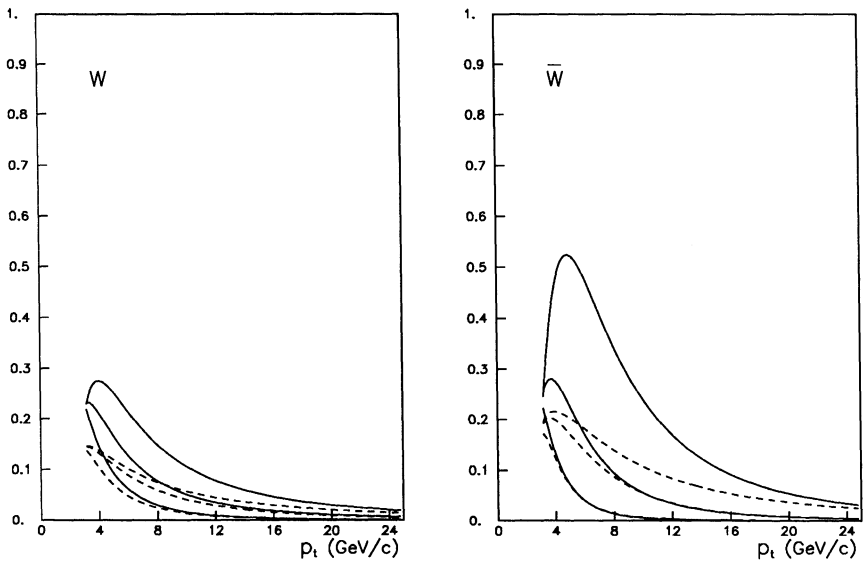

Figure 5.5: Packing fraction W and $\overline{W}$ for set 1 of EHLQ (continuous curve) and set 1 of GHR (dashed curve) as a function of p_t, for the energies $\sqrt{s}$ = 200 GeV , 2 TeV and 20 TeV (respectively lower, middle and upper curve).

To get an impression of these criteria W and $\overline{W}$ were plotted for three energies ($\sqrt{s}$ = 200 GeV, 2 TeV and 20 TeV) as a function of p_t for set 1 of EHLQ and set 1 of GHR in figure 5.5. A first look shows that the packing fraction W and $\overline{W}$ blows up if low values for p_t are reached and becomes large if higher energies are approached. A careful examination shows that the packing fraction goes through a maximum for high energies. This maximum shifts from $p_t \sim 4$ (3.5) GeV/c at $\sqrt{s}$ = 2 TeV to ~ 5 (4.5) GeV/c at 20 TeV for the structure functions of EHLQ set 1 (and GHR set 1). This behaviour can be used as an indication that first order PQCD breaks down (for these structure functions) below this value of p_t. Thus there is a rough indication that PQCD can be trusted down to a value of p_t of 3.5 - 5 GeV/c.

This statement can be verified by the measurement of the differential and total jet cross section by the UA1 collaboration. The differential jet cross section is measured down to 4-5 GeV/c (for experimental reasons) and is in good agreement with the prediction of PQCD. The minimum p_{tmin} can be calculated more precisely from the measurement of the total minijet cross section. A value of 13.0 mb at $\sqrt{s}$ = 630 GeV is measured by UA1. By adjusting p_{tmin} to this measured jet cross section a value for p_{tmin} of 4.5 $\pm$ 0.1 GeV/c was found.

The raw jet cross section as a function of the energy is calculated by integrating equation (5.8), while the value of p_{tmin} was kept fixed at 4.5 GeV/c. The result is shown in figure 5.6. The form of the curve is in good agreement with the data

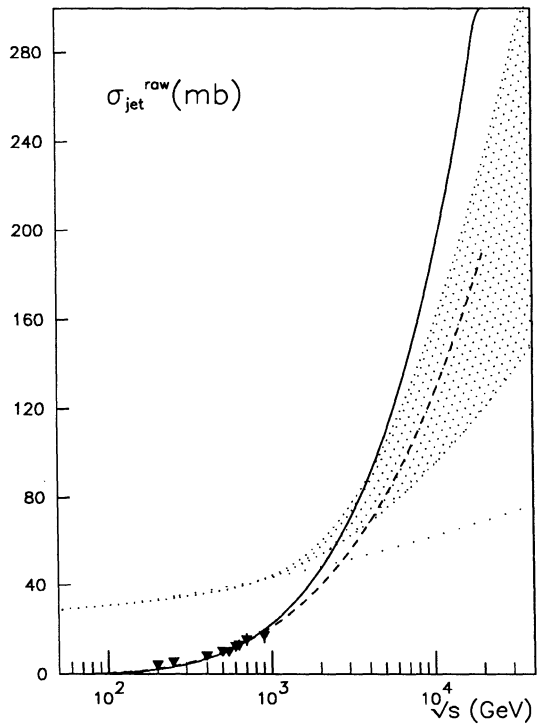

Figure 5.6: Raw jet cross section for set 1 of EHLQ (continuous curve) and set 1 of GHR (dashed curve). The inelastic n.s.d. cross section for our hypothesis (shaded area) and an Amaldi like model (dotted curve). The UA1 data points are plotted too.

up to $\sqrt{s} = 900$ GeV. The upper case (obtained with the set 1 of EHLQ) is the fastest rising jet cross section that could be obtained with the different structure functions of EHLQ, D&O and GHR. The lower case (obtained with set 1 of GHR) corresponds to the slowest rising jet cross section. The result is a steeply rising raw jet cross section in the energy domain above $\sim$ 1 TeV. The trend for this steep rise is already present in the UA1 data.

One might question whether it is allowed to keep the minimum value for $p_{t\min}$ fixed at 4.5 GeV/c. A careful examination of the packing fraction shows that for GHR set 1 there is no problem up to $\sqrt{s} \sim 10$ TeV. For set 1 of EHLQ one might argue that above approximately 3 TeV $p_{t\min}$ should be raised slowly to $\sim$5 GeV/c at 10 TeV. This means that in any case up to approximately 3 TeV the predictions obtained with EHLQ set 1 for the raw jet cross section are reliable.

Some authors (e.g. [75], [76]) doubt the conclusion that the jet cross section will rise very steeply and try to lower it drastically by introducing an absorption or cancellation mechanism. The motivation for this procedure is mainly that the

total jet cross section cannot surpass the inelastic n.s.d. cross section as calculated on the basis of an Amaldi-like model. If the hypothesis of an Amaldi-like model is dropped - as is done here - there is no reason left for introducing such a mechanism.

5.4 Comparison and Conclusions

If we compare the raw jet cross section and the inelastic n.s.d. cross section, we get the impression that the form of the curves is almost the same. This suggests that the following formula holds:

$$\sigma_{\text{inel}} = \sigma_{\text{sd}} + \sigma_{\text{jet}}^{\text{tot}} + \sigma_0 \tag{5.19}$$

where σ_0 is the remaining inelastic cross section. It can be argued quite generally that this term should be positive and not equal to zero at infinite energies. An interesting assumption - that was already proposed in the seventies [66], [67] - is that σ_0 is a constant. This means that the rise of the inelastic cross section is driven by the the total jet cross section.

This hypothesis can be tested by fitting the UA1 data. Therefore a renormalisation factor λ is introduced, that reflects the systematic uncertainty in the UA1 minijet cross sections. By comparing the measured cross sections with the calculated inelastic n.s.d. cross sections up to 900 GeV (that are barely different for an Amaldi-like model - see figure 5.3 and tables 5.1 and 5.2) a value for λ of 0.75 ± 0.05 and σ_0 of 30.5 ± 0.5 mb was found. This is in agreement with the overall systematic error of 20 percent that is quoted by UA1 [65].

It is possible to calculate - on the basis of this hypothesis - the total jet cross section. Therefore we require that the low energy behaviour of the total jet cross section fits the renormalised UA1 data. This means that the minimum p_{tmin} has to be raised to 5 GeV/c. The result of this calculation is plotted in figure 5.7. It is clear that the rise of the total jet cross section and the inelastic n.s.d. cross section follow the same trend. Only above 10 TeV one has to raise the value of p_{tmin} and higher order corrections become important. This means that up to approximately 10 TeV formula (5.19) holds.

In conclusion, it is argued that the rise of the total jet cross section as a function of the energy is compatible with a steeply rising inelastic cross section. The jet cross section was calculated in PQCD and fitted perfectly the renormalised UA1 data points. In more detail it is shown that the inelastic n.s.d. cross section - that is calculated on the basis of the hypothesis of a total cross section that rises like $\ln^2(1+s/s_1)$ - can be expressed in a constant cross section plus a steeply rising jet cross section from $\sqrt{s}$ equals 100 GeV up to approximately 10 TeV. This means that the rise of the inelastic cross section is driven by the jet cross section.

A steeply rising jet cross section is - even if we allow for a p_{tmin} that rises slowly with the energy - a direct implication of PQCD. The UA1 measurement of the

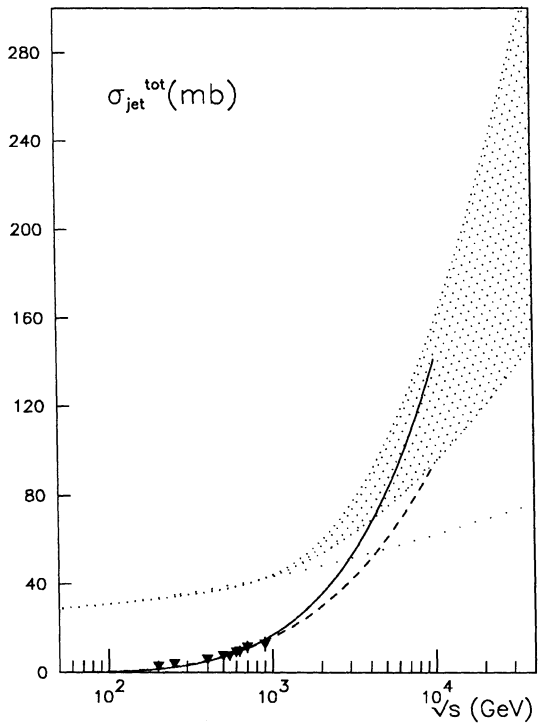

Figure 5.7: Total jet cross section for set 1 of EHLQ (continuous curve) and set 1 of GHR (dashed curve). The inelastic n.s.d. cross section for our hypothesis (shaded area) and an Amaldi like model (dotted curve). The renormalised UA1 data points are plotted too.

minijet cross section confirms this prediction. A high energy extrapolation from the data points yields a steeply rising jet cross section in the TeV domain.

The total jet cross section surpasses the predictions of an Amaldi-like model for the inelastic n.s.d. cross section. This indicates that the inelastic cross section and the total cross section for pp and $p\overline{p}$ will rise steeper than an Amaldi-like model predicts. A steeply rising total cross section for pp and $p\overline{p}$ (which is parametrised e.g. as equation (5.1)) is - on the other hand - one of the possible implications of the high ρ value that was measured by the UA4 experiment.

Appendix A

It is in principle straight forward to calculate ρ from the imaginary part using a dispersion relation [56]:

$$\frac{ReF(s)}{s} = \rho(s)\,\sigma(s) = \frac{2s}{\pi}\oint_{4m^2}^{\infty} ds'\,\frac{\sigma(s')}{s'^2 - s^2} \tag{5.20}$$

The real part which corresponds to a total cross section of the form $C_4\,\ln^2(s/s_0)$ equals:

$$\frac{ReF(s)}{s} = \rho(s)\,\sigma(s) = \pi C_4\,\ln(s/s_0) \tag{5.21}$$

Thus the main contribution of the real part which corresponds to a total cross section which has the form $C_5\,\ln^2(1+s/s_1)$ can be written as:

$$\frac{ReF(s)}{s} = \rho(s)\,\sigma(s) = \pi C_5\,(\ln(1+s/s_1) + \mathcal{F}(s/s_1)) \tag{5.22}$$

by substituting this formula in formula (5.20) one gets an expression without a pole:

$$\begin{aligned}\pi^2\mathcal{F}(s/s_1) \;=\; & \int_{1+4m^2/s_1}^{4m^2/s_1} ds'\,\frac{\ln^2(s')}{s'-1-s/s_1} + \int_{4m^2/s_1}^{\infty} ds'\,\frac{\ln^2(s')}{s'+1+s/s_1} \\ & - \int_{1+4m^2/s_1}^{\infty} ds'\,\frac{\ln^2(s')}{s'-1+s/s_1}\end{aligned} \tag{5.23}$$

An integral has to be solved of the form:

$$\int ds'\,\frac{\ln^2(s')}{s'+a} \tag{5.24}$$

where a is constant. The integration interval doesn't contain the pole at $s' = -a$. With some algebra one can prove that:

$$\int ds'\,\frac{\ln^2(s')}{s'+a} = \ln^2(s)\,\ln|\frac{s+a}{a}| + 2\,\ln(s)\,L_2(-s/a) - 2\,L_3(-s/a) + C \tag{5.25}$$

where L_2 and L_3 are the dilog and trilog functions. It is then straight forward to calculate the real part by the substitution of the proper boundaries and values for a.

Conclusions

The measurement of ρ, i.e. the ratio of the real to the imaginary part of the nuclear part of the scattering amplitude at the momentum transfer squared zero ($|t| = 0$), for $p\bar{p}$ at a centre of mass energy of $\sqrt{s} = 546$ GeV yielded the final result:

$$\rho_{p\bar{p}}\ (546\ \text{GeV}) = 0.24 \pm 0.04$$

(statistical and systematical error added quadratically). The result was checked against different parametrisations of the nuclear scattering amplitude - allowing for e.g. a spin-flip term and a t dependence of the slope - and remains the same within the quoted error.

This means that the value of the total cross section, which was published before [8], [9] assuming a ρ value of 0.15, has to be changed into $\sigma_{p\bar{p}}$ (546 GeV) = 60 $\pm$ 1.5 mb. The result for ρ is almost three standard deviations higher than the standard expectation for the value of $\rho_{p\bar{p}}$ (546 GeV) that yielded 0.12-0.14.

The implications of the high $\rho_{p\bar{p}}$ value were derived using a dispersion relation analysis. The interpretation is twofold.

(1) Assuming that the pp and $p\bar{p}$ cross sections are asymptotically identical - the even scenario - it is deduced that the total cross section rises steeply in the 1-4 TeV domain.

(2) In case the pp and $p\bar{p}$ cross sections are asymptotically different - the odd scenario - it is deduced that the total cross sections for pp and $p\bar{p}$ cross around $\sqrt{s} \sim 100$ GeV followed by a rise of the difference of the pp and $p\bar{p}$ total cross sections up to approximately 10 TeV.

Predictions for the total cross section for pp and $p\bar{p}$ in the even and odd scenario are given in chapter 4. It is shown that in both cases this rise can be accounted for if we add an additional term with an energy cut-off to the usual Amaldi parametrisation (1.27) of the the total cross section: $C_5 \ln^2(s/s_{\text{cut}})$ in the even scenario , or $\pm C_6 \ln(s/s_{\text{cuto}})$ in the odd scenario, where $\sqrt{s_{\text{cut}}}$ lies around 500 GeV and $\sqrt{s_{\text{cuto}}}$ around 63 GeV. Both quantities can be interpreted as a threshold of a new process. For the even scenario, a continuous parametrisation without a threshold is also proposed with an extra term of the form $C_5 \ln^2(1 + s/s_1)$, where $\sqrt{s_1}$ equals 700 GeV.

Finally it is shown that the steeply rising cross section - that was derived in the even scenario - might be compatible with the rise of the total jet cross section

as it can be calculated in perturbative QCD. The total cross section for pp and $p\overline{p}$ is assumed to be described by the Amaldi parametrisation plus the extra term of the form $C_5 \ln^2(1 + s/s_1)$. A simple hypothesis for the calculation of the inelastic n.s.d. cross section is elaborated and an upper limit for C_5 of 8.5 mb is derived. It is shown that this implies that the ratio ρ, the forward elastic slope (b), the ratio of the elastic to the total cross section (R), and the elastic and inelastic cross sections ($\sigma_{\rm el}$ and $\sigma_{\rm inel}$) must rise steeply as a function of the energy. Predictions for these quantities are given in chapter 5.

It is argued that from perturbative QCD one should expect a steep rise of the total jet cross section, compatible with the UA1 minijet data. It is shown quantitatively that the steep rise of $\sigma_{\rm inel}^{\rm nsd}$ - derived from our hypothesis - is compatible with the rise of the total jet cross section up to $\sqrt{s} \sim 10$ TeV. If it is assumed that $\sigma_{\rm inel}(s) = \sigma_{\rm sd}(s) + \sigma_{\rm jet}^{\rm tot}(s) + \sigma_0$, where σ_0 is a constant, a perfect agreement between QCD predictions and our calculation of the inelastic n.s.d. cross section is obtained. This means that the rise of the inelastic cross section is driven by the jet cross section. The rise of the inelastic n.s.d. cross section and the jet cross section is compatible with a steeply rising total cross section above $\sqrt{s} = 546$ GeV and a high $\rho_{\rm p\overline{p}}$ value at the Collider.

References

[1] UA4 Collaboration, D. Bernard et al., Phys. Lett. 198B (1987) 583.

[2] P. Kluit and J. Timmermans, Phys. Lett. 202B (1988) 459.

[3] M. Botje, PhD thesis, University of Utrecht 1984.

[4] N. Amos et al., Nucl. Phys. B262 (1985) 689.

[5] H. Bethe, Ann. Phys. 3 (1958) 190.

[6] G. West and D. Yennie, Phys. Rev. 172 (1968) 1413.

[7] R. Cahn, Zeitschr. für Phys. C 15 (1982) 253.

[8] UA4 Collaboration, M. Bozzo et. al., Phys. Lett.147B (1984) 385.

[9] R. van Swol, PhD thesis, University of Amsterdam 1985.

[10] P. Collins, *An introduction to Regge theory and high energy physics*, Cambridge 1977.

[11] Y. Pomeranchuk, JETP 7 (1958) 499.

[12] M. Froissart, Phys. Rev. 123 (1961) 1053.

[13] A. Martin, Nuov. Cim. 42 (1966) 930.

[14] G. Grundberg and T. Truong, Phys. Rev. D 9 (1974) 2874.

[15] H. Cornille and A. Martin, Phys. Lett. 40B (1972) 671.

[16] see references [17], [18], [19], [20], [21].

[17] A. Martin, Proc. of the Workshop on $p\overline{p}$ Physics, Bern (1984), CERN 84-09, p.308.

[18] M. Block and R. Cahn, Phys. Lett. 188B (1987) 143.

[19] R. J. Glauber and J. Velasco, Phys. Lett. 147B (1984) 380.

[20] R. Henzi and P. Valin, Phys. Lett. 149B (1984) 239.

[21] C. Bourrely, J. Soffer and T.T. Wu, Phys. Lett. B196 (1987) 237, plus errata B198 (1987) 591.

[22] P. Gauron, E. Leader, B. Nicolescu, Phys. Rev. Lett. 54 (1985) 2656, 55 (1985) 639.

[23] N. Khuri, T. Kinoshita, Phys. Rev. B 137 (1965) 720.

[24] U. Amaldi et al., Phys. Lett. 44B (1973) 112.

[25] A. Martin, Zeitschr. für Phys. C 15 (1982) 185.

[26] P. Söding, Phys. Lett. 8 (1964) 285.

[27] W. Bartels and A. Diddens, CERN NP internal report (1973) 73-4.

[28] J. Dorenbosch, PhD thesis, University of Amsterdam 1977.

[29] U. Amaldi et al., Phys. Lett. 66B (1977) 390.

[30] see e.g. references [17], [18], [19], [20], [21], [31].

[31] P. Gauron, E. Leader, B. Nicolescu, Nucl. Phys. B 299 (1988) 641.

[32] C. Rubbia, P. McIntyre and D. Cline, Proc. Int. Neutrino Conf. Aachen 1976, p.683.

[33] see e.g. references [34], [35], [36].

[34] S. van der Meer, CERN-ISR-PO internal Report 72-31 (1972).

[35] P. Bramham, Nucl. Instr. Meth. 125 (1975) 201.

[36] D. Möhl et al., Phys. Report 58 (1980) 73.

[37] R. Billinge and M. Crowley-Milling, IEE Trans. on Nucl. Sc. NS-26 (1979).

[38] J. Gareyte, 11^{th} Int. Conf. on High Energy Accelerators Geneva 1980, p.79.

[39] H. Hoffman, CERN EP/81-139 (1981).

[40] UA1 Collaboration, "A 4π Solid Angle Detector for the SPS Used as a Proton-Antiproton Collider at the Centre-of-Mass Energy of 540 GeV", CERN-SPSC/78-06/P 92 (1978).

[41] UA2 Collaboration, "Proposal to Study Antiproton-Proton Interactions at 540 GeV c.m. Energy", CERN-SPSC/78-08/P 93 (1978), plus addendum CERN-SPSC/78-54/P 93-Add.1 (1978).

[42] UA4 Collaboration, "The Measurement of Elastic Scattering and of the Total Cross-Section at the CERN $p\bar{p}$ Collider", CERN-SPSC/78-105/P 114 (1978).

[43] UA5 Collaboration, "An Investigation of Proton-Antiproton Events at 540 GeV c.m. Energy with a Streamer Chamber Detection System", CERN-SPSC/78-70/P 108 (1978).

[44] E.D. Courant and H.S. Snyder, Ann. Phys. 3, (1958) 1.

[45] E.J. Wilson, CERN 77-07 (1977).

[46] P.J. Bryant, CERN 84-04 (1984).

[47] M. Sands, SLAC-121 (1970) 263.

[48] P.E. Faugeras, CERN SPS/84-7 (ARF) (1984).

[49] J. Buskens et al., Nucl. Instr. Meth. 207 (1983) 365.

[50] UA4 Collaboration, M. Bozzo et al., Nucl. Instr. Meth. A238 (1985) 35.

[51] U. Amaldi et al., Phys. Lett. 43B (1973) 231.

[52] J. Bosser et al., CERN SPS/84-11 (DI-MST) (1984).

[53] D. Bernard, PhD thesis, University of Paris-Sud 1987.

[54] C. Bourrely, J. Soffer and D. Wray, Nucl. Phys. B 77 (1974) 386.

[55] UA5 Collaboration, G.J. Alner et al., Zeitschr. für Phys. C 32 (1986) 133.

[56] A. Martin, Proc. second Int. Conference on Elastic and Diffractive Scattering New York 1987, p.145.

[57] L. Lukaszuk and B. Nicolescu, Nuov. Cim. Lett. 8 (1973) 405.

[58] K. Kang and B. Nicolescu, Phys. Rev. D 11 (1975) 2461.

[59] E. Leader, Phys. Rev. Lett. 59 (1987) 1525.

[60] D. Bernard, P. Gauron and B. Nicolescu, Phys. Lett. B199 (1987) 125.

[61] S. Hadjitheodoridis and K. Kang, Phys. Lett. B208 (1988) 135.

[62] S. Troshin and N. Tyurin, Phys. Lett. B208 (1988) 517.

[63] S. Troshin, N. Tyurin and O. Yushchenko, Nuov. Cim. 91A (1986) 23.

[64] B. Kopeliovich, N. Nikolaev and I. Potashnikova, Phys. Lett. B209 (1988) 355.

[65] UA1 Collaboration, C. Albajar et al., CERN preprint EP88-29, submitted to Nucl. Phys. B.

[66] J. Kogut, G. Frye and L. Susskind, Phys. Lett. B40 (1972) 469.

[67] D. Cline, F. Halzen and J. Luthe, Phys. Rev. Lett. 31 (1973) 491.

[68] see e.g. references [70],[71], [72], [73], [74], [75], [76].

[69] see e.g. references [72], [73], [74], [75], [76].

[70] T.K. Gaisser and F. Halzen, Phys. Rev. Lett. 54 (1985) 1754.

[71] G. Pancheri and Y. Srivastava, Phys. Lett. 159B (1985) 69.

[72] G. Pancheri and Y. Srivastava, Phys. Lett. 182B (1986) 199.

[73] M. Jacob and P. Landshoff, CERN preprint TH.4562/86.

[74] N. Antononiou et al., Z. Phys. C 36 (1987) 461.

[75] A. Capella, J. Tran Thanh Van and J. Kwiecinski, Phys. Rev. Lett. 58 (1987) 2015.

[76] L. Durand and H. Pi, Phys. Rev. Lett. 58 (1987) 303.

[77] M. Block and R. Cahn, Rev. Mod. Phys. 57 (1985) 563.

[78] N. Amos et al., Phys. Rev. Lett. 61 (1988) 525.

[79] E. Eichten et al., Rev. Mod. Phys. 56 (1984) 601, errata Rev. Mod. Phys. 58 (1986) 1065.

[80] D. Duke and J. Owens, Phys. Rev. D 30 (1984) 49.

[81] M. Glück, E. Hoffman and E. Reya , Z. Phys C 13 (1982) 119.

[82] L. Gribov, E. Levin and M. Ryskin, Phys. Rep. C 100 (1983) 1.

[83] J. Collins, Proc. of the Summer Study on the design and Utilisation of the SSC, Snowmass Colorado 1984, p.251.

[84] W. Galbraith et al., Phys. Rev. B 138 (1965) 913.

[85] G. Belletini et al., Phys. Lett. 14 (1965) 164.

[86] K. Foley et al., Phys. Rev. Lett. 19 (1967) 857.

[87] S. Denisov et al., Phys. Lett. 36B (1971) 415.

[88] S. Denisov et al., Nucl. Phys. B65 (1973) 1.

[89] A. Caroll et al., Phys. Rev. Lett. 33 (1974) 928.

[90] A. Caroll et al., Phys. Lett. 61B (1976) 303.

[91] A. Caroll et al., Phys. Lett. 80B (1979) 423.

[92] G. Bezognikh et al., Phys. Lett. 39B (1972) 411.

[93] G. Bezognikh et al., Phys. Lett. 43B (1973) 85.

[94] U. Amaldi et al., Nucl. Phys. B145 (1978) 367.

[95] U. Amaldi and K. Schubert, Nucl. Phys. B166 (1980) 301.

[96] V. Bartenev et al., Phys. Rev. Lett. 29 (1972) 1755.

[97] V. Bartenev et al., Phys. Rev. Lett. 31 (1973) 1088 and 1367.

[98] L. Baksay et al., Nucl. Phys. B141 (1978) 1.

[99] J. Burq et al., Phys. Lett. 109B (1982) 124.

[100] K. Eggert et al., Nucl. Phys. B98 (1975) 93.

[101] L. Fajardo et al., Phys. Rev. D 24 (1981) 46.

[102] G. Carboni et al., Nucl. Phys. B254 (1985) 697.

[103] R. Breedon, Proc. second Int. Conference on Elastic and Diffractive Scattering New York 1987, p.179.

[104] for σ_{pp}: [84], [85], [86], [87], [89], [100], [90], [98], [94], [95], [91], [102], [4]; for $\sigma_{p\overline{p}}$: [84], [87], [88], [89], [90], [91], [95], [8], [102], [4]; for ρ_{pp}: [86], [92], [93], [96], [97], [29], [95], [103], [99], [4], [3]; for $\rho_{p\overline{p}}$: [86], [101], [103], [4], [3].

Acknowledgements

This thesis could not be written without the support and effort of many people. First I would like to thank all members of the UA4 Collaboration, and especially my co-workers Denis Bernard and Vincenzo Innocente, with whom I spent many days analysing and discussing the data.

I found it very stimulating to work at the NIKHEF-H in Amsterdam and I benefited from discussions with other experimental physicists and theoreticians. I am grateful to Prof. Dr. K. J. F. Gaemers for his valuable comments on the dispersion relations and the validity of perturbative QCD. I would like to acknowledge the operators and the other members of the computer group, especially Dr. W. M. van Leeuwen for assisting me with the running of large computer programms, and providing me with a helpful iterative programme that produces jobs ad infinitum.

At the conferences I learned a lot from the discussions with Prof. Dr. J. Dias de Deus, Prof. Dr. E. Leader, Prof. Dr. B. Nicolescu and Prof. Dr. J. Soffer concerning the high ρ value. I would like to thank Dr. M. Botje for his valuable suggestions on the high energy extrapolations. The enlightening comments of Prof. Dr. A. Martin on the dispersion relations were extremely valuable to me.

I am indebted to my promotor Prof. Dr. G. Matthiae for his valuable comment at all stages of the analysis. His clear intuition and keenness of observation showed the way to the solution of many problems. I am grateful to my co-promotor and supervisor Dr. J. J. M. Timmermans for his precise and observant criticism of the physics results and his elucidating comments on this thesis. I want to express my gratitude to my promotor Prof. Dr. A. N. Diddens for his stimulating support and his valuable, critical suggestions for the improvement of this thesis.

Finally I want to thank Miriam for her help, love and care during this restless time.

Summary

In this thesis the measurement of elastic scattering of protons and antiprotons and the ratio ρ, i.e. the ratio of the real to the imaginary part of the elastic scattering amplitude at momentum transfer squared $-t$ equals zero (i.e. a scattering angle zero) at a centre of mass energy $\sqrt{s}$ of 546 GeV is described. The experiment, that was proposed and carried out by the UA4 Collaboration, took place in June 1985 at the proton-antiproton Collider at CERN in Geneva.

The motivation of the experiment is to investigate whether the total cross section for pp and $p\overline{p}$ still rises as $\ln^2(s)$ in the TeV energy domain. The rise of the total cross section was discovered at the ISR (Intersecting Storage Rings) and later confirmed by the measurement of the total cross section for $p\overline{p}$ by the UA4 (and UA1) experiment at the SPS (Super Proton Synchrotron) at CERN. The ratio ρ is related to the high energy behaviour of the total cross section by the dispersion relations. If one assumes - as is done in most models - that the total cross section continues to rise like $\ln^2(s)$ in the TeV energy domain, a prediction for $\rho_{p\overline{p}}$ in the range of 0.12-0.14 can be obtained. By measuring $\rho_{p\overline{p}}$ this prediction of different models for elastic scattering can be tested.

In the first chapter a general introduction is given. The relevant theory for elastic scattering is presented and the method for extracting ρ from the distribution of elastically scattered particles is sketched. Special attention is paid to the derivation of the different forms of the dispersion relations.

The experimental set up is explained in chapter 2. The special super-high-beta optics of the Collider, that was necessary to measure scattered particles down to angles of $\sim$ 120 μrad, is discussed. The detector and the precise calibration of proportional and drift planes - that measure the vertical and horizontal coordinate of the particle - is described.

A report of the measurement of the real part and ρ is presented in the third chapter. The data taking, data processing and the selection of elastic events is described. After the determination of the efficiency of the detector, the experiment is simulated by the Monte Carlo method and a distribution of events as a function of the momentum transfer squared $-t$ is obtained. The final value for $\rho_{p\overline{p}}$ (546 GeV) is obtained by a fit to this distribution and yields 0.24 ± 0.04. The result is checked against modifications of the parametrisation of the nuclear scattering amplitude.

The implications of the measured $\rho_{p\overline{p}}$ value are discussed in chapter 4. The measured value is almost three standard deviations higher than the expected value

for ρ that equals 0.12-0.14. A dispersion relation analysis of the high ρ value is presented and it is shown that the implications for the high energy behaviour of the total cross section are twofold:
(1) either - in the so-called even scenario - the total cross section for pp and $p\overline{p}$ rises steeper than the assumed $\ln^2(s)$ (of the standard Amaldi parametrisation of the total cross section). The so-called Froissart-Martin bound is in that case not surpassed.
(2) or - in the odd scenario - the difference of the total cross sections for pp and $p\overline{p}$ rises as a function of the energy and the total cross section for pp becomes larger than the total cross section for $p\overline{p}$ above $\sqrt{s} \sim 100$ GeV.
Quantitative predictions for both scenarios are given and new parametrisations for the total cross section are proposed.

In the last chapter the hypothesis is investigated whether the steep rise of the total cross section (in the even scenario) is related to the rise of the minijet cross section, that was measured by the UA1 experiment. A simple hypothesis for elastic scattering is elaborated to calculate the inelastic (non-single-diffractive) cross section. This cross section is compared to the jet cross section that is calculated in first order Perturbative Quantum Chromo Dynamics (PQCD). It is shown that - using an equation for the total cross section where an extra term of the form $\ln^2(1 + s/s_1)$ is added to the standard Amaldi parametrisation - both cross sections follow the same trend. This means that there is an indication that $\rho_{p\overline{p}}$ (546 GeV) should be high and that the total cross sections for pp and $p\overline{p}$ should rise locally steeper than the assumed $\ln^2(s)$ in the TeV energy domain.

Samenvatting

In dit proefschrift wordt de meting besproken van de elastische vertrooiing van protonen en anti-protonen en de verhouding ρ, gedefinieerd als de verhouding van het reeële tot het imaginaire gedeelte van de nucleaire verstrooiingsamplitudo, bij een (gequadrateerde) impulsoverdracht $-t$ gelijk aan nul (d.w.z. bij een verstrooiingshoek, die gelijk aan nul is) en bij een zwaartepuntsenergie $\sqrt{s}$ van 546 GeV. Het experiment werd voorgesteld door het UA4 samenwerkingsverband en in juni 1985 uitgevoerd met behulp van de proton-antiproton-botser op CERN in Geneve.

De motivatie voor dit experiment is te onderzoeken of de totale werkzame doorsnede voor pp (proton-proton) en $\mathrm{p\overline{p}}$ (proton-antiproton) voor energieën in het gebied van enkele TeV's nog steeds stijgt als $\ln^2(s)$. De stijging van de pp totale werkzame doorsnede werd ontdekt bij het ISR (Intersecting Storage Rings) en later bevestigd door de meting van de totale werkzame doorsnede voor $\mathrm{p\overline{p}}$ door het experiment UA4 (en ook UA1) aan het SPS (Super Proton Synchrotron) op CERN. De verhouding ρ is gerelateerd aan de stijging van de totale werkzame doorsnede bij hogere energieën door de dispersierelaties. Als men aanneemt - zoals in de meeste modellen wordt gedaan - dat de totale werkzame doorsnede blijft stijgen als $\ln^2(s)$, kan voor $\rho_{\mathrm{p\overline{p}}}$ bij 546 GeV een waarde van 0.12-0.14 worden afgeleid. Door $\rho_{\mathrm{p\overline{p}}}$ te meten kan deze voorspelling worden getest en tussen verschillende modellen voor elastische verstrooiing worden gekozen.

In het eerste hoofdstuk wordt een algemene inleiding gegeven. De relevante theorie voor elastische verstrooiing wordt besproken en de methode om ρ uit de distributie van elastisch verstooide deeltjes te bepalen wordt geschetst. De afleiding van de verschillende vormen van dispersierelaties krijgt bijzondere aandacht.

De experimentele opstelling wordt beschreven in hoofdstuk 2. De speciale 'super-hoge-beta'-optica van de proton-antiproton-botser, die noodzakelijk was om verstrooide deeltjes bij hele lage hoeken van ~ 120 μrad te kunnen detecteren, wordt besproken. Vervolgens wordt de detector en de preciese calibratie van de proportionele en drift vlakken - die de verticale en horizontale coordinaat van het deeltje meten - beschreven.

De meting van ρ is het onderwerp van het derde hoofdstuk. Het vergaren en het verwerken van de meetgegevens, en de uiteindelijke selectie van elastische gebeurtenissen wordt eerst beschreven. Na de bepaling van de efficiëntie van de detector wordt het experiment met behulp van de Monte Carlo methode gesimuleerd. De verdeling van gebeurtenissen als een functie van de (gequadrateerde)

impulsoverdracht $-t$ wordt op deze wijze verkregen. De waarde van ρ wordt bepaald door een (kleinste quadraten) aanpassing aan deze distributie. Het resultaat $\rho_{p\overline{p}}$ (546 GeV) $= 0.24 \pm 0.04$, blijft hetzelfde als de parametrisatie van de nucleaire verstrooiingsamplitudo op verschillende wijzen wordt veranderd.

De gevolgen van de gemeten waarde van $\rho_{p\overline{p}}$ bij 546 GeV worden in hoofdstuk 4 besproken. De gemeten waarde is bijna drie standaard-afwijkingen hoger dan de voorspelde waarde, die tussen de 0.12 en 0.14 ligt. Een analyse van de hoge ρ waarde met behulp van de dispersierelaties wordt gegeven. Er wordt aangetoond dat de gevolgen voor het gedrag van de totale werkzame doorsnede bij hoge energieën tweevoudig zijn:
(1) ofwel stijgt - in het zgn. even scenario - de totale werkzame doorsnede voor pp en $p\overline{p}$ als functie van de enrgie sneller dan $\ln^2(s)$, de stijging die meestal (in de vorm van bijv. de Amaldi parametrisatie van de totale werkzame doorsnede) wordt aangenomen. De zgn. Froissart-Martin grens wordt hierbij echter niet overschreden.
(2) ofwel stijgt - in het oneven scenario - het verschil van de totale werkzame doorsnedes van pp en $p\overline{p}$ als functie van de energie en wordt de totale werkzame doorsnede voor pp groter dan de totale werkzame doorsnede voor $p\overline{p}$ boven $\sqrt{s} \sim$ 100 GeV.
Voor beide scenario's worden quantitatieve voospellingen gegeven en nieuwe parametrisaties voor de totale werkzame doorsnede voorgesteld.

In het laatste hoofdstuk wordt de hypothese onderzocht of de snelle stijging van de totale werkzame doorsnede samenhangt met de stijging van de werkzame doorsnede voor minijet's. Een eenvoudige hypothese voor elastische verstrooiing wordt uitgewerkt om de inelastische (zonder de enkel-diffractieve) werkzame doorsnede te berekenen. Deze werkzame doorsnede wordt vergeleken met de werkzame doorsnede voor jet's, die met behulp van de eerste-orde-storingstheorie van de quantumchromodynamica (PQCD) wordt berekend. Er wordt aangetoond dat - als een vergelijking voor de totale werkzame doorsnede wordt gebruikt, waarbij een extra term $\ln^2(1 + s/s_1)$ wordt toegevoegd aan de standaard Amaldi parametrisatie - beide werkzame doorsnedes gelijk oplopen. Dit betekent dat er een aanwijzing bestaat dat $\rho_{p\overline{p}}$ (546 GeV) hoog zal moeten zijn en dat de totale werkzame doorsnede voor pp en $p\overline{p}$ voor energieën in het gebied van enkele TeV's sneller zal moeten stijgen dan $\ln^2(s)$.